DIGITAL SIGNAL PROCESSING OF HEMODYNAMIC SIGNALS

DIGITAL SIGNAL PROCESSING OF HEMODYNAMIC SIGNALS

By
ANNE XIAO-AN HU, B. ENG.

A Thesis Submitted to
the School of Graduate Studies
in Partial Fulfillment of the Requirements
for the Degree
Master of Engineering

McMaster University

Master of Engineering (1999)
(Electrical and Computer Engineering)

McMaster University
Hamilton, Ontario

TITLE: Digital Signal Processing of Hemodynamic Signals

AUTHOR: Anne Xiao-An Hu, B. Eng. (Shanghai Jiaotong University)

SUPERVISOR: Dr. Markad V. Kamath, Ph.D.

NUMBER OF PAGES: clxiii, 163

Abstract

Physiological signals when subjected to digital signal processing algorithms often reveal information about their origin and how they are regulated. Recently, it has been shown that when power spectrum of the heart rate variability signal is computed, physiological mechanisms about how the autonomic nervous system modulates the sinus node of the heart can be unraveled. During the past several years, computation of the power spectrum of heart rate variability has progressed from Blackman-Tukey algorithm and autoregressive modelling to Wigner-Ville distribution.

In this thesis, we describe the development of appropriate algorithms for QRS detection from an ECG signal to obtain a heart rate signal, interpolation of heart rate variability signal and the computation of power spectrum. We also describe mathematical details underlying time-frequency analysis, specifically for the Wigner-Ville distribution. We present a software package in C++, for computing the Wigner-Ville distribution of the heart rate variability signal.

As applications of these methods in physiology and clinical medicine, we found that the power spectrum of the heart rate variability of premature infants can help us understand the ontogeny of the autonomic nervous system. Similarly, physiological effects of atropine, methacholine and allergen challenges can be elucidated using the power spectrum of heart rate variability in small animals, such as a rat model. Furthermore, a progressive tilt model in human subjects is used to compare power spectrum obtained from the Blackman-Tukey method, autoregressive modelling and the Wigner-Ville distribution. Finally, an application of the Wigner-Ville distribution technique to study the changes that take place in the autonomic regulation of the heart during different stages of sleep is presented.

DEDICATION

This thesis is dedicated to my grandmother Liu Jintang
in memory of her courage and generosity.

Acknowledgements

This thesis is made possible with the aid and support of numerous people, to whom I am grateful.

First and foremost, I would like to thank my supervisor Dr. Markad V. Kamath for his excellent mentoring ability and continuous support. Special thanks go to Dr. Ernest L. Fallen for all those stimulating group discussions.

I would like to express my appreciation to Dr. Kevin Jacobson, Dr. Adrian Upton and Dr. Veljko Djuric for providing patient material and animal laboratory facilities.

Thanks go to Zhinong He, Sabrina Quick, Sameer Hajee, Faisal Shad, Andrew May, Changxiong Bian and James Huggins for providing me the most needed feedback and help.

Thanks go to my Sensei Philip McColl for showing me the warrior spirit.

I would like to thank my mother, my father, my sister and my brother-in-law for their unwavering support over the past two years.

Finally, I am grateful to Heart and Stroke Foundation of Canada for their support of this research. Computer and laboratory facilities provided by de Groote Foundation and National Science and Engineering Research Council helped me to complete the software development process in a record time.

TABLE OF CONTENTS

List of Figures

List of Tables

List of Acronyms

2-D	2-Dimensional
3-D	3-Dimensional
ACF	Autocorrelation Function
AIC	Akaike Information Criterion
ANS	Autonomic Nervous System
AR	Autoregressive
AS	Active Sleep
BAL	Bronchoalveolar Lavage
BP	Blood Pressure
BPV	Blood Pressure Variability
BT	Blackman-Tukey
CA	Conceptional Age
DBP	Diastolic Blood Pressure
DC	Direct Current
DSP	Digital Signal Processing
ECG	Electrocardiogram
ED	Exponential Distribution
EEG	Electroencephalogram
EMG	Electromyogram
EOG	Electro-oculogram
FIR	Finite Impulse Response
FFT	Fast Fourier Transform
FT	Fourier Transform
GA	Gestational Age
GUI	Graphical User Interface
HF	High-Frequency
HR	Heart Rate
HRV	Heart Rate Variability
LF	Low-Frequency
MFC	Microsoft Foundation Class
NICU	Neonatal Intensive Care Unit
OOP	Object-Oriented Programming
PA	Post-natal Age
PEF	Prediction Error Filter
PS	Power Spectrum
PSA	Power Spectral Analysis
PSMP	Parasympathetic
QS	Quiet Sleep
REM	Rapid Eye Movement
RID	Reduced Interference Distribution
RSA	Respiratory Sinus Arrhythmia
SBP	Systolic Blood Pressure
STFT	Short-Time Fourier Transform

SMP	Sympathetic
T-F	Time-Frequency
TFA	Time-Frequency Analysis
TFD	Time-Frequency Distribution
VLBW	Very Low Birth Weight
VLF	Very-Low-Frequency
WT	Wavelet Transform
WD	Wigner Distribution
WVD	Wigner-Ville Distribution

Chapter 1

Autonomic Nervous System and Types of Hemodynamic Signals

1.1 INTRODUCTION

Recent studies on the analysis of heart rate variability (HRV) & blood pressure variability (BPV) signals using digital signal processing methods in adult, pediatric and newborn human subjects have provided significant insights into the understanding of autonomic control of heart rhythms. Specifically, HRV studies through power spectral analysis (PSA) have brought out a better understanding of the role the autonomic nervous system (ANS) plays in homeostasis and in pathological conditions such as myocardial infarction, diabetic neuropathy, congestive heart failure, and sudden cardiac death (Lombardi et al., 1987; Lishner, et al, 1987; Saul et al., 1988; Myers et al, 1986; Dougherty, et al, 1992).

During the last 15 years, digital signal processing methods for computing appropriate indices from HRV/BPV have advanced from simple time domain statistics

such as mean & standard deviation (Hon and Lee, 1965) to 24 hour HRV data analysis using AR modelling & time-frequency analysis (TFA). Our laboratory has examined a number of these techniques in healthy controls and patients (Kamath and Fallen, 1993). This thesis extends such work by developing appropriate algorithms for monitoring neural modulation of the sinus node in premature infants and animal models. Furthermore, we also explored the usefulness of time-frequency analysis in healthy controls during passive tilt studies and in sleep. The objectives of this thesis are as follows:

A. To review and develop HRV algorithms for studying premature infants in a neonatal nursery.

B. To develop algorithms for evaluating the autonomic nervous system in a rat model and study the effect of atropine and methacholine.

C. To test algorithms for time-frequency analysis of HRV recorded in a tilt study and compare results obtained using AR method.

D. To assess various stages of sleep in healthy volunteers using time-frequency analysis and compare the results obtained through AR method.

In addition, the software described in this thesis was written using C++, incorporating Modularization and Object-Oriented Programming (OOP) techniques, which enabled me to achieve proficiency in the development of Digital Signal Processing (DSP) methods and user interface design. Finally, Graphic User Interface (GUI) and 2-D/3-D plotting were implemented to generate a user-friendly environment, which enables a broad range of users including physicians, psychologists, kinesiologists, and biologists to take full advantage of this novel signal processing tool.

In the first chapter we introduce the physiological concepts of autonomic nervous system (ANS), its influence on the heart, the types of hemodynamic signals which facilitate the study of ANS, and respiratory sinus arrhythmia.

1.2 OVERVIEW OF AUTONOMIC NERVOUS SYSTEM

The autonomic nervous system plays a very important role in the regulation of the viscera, glands, heart, and blood vessels, as well as other smooth muscles (Hockman, 1987). The ANS is made up of two functional branches: the sympathetic (SMP) branch and the parasympathetic (PSMP) branch. Specifically for the heart, sympathetic fibers terminate at the sinus node pacemaker, conduction system, atria, ventricles, and coronary vessels. The parasympathetic fibers in the vagus nerve terminate at the sinoatrial and atrioventricular nodes, atrial and ventricular musculature, and coronary vessels. All blood vessels receive sympathetic fibers and some vessels supplying visceral organs such as the heart also receive parasympathetic fibers (Figure 1.1) (Hockman, 1987).

1.3 TYPES OF HEMODYNAMIC SIGNALS

There are two types of beat-to-beat hemodynamic signals that can be used to facilitate the noninvasive investigation of heart function: beat-to-beat heart rate variability (HRV) and beat-to-beat blood pressure variability (BPV) (including systolic & diastolic BPV). They are obtained from electrocardiogram (ECG) and blood pressure (BP) signals respectively. The critical requirement for obtaining the HRV signal from ECG signal is the identification of the instantaneous R-R interval (Figure 1.2), which is

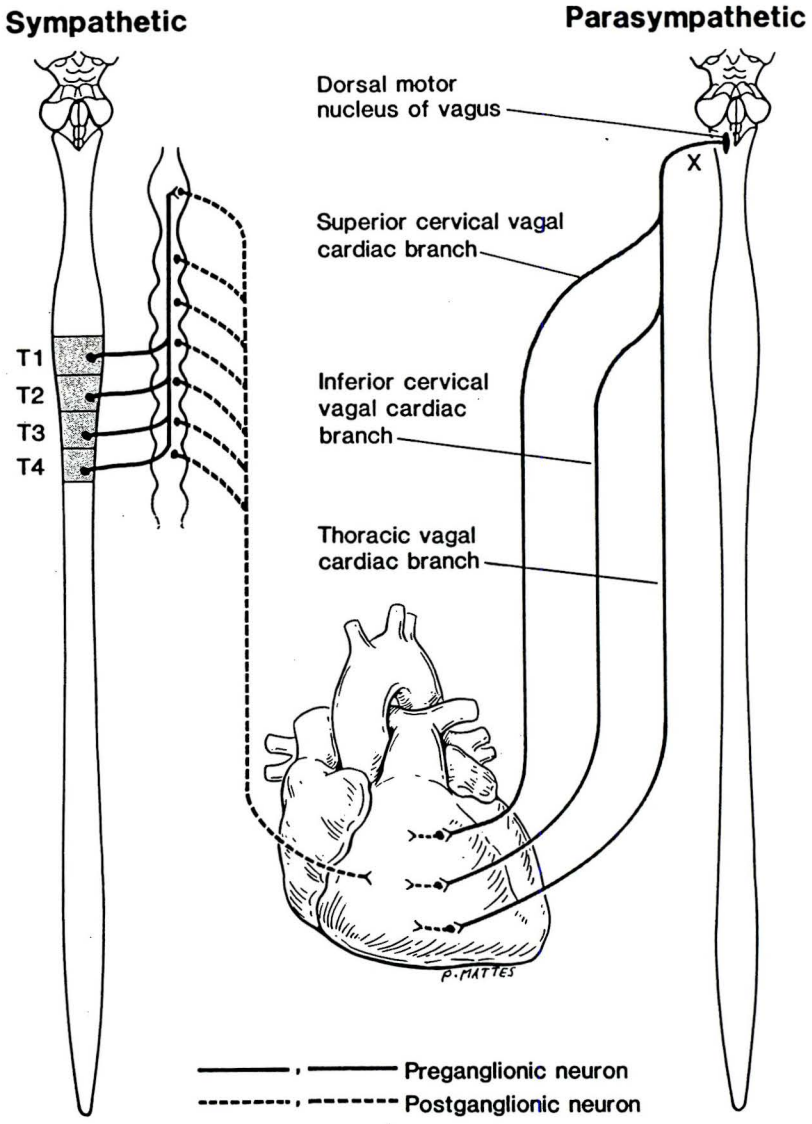

Figure 1.1 Diagram depicts nerve supply to the heart from both branches of the autonomic nervous system. Preganglionic fibers from both branches are represented by solid lines. Postganglionic fibers from both branches are represented by dashed lines: terminals from the sympathetic branch are distributed to the pacemaker, conduction system, atrial and ventricular myocardium, and coronary vessels; and from the parasympathetic branch fibers terminate in the sinoatrial and atrioventricular nodes, atrial and ventricular musculature, and coronary vessels. (From Hockman CH, *Essentials of autonomic function.* Springfield IL, pp. 42, 1987).

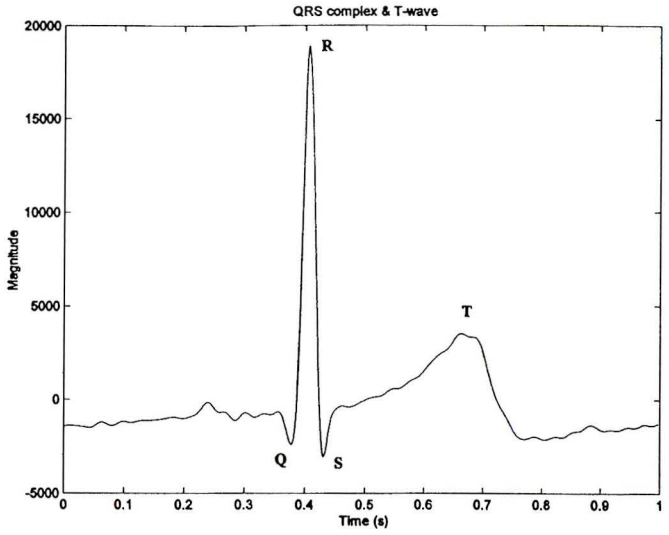

(a)

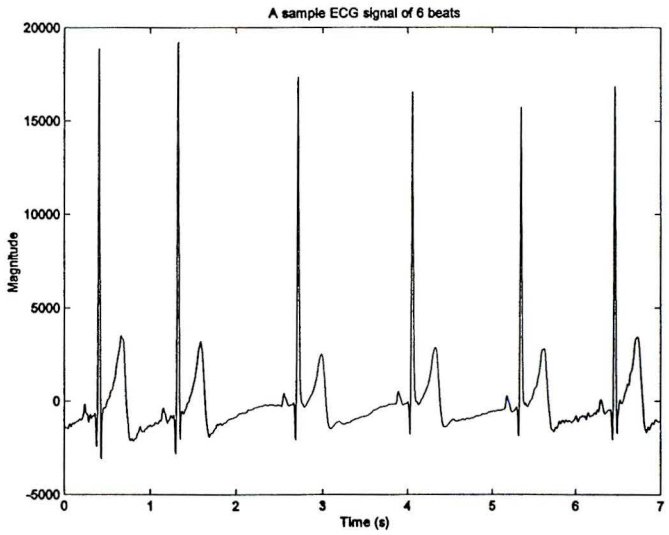

(b)

Figure 1.2 Illustration of the basic concepts utilized in QRS detection: (a) QRS complex & T-wave. (b) Sample ECG signal of 6 heartbeats. (c) Five R-R intervals obtained from previous sample signal. (d) R-R interval signal of a sample ECG signal containing 300 heartbeats.

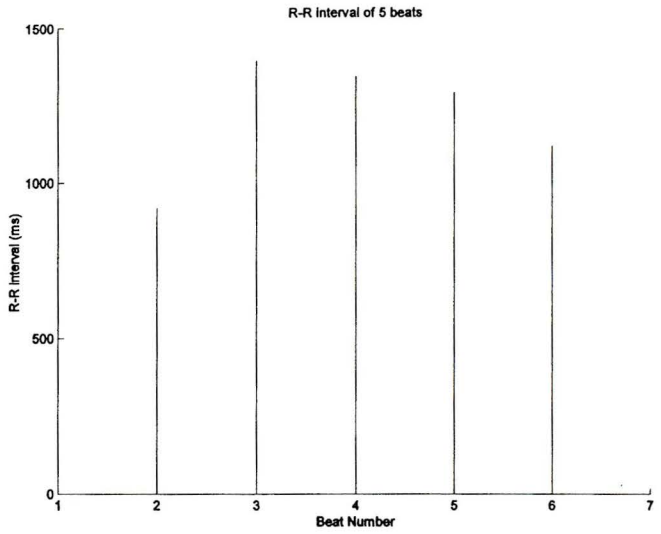

(c)

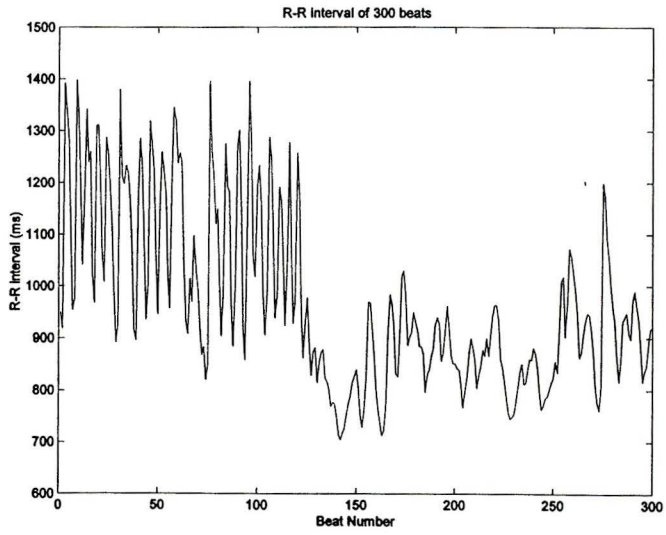

(d)

Figure 1.2 (*contd.*)

called QRS detection and is discussed in detail in Chapter 2. Computation of BPV signal requires the original BP signal and a knowledge of peak position of the QRS. It utilizes the fact that the BP peak (systolic BP) and BP trough (diastolic BP) always occur between two adjacent QRS complexes.

Recognition of beat-to-beat fluctuations in heart rate and blood pressure dates back to the 18th century (Hales, 1733). Similar variations have since been noted in stroke volume and ECG morphology and are believed to represent the interplay between both exogenous (eg. environmental stress) and endogenous (eg. respiratory related fluctuations of intrathoratic pressure) cardiovascular perturbations and the resultant response of hemodynamic regulatory mechanisms (Harvey, 1997).

Today HRV analyses in both the time and frequency domains have proven to be viable tools for the noninvasive assessment of cardiac autonomic function (Kamath and Fallen, 1993; Task Force 1996). This tool has been used to assess cardiovascular responses to various pharmacological agents (Vybiral et al., 1990) and physiological maneuvers such as orthostasis/postural tilt (Pagani et al., 1986), the Valsalva maneuver (Ziegler et al., 1992) and exercise (Kamath, 1991). Recent work has focused on developing joint time-frequency analysis (TFA) (Jasson et al., 1997; Novak et al., 1993; Pola et al., 1996) because of its potential for extracting useful information from nonstationary signals. Time-frequency analysis is the focus of Chapter 3 in this thesis.

1.4 RESPIRATORY SINUS ARRHYTHMIA

At rest the heart rate increases with inspiration and decreases with expiration. This beat-to-beat variation of heart rate, which occurs during a respiratory cycle, has been

of interest to physiologists since the middle of the last century (Ludwig, 1847). This phenomenon is called respiratory sinus arrhythmia (RSA) and has been well documented (Katona et al., 1975; Brown et al., 1993; Harvey, 1997). Three mechanisms are proposed to account for the coupling of heart rate oscillations with the respiratory cycle (Hirsch et al., 1981; Harvey, 1997).

The first mechanism involves the direct influence of medullary respiratory neurons on cardiomotor neurons in the brain stem (Hirsch et al., 1981). Indeed, Levy et al. (1966) observed RSA of heart rate in the absence of respiratory movements or blood pressure variations in dogs with the respiratory muscles paralyzed. Under the same conditions, deepening anesthesia affecting the respiratory centers resulted in the abolition of these heart period oscillations. The second mechanism is that blood pressure fluctuations secondary to respiratory movements affect heart period via mechanisms mediated by atrial stretch receptors and arterial baroreceptors. Thirdly, evidence suggests that thoracic stretch receptors (located in the lungs and chest wall) modulate heart rate as a reflex response to pulmonary inflation (Hirsch et al., 1981). In addition, there is no respiratory sinus arrhythmia during vagotomy.

Other indirect mechanisms, including the Bainbridge and baroreflex arcs contribute to the respiratory linked oscillations in heart rate (Novak et al., 1993). On inspiration, the chest cavity enlarges resulting in a decreased intrapleural pressure and a subsequent augmentation of venous return to the right atrium. This increase in atrial blood volume has a direct effect on receptors located in the wall of the atrium near the veno-atrial juctions and results in activation of the Bainbridge reflex which is manifested by an increase in heart rate (Harvey, 1997). The resultant increase in pulmonary arterial

and venous pressure leads to a subsequent augmentation in venous return to the left atrium and an increased left ventricular stroke volume. Consequently, increased pressure in the systemic arteries will result in a stimulation of aortic and carotid baroreceptors, which result in vagoafferent stimulation and reflex slowing of the heart rate. On expiration the intrathoracic pressure returns to baseline and the atria are subsequently unloaded. As a result the heart rate returns to pre-inspiration levels.

Whenever possible the respiration signal should be recorded along with ECG signal because of its tremendous influence on the modulation of heart rate.

Chapter 2

Algorithms for the Computation of Power Spectrum of Heart Rate Variability

2.1 OVERVIEW

In this chapter we discuss as to how to compute heart rate variability (HRV) signal from a given ECG signal and estimate the power spectrum (PS) from HRV signal. The most important step in the computation of HRV signal is QRS detection, which stands for the peak detection algorithm in ECG signal. The resultant HRV signal is subjected to the interpolation and highpass filtering processes to obtain an equally sampled (2 Hz) HRV signal ready for PS computation. Furthermore, two commonly used PS methods, i.e. autoregressive method and Blackman-Tukey procedure, are described in detail.

2.2 QRS DETECTION

2.2.1 Algorithms

QRS detection is the first step in a series of computational tasks in HRV signal analysis system. Its purpose is to determine the R-R intervals from the original ECG signal. In signal processing domain, QRS detection is not always easy because of inherent physiological variability of QRS complexes and contamination of the signal by various types of noise (Pan and Tompkins, 1985). For example, ECG signal is corrupted by following types of noise: power line interference (~60 Hz), electrode contact noise, motion artifacts, muscle contractions (electromyogram or EMG), baseline drift and ECG amplitude modulation by respiration (Figure 2.1) (Friesen, 1990).

QRS detectors implemented in software can be divided into following two subgroups: linear QRS detector and neural-network-based QRS detector. The linear QRS detector typically consists of the following processing steps: linear processing, a nonlinear transformation, and decision rules for detecting the R-waves (Pahlm and Sornmo, 1984). Linear processing may include a digital bandpass filter, a first order or second order derivative computation (Friesen, 1990), and a moving window integrator (Pan and Tompkins, 1985). The nonlinear transformation that is often used involves squaring of the amplitude of the ECG signal following linear processing (Pan and Tompkins, 1985). Its purpose is to enhance the difference of magnitude of QRS periods from non-QRS periods.

Decision rules are a set of criteria that a sample in ECG signal must meet in order to be characterized as a fiducial point on R-wave. Good decision rules lead to robust QRS detection. The decision rules may consist of several steps that determine the presence of

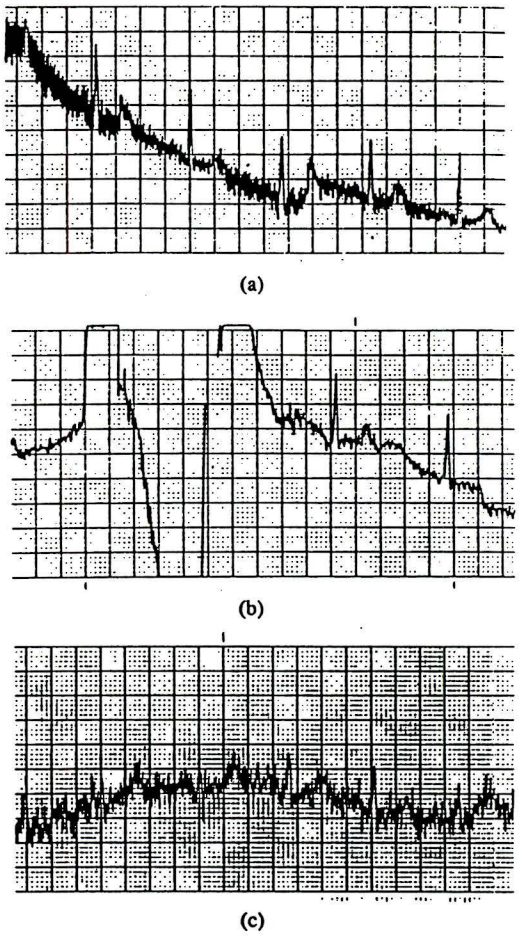

Figure 2.1 Noisy ECG signals: (a) power line interference and motion artifacts (b) loose contacts (c) ECG amplitude modulation by respiration (low frequency) and EMG (high frequency). (From Friesen GM et al., *IEEE Trans. Biomed. Eng.*, vol. 37, no. 1, pp. 85-98, 1990)

an R-wave such as adaptive threshold, T-wave discrimination (see Figure 1.1 for example of T-wave), and search-back techniques. A basic method used to locate a QRS complex is to compare the current signal magnitude to a pre-set threshold (usually a percentage of the signal envelope). The adaptive threshold technique utilizes that basic concept but also adjusts the threshold according to the evolving signal envelope and hence compensates the effects of baseline wandering and/or sudden changes in the QRS amplitude. The T-wave discrimination technique makes use of the fact that in ECG signals, there is a physiological refractory period of at least 200 ms after a QRS complex and before the next one occurs. Search-back technique continuously compares the current R-R time interval to the average interval and re-searches a period if the interval is much longer than the average value.

Not all of the aforementioned techniques have to be utilized in a specific QRS detector. The techniques should be chosen based on their performances and the requirement of efficiency and complexity. Among the methods utilized in the linear processing, a digital bandpass filter has the advantage of best handling combinations of noise if the contribution from each of the individual noise types can be limited (Friesen, 1990). A derivative calculation is good at reducing the effect of low-frequency drift and enhancing the transition from baseline to peak. However it also enhances the high-frequency noise (due to EMG). The idea of combining these two (removing high-frequency noise then perform derivative) to achieve the best result is not realizable due to the following reason. The EMG noise (frequency content is from DC to 10 kHz (Webster, 1978)) overlaps with the QRS complex (frequency content is from 2 to 100 Hz with a peak around 10 to 15 Hz (Ruha, 1997)). Hence, in the linear processing, we prefer to

utilize a digital bandpass filter, rather than a combination of a filter followed by a computation of the derivative.

The neural-network-based QRS detector utilizes an artificial neural network (ANN) adaptive whitening filter to model the lower frequencies of the ECG signal that are inherently nonlinear and nonstationary. The residual signal that contains mostly higher frequency QRS complex energy is then passed through a linear matched filter to detect the location of QRS complex. The strength of this approach lies in its high success rate on very noisy patient records in the MIT/BIH arrhythmia database (99.5% compared to 96.5% of linear methods) (Xue, Hu, and Tompkins, 1992).

In the current study, we developed a QRS detection algorithm based on the work of Ruha (1997). The algorithm is able to achieve good time accuracy in a relatively noisy environment, while at the same time, maintains low computational complexity. The QRS detection algorithm, details of which are given in the next section, includes a linear digital filtering process and a decision rule (Figure 2.2). The linear filtering process contains two linear bandpass filters (prefiltering bandpass & bandpass) which aim to attenuate noise and enhance the features used for detection. The decision rule is based on an adaptive amplitude comparison procedure and a T-wave discrimination technique. Since the threshold is continuously adapting to the envelope of ECG signal, the algorithm is able to capture the dynamic changes that occur during transient physiological states such as tilt or exercise. No search-back algorithm is utilized.

During the filtering stage, we use two bandpass filters to attenuate the low frequency and high frequency noise. Since we know that the QRS complex contains signal components in the frequency band from 2-100 Hz with a peak at 10-15 Hz, the

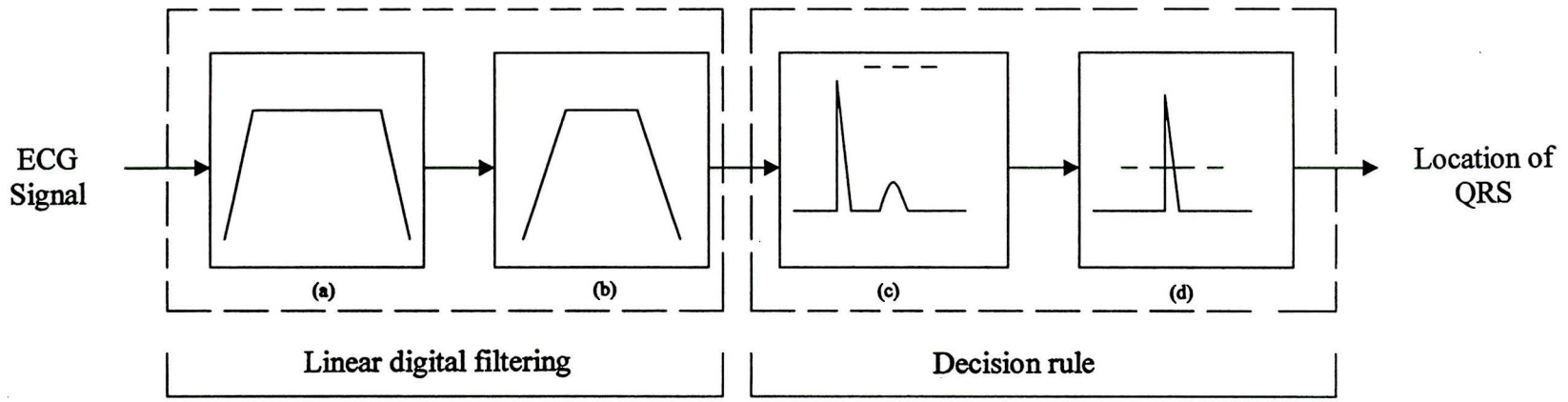

Figure 2.2 QRS detection method illustrated in block diagrams: (a) Prefiltering bandpass filter (0.5-35 Hz). (b) Bandpass filter (15-40 Hz). (c) T-wave discrimination technique. (d) QRS detection.

first band pass filter (0.5-35 Hz) is chosen to filter out the DC component, power line interference, and high frequency (EMG) noise. The second bandpass filter (15-40 Hz) is chosen to further remove the low frequency motion artifacts (2 to 10 Hz). In addition, utilizing the band 15-40 Hz instead of 10-35 Hz provides a significant reduction of the T-wave (Figure 2.6 (b)&(c)).

In the development of decision rules, principles from communications theory were applied for defining the threshold level. Assuming a heart rate of 60 beats/min, the QRS threshold should be around 60% of the peak value. In reality, the threshold should be set at a lower level (30-40%) in order to decrease the amount of false negatives (missed beats). This is at the expense of an increase in false positives that can be corrected more easily than false negatives in the post-processing stage. Besides, the threshold level must adapt to varying ECG signal envelopes in order to remain at the same relative level and maintain the desired detection properties.

2.2.2 Details of the Algorithms Employed

In the linear filtering process, the first bandpass filter is chosen to be a 48^{th} order FIR filter with pass band 0.5-35 Hz (Figure 2.3). The second bandpass filter is chosen to be a 48^{th}-order FIR filter with passband 15-40 Hz (Figure 2.4 (a)). The order of the FIR filter is chosen due to the following reasons. While comparing 48^{th}-order, 24^{th}-order, and 12^{th}-order FIR filters, we found that the amplitude response of the 48^{th}-order FIR filter has much sharper transition at the 3-dB point (Figure 2.4 (a)-(c)). As a result, it is shown in Figure 2.5 (a)-(c) that the 48^{th}-order FIR filter is able to attenuate the T-wave considerably. Figure 2.6 shows signals at various steps in the linear filtering process. The

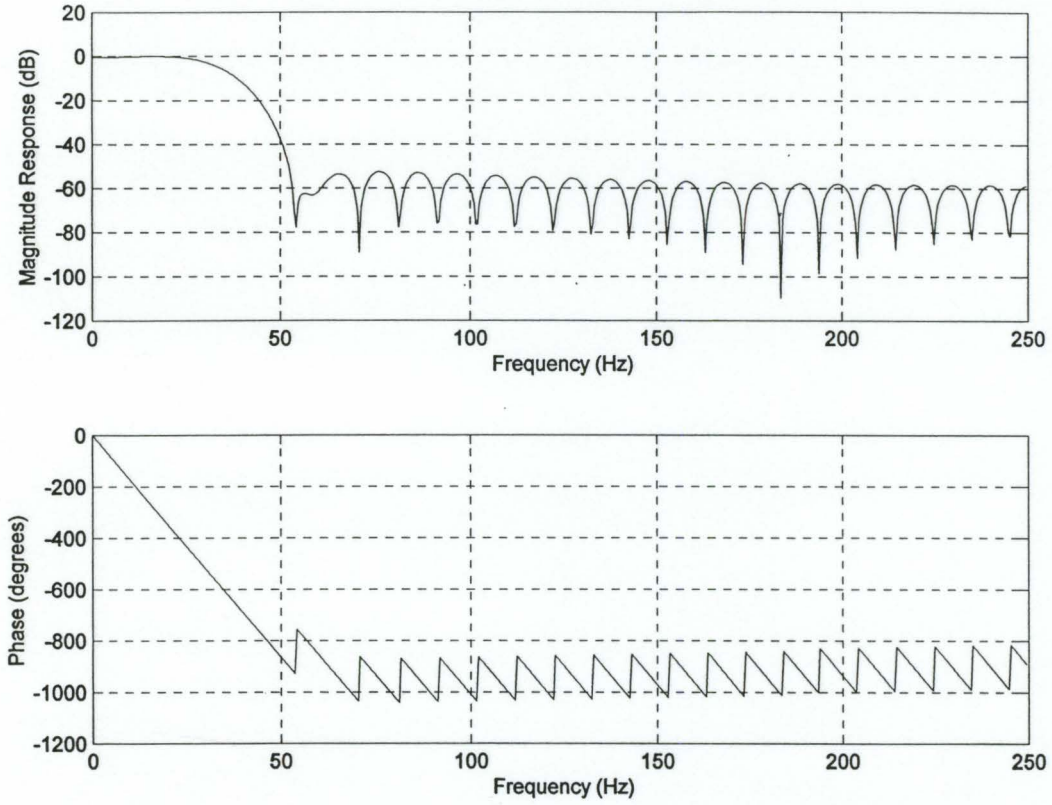

Figure 2.3 Magnitude and phase responses of prefiltering bandpass filter (0.5-35 Hz).

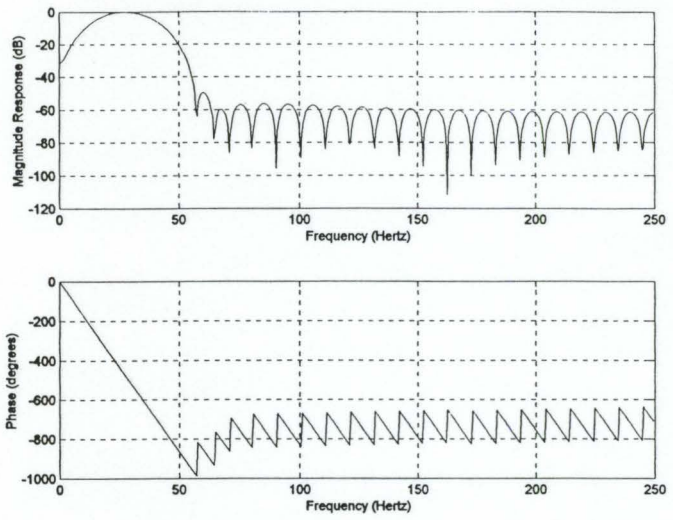

(a)

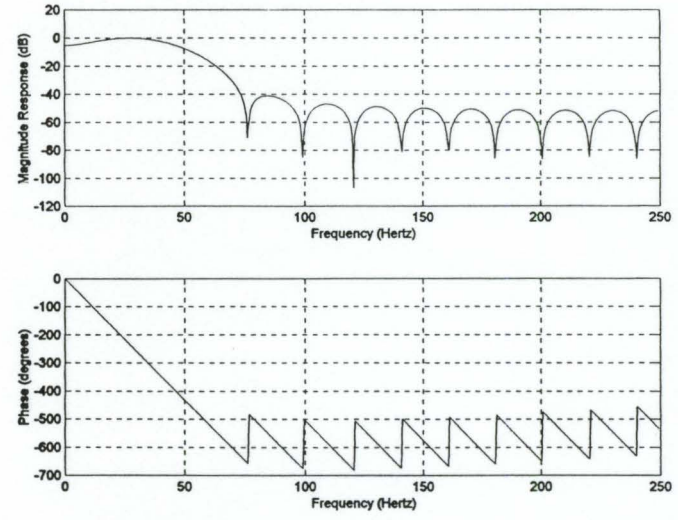

(b)

Figure 2.4 Comparison of magnitude and phase responses among three bandpass filters (15-40 Hz) with different order: (a) Order = 48. (b) Order = 24. (c) Order = 12.

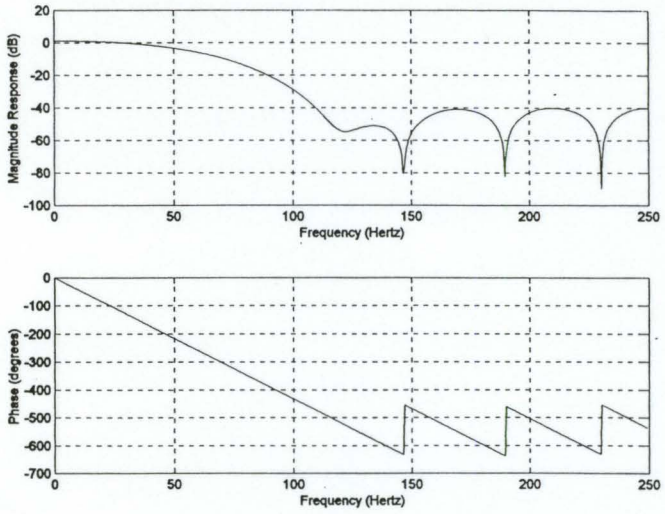

(c)

Figure 2.4 (*contd.*)

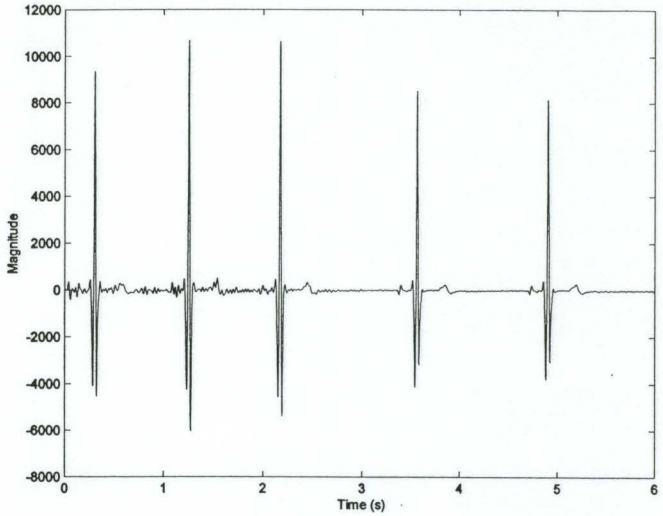

(a)

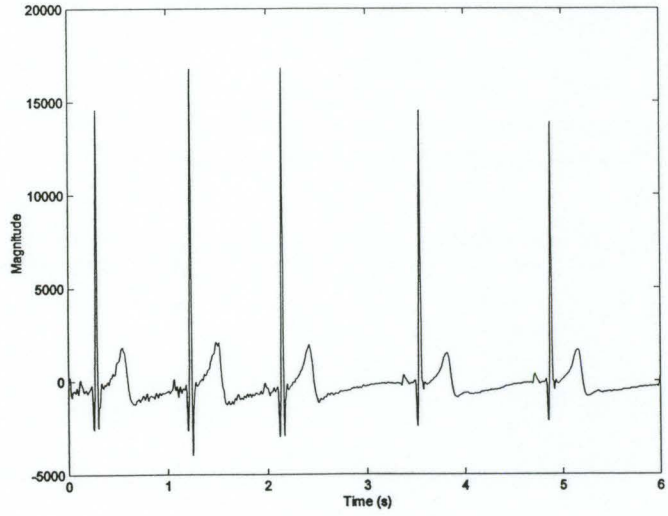

(b)

Figure 2.5 Comparison of results obtained from three bandpass filters (15-40 Hz) with different order: (a) Order = 48. (b) Order = 24. (c) Order = 12.

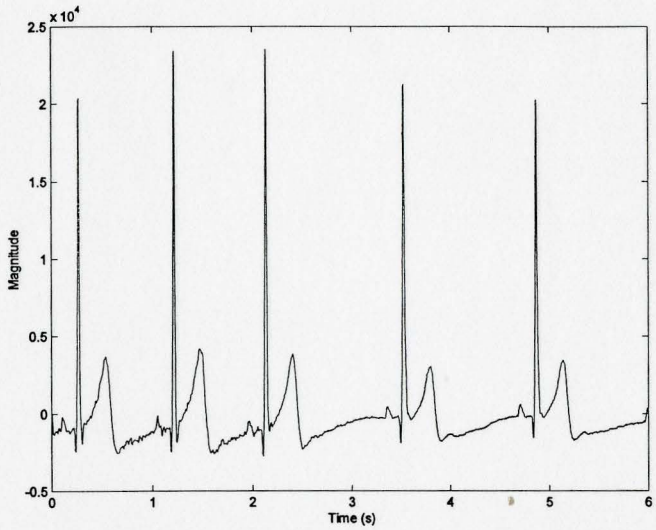

(c)

Figure 2.5 (*contd.*)

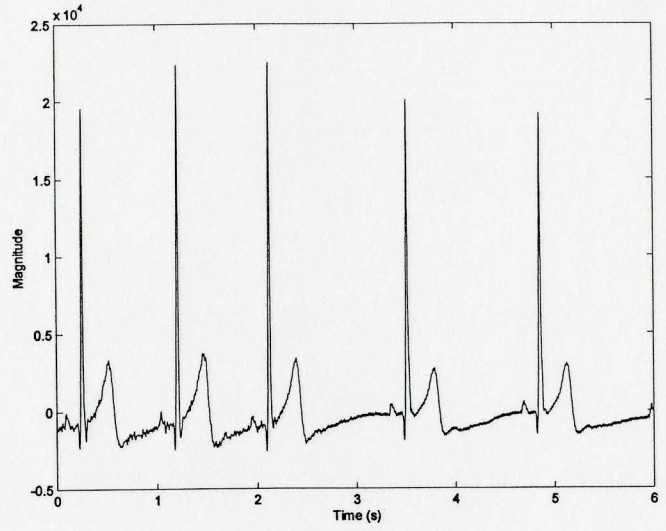

(a)

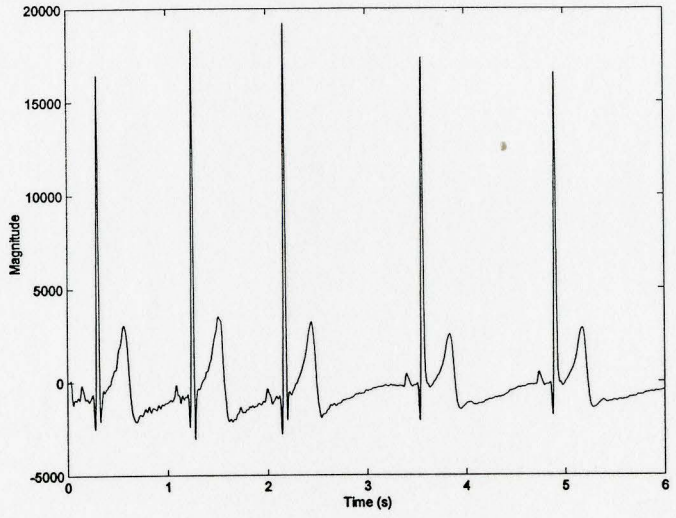

(b)

Figure 2.6 Examples of ECG signal at various steps in the linear filtering process: (a) original ECG signal. (b) ECG signal after prefiltering bandpass filtering (0.5-35 Hz). (c) ECG signal after second bandpass filtering (15-40 Hz).

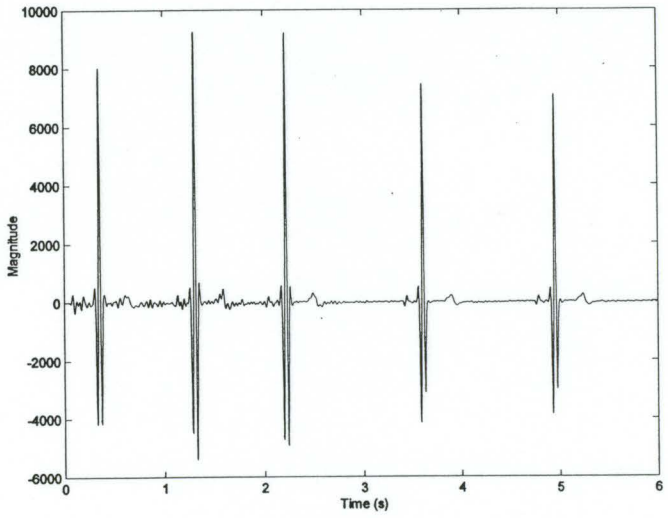

(c)

Figure 2.6 (*contd.*)

QRS decision rule is then implemented on the filtered ECG signal using an adaptive threshold. The threshold continuously adapts to 40% of the maximum value of the filtered ECG over the previous 2 seconds. After each positive QRS detection, the threshold is raised to 120% of the latest maximum value for 200 ms in order to prevent false detection due to a T-wave. The QRS detection algorithm with adaptive threshold comparison can be described using a pseudo-code as follows (Ruha, 1997).

Variable definitions:

ENV: envelope of filtered ECG signal
THR: threshold constant (0.4)
THRES: threshold coefficient
DET: binary value detection signal
ETR: envelope rise rate constant (1.2 /s)
EHC: envelope hold time constant (2 s)
T_LASTP: detection threshold keep time (200 ms)

For ("each output sample x(i) from the filtered ECG signal")
    if (x(i) > THRES * ENV)
        then DET(i) = 1 else DET(i) = 0.
    if (x(i) > ENV) then ENV = ENV + ETR*x(i).
    if (x(i) < ENV) and ("EHC seconds has passed since the previous update")
        then ENV = 0.9*ENV.
    if (DET(i) = 1) and (DET(i-1) = 0)
        then THRES = 1.2.
    if ("more than T_LASTP has passed since the previous detection") and
        (THRES > THR) then
        THRES = 0.9*THRES.

The QRS detection algorithm developed according to the above constraints was able to detect practically all of the QRS complexes of the signals recorded from healthy controls and patients in our laboratory. The algorithm shows an error rate of ±2 ms when tested against the results obtained using visual verification through CODAS data playback system (DATAQ Instruments, Inc., Akron Ohio 44333, USA). This is roughly 0.2% error for a heart rate of 60 beats/min.

2.3 FURTHER PROCESSING FOR HRV SIGNAL

After obtaining the R-R interval signal, we convert it into an instantaneous heart rate (HR) signal by inversion (e.g. R-R interval: 1000 ms leads to HR: 1 beat/s). Following this, a 2 Hz re-sampling procedure is implemented on the HR signal using linear interpolation technique. Finally we filter out the 0-0.025 Hz frequency component for reasons that are explained in Section 2.4.5 below.

2.4 POWER SPECTRUM COMPUTATION

2.4.1 Algorithms

For a given signal, the power spectrum (PS), or often called power spectral density (PSD), describes the distribution of power with frequency (Kay, 1988). For a signal $x(t)$, sampled at equal intervals of time, Δt, the PS is defined as the mean square value of the signal for each frequency component, over the frequency range for which the signal exists. The PS thus represents the average distribution of the power across the frequency range of interest. The computation of PS has been associated with Fourier transform (FT) of a signal and therefore power spectrum $P_x(f)$, is often expressed simply as the square of the absolute value of the FT of the signal. If $X(f)$ represents the FT of $x(t)$,

$$P_x(f) = X(f)X^*(f) = |X(f)|^2 \tag{2.1}$$

where $X^*(f)$ is the complex conjugate of $X(f)$. The Fourier transform and inverse Fourier transform are described as follows:

$$X(f) = \int_{-\infty}^{+\infty} x(t)e^{-j2\pi ft}dt \tag{2.2}$$

$$x(t) = \frac{1}{2\pi}\int_{-\infty}^{+\infty} X(f)e^{j2\pi ft}df \qquad (2.3)$$

In reality, PS given by Equation 2.1 is called a raw estimate of PS and is not generally accepted as a statistically reliable and robust estimate of the power spectrum of *x(t)*. Computation of PS of real life signals involves obtaining a reliable, smooth, and stable estimate of the raw PS represented by Equation 2.1, across the frequency band of interest.

A stable computation of the PS of a cardiac event time series, such as HRV signal, can be performed using a number of techniques. Among them, Blackman-Tukey (BT) method and autoregressive (AR) procedure are the two most commonly used.

2.4.2 Blackman-Tukey Algorithm for Computing the PS of HRV Signal

The Blackman-Tukey (BT) method is based on the Weiner-Khinchin relationship, which states that the power spectrum, $P_{BT}(f)$, of a signal equals the Fourier transform (FT) of the autocorrelation function (ACF) of the signal. A discrete time version of this relationship can be stated as:

$$P_{BT}(f) = \sum_{k=1}^{n} r_{xx}[k]\exp(-j2\pi fk) \quad -1/2 \le f \le 1/2 \qquad (2.4)$$

where $r_{xx}[k] = E[x_{n+k}x_n^*]$ is the autocorrelation function (ACF) of lag k and n is the number of lags used. The following steps are used for computing the PS (Jenkins and Watts, 1968).

1. Compute the raw spectrum by squaring the FFT of the data.
2. Compute the inverse FFT to obtain the ACF.
3. Multiply the ACF by a lag window, such as the Bartlett window, and truncate the ACF to some specific value.

4. Compute the FFT of the windowed ACF to obtain a smoothed PS using the discrete version of the FFT:

$$P_{BT}(f) = 1/M \sum_{k=-M}^{M} w[k] r_{xx}[k] \exp(-j2\pi fk) \qquad (2.5)$$

where the Bartlett window $w[k] = 1-|k/M|$ and M is the length of the window.

The advantage of the BT method is that a single realization of the random process is adequate to compute PS. If the ACF decays rapidly, a particularly long record is not needed. Finally, the computation of the ACF involves a smoothing operation, which reduces the variance of PS (Bendat and Piersol, 1986).

2.4.3 Autoregressive Modelling for Computing the PS of HRV Signal

In the autoregressive (AR) approach, the signal $x[n]$, at any instant n, is defined as a linear combination of past values plus a disturbance (Kay, 1988):

$$x(n) = -\sum_{k=1}^{p} a(k)x(n-k) + u(n), \quad n = p+1,...,N, \quad N >> p \qquad (2.6)$$

where $a[k]$, $k = 1,2...p$ are the autoregressive parameters used to describe the process that generates the signal. We can gain more insight to the process that generates the signal by investigating from a digital filter viewpoint. For an all-pole filter with output $\{x(n)\}$ defined as shown in Figure 2.7 (a) and the input $\{u(n)\}$ is a white noise sequence, the denominator polynomial $H(z)$ of the filter transfer function is defined as

$$H(z) = 1 + \sum_{k=1}^{p} a_k z^{-k}. \qquad (2.7)$$

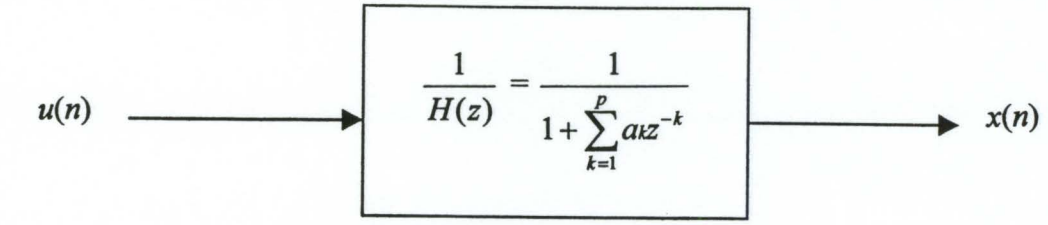

(a)

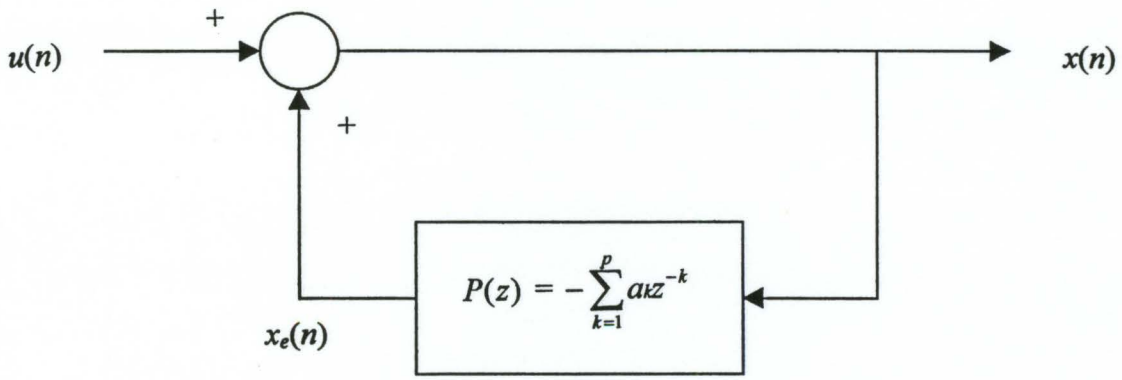

(b)

Figure 2.7 AR process seen from a filter viewpoint: (a) AR process can be seen as the output signal $x(n)$ from an all-pole filter driven by white noise $u(n)$. (b) Alternative interpretation emphasizing the prediction process ($x_e(n)$ is predicted value of $x(n)$). (From Reilly JP, 1998).

Thus the filter transfer function is $\frac{1}{H(z)}$. Taking z-transform of the input-output relationships we have

$$X(z) = \frac{1}{H(z)} U(z) \quad \text{or} \quad X(z)H(z) = U(z). \tag{2.8}$$

Converting the above relationship back into the time domain and realizing that multiplication in the z-domain is convolution in time, we get

$$x(n) + \sum_{k=1}^{p} a(k)x(n-k) = u(n) \tag{2.9}$$

or

$$x(n) = -\sum_{k=1}^{p} a(k)x(n-k) + u(n). \tag{2.10}$$

Notice that the above equation is the same as Equation 2.6. Equations 2.6 and 2.10 show that there are two equivalent interpretations for an AR process: (1) The sequence is defined as a linear combination of past values plus a disturbance; (2) The sequence is the output of an all-pole filter, the input of which is excited by white noise. We can rearrange the block diagram of 2.5 (a) according to 2.5 (b) to emphasize the interpretation of point (1) mentioned above. Note that the polynomial $P(z)$ is given as

$$P(z) = -\sum_{k=1}^{p} a(k)z^{-k}. \tag{2.11}$$

To verify that the overall transfer function of Figure 2.7 (b) is the same as that of Figure 2.7 (a), we realize that the transfer function of Figure 2.7 (b) is given by

$$\begin{aligned} &X(z) = X(z)P(z) + U(z), \\ &\frac{X(z)}{U(z)} \equiv T(z) = \frac{1}{1-P(z)} = \frac{1}{1+\sum_{k=1}^{p} a_k z^{-k}} \end{aligned} \tag{2.12}$$

where $T(z)$ is the transfer function of the system.

The process is termed an autoregressive process in that the sequence $x(n)$ is a linear regression on itself with $u(n)$ representing the error. If we move the weighted summation term to left side of Equation 2.6 and perform z-transform, we get

$$(1+\sum_{k=1}^{p} a[k]z^{-k})X(z) = U(z). \tag{2.13}$$

Rearranging the terms we obtain

$$X(z) = \frac{U(z)}{1+\sum_{k=1}^{p} a[k]z^{-k}} \tag{2.14}$$

and

$$X(f) = X(e^{j2\pi f}) = \frac{U(j2\pi f)}{1+\sum_{k=1}^{p} a[k]e^{-j2\pi fk}} \tag{2.15}$$

where we utilize the relationship between Fourier-transform and z-transform: $z = e^{j2\pi f}$. Since $P_{AR}(f) = |X(f)|^2$ and $U(j2\pi f)$, the power of white noise $u(n)$, is σ^2, AR PS is (Kay and Marple, 1981; Kay, 1988):

$$P_{AR}(f) = \frac{\sigma^2}{(1+\sum_{k=1}^{p} a[k]e^{-j2\pi fk})^2}. \tag{2.16}$$

In order to calculate the AR PS using Equation 2.16, we must first solve the coefficients $a[k]$ in Equation 2.6. In the following, we first explain the idea of prediction error filter (PEF) then describe the derivation of one solution (Yule-Walker equations) to this problem from a matrix computation viewpoint (Reilly, 1998; Kay, 1988). The prediction error filter (PEF) accepts an autoregressive process $x(n)$ as input and outputs the

corresponding prediction error $u(n)$. This filter is obtained from the AR generating filter of Figure 2.7 (a) by interchanging the input and output sequences and inverting the filter transfer function (Figure 2.8 (a)). An equivalent structure making use of the prediction polynomial $P(z)$ is shown in Figure 2.8 (b), where it is clearly shown that the prediction error output $u(n)$ is the difference between the predicted value $x_e(n)$ (subscript e stands for estimate) and the true value $x(n)$.

After illustrating the idea of PEF, we now move on to the derivation of Yule-Walker equations. Equation 2.6 can be expressed in matrix form as

$$\mathbf{x}_p = \mathbf{X}\mathbf{a} + \mathbf{u} \tag{2.17}$$

where

$$\mathbf{x}_p = \begin{bmatrix} x_{p+1} \\ x_{p+2} \\ \vdots \\ x_N \end{bmatrix} \quad \mathbf{u} = \begin{bmatrix} u_{p+1} \\ u_{p+2} \\ \vdots \\ u_N \end{bmatrix} \quad \mathbf{a} = \begin{bmatrix} -a_1 \\ -a_2 \\ \vdots \\ -a_p \end{bmatrix}$$

$$\mathbf{X} = \begin{bmatrix} x_p & \cdots & x_1 \\ x_{p+1} & \cdots & x_2 \\ \vdots & & \vdots \\ x_{N-1} & \cdots & x_{N-p} \end{bmatrix}, \qquad n = p+1, \ldots, N, \quad N >> p.$$

To solve for the coefficients **a**, we use the idea of the PEF. For our purposes, we choose the coefficients **a** to minimize the prediction-error power. This makes the prediction $x_e(n)$ as close as possible to $x(n)$ in the 2-norm sense. The coefficients $\mathbf{a}_{LS}$ (subscript LS stands for least square) found in such a manner minimize $\| \mathbf{x}_p - \mathbf{X}\mathbf{a} \|_2^2$ and are therefore given as the solution to the normal equations:

$$\mathbf{X}^T\mathbf{X}\mathbf{a}_{LS} = \mathbf{X}^T\mathbf{x}_p . \tag{2.18}$$

Taking expectations in Equation 2.18 we get

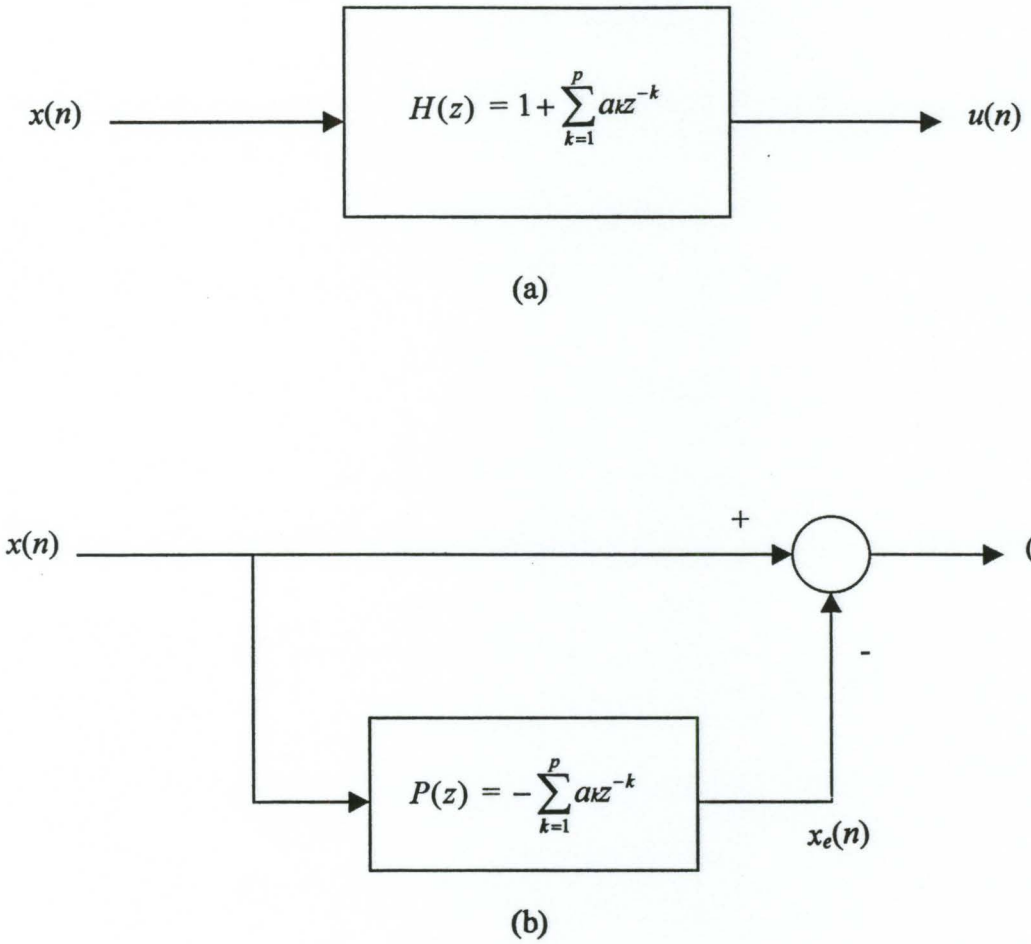

Figure 2.8 Forward prediction-error filter (PEF): (a) Basic configuration of forward PEF. (b) Alternative interpretation emphasizing prediction process. (From Reilly JP, 1998).

$$E(\mathbf{X}^{\mathrm{T}}\mathbf{X})\mathbf{a}_{LS} = E(\mathbf{X}^{\mathrm{T}}\mathbf{x}_p) \tag{2.19}$$

If $\{x(n)\}$ is stationary and ergodic, the matrix $E(\mathbf{X}^{\mathrm{T}}\mathbf{X})$ becomes

$$E(\mathbf{X}^{\mathrm{T}}\mathbf{X}) = \begin{bmatrix} r_{xx}(0) & r_{xx}(-1) & r_{xx}(-2) & \cdots & r_{xx}(-(p-1)) \\ r_{xx}(1) & r_{xx}(0) & r_{xx}(-1) & & \\ r_{xx}(2) & r_{xx}(1) & r_{xx}(0) & \ddots & \\ \vdots & & \ddots & \ddots & \\ r_{xx}(p-1) & & & r_{xx}(1) & r_{xx}(0) \end{bmatrix} = \mathbf{R} \tag{2.20}$$

where $r_{xx}(k) = E[x_{n+k}x_n^*]$ is the autocorrelation function (ACF) of lag k, and $\mathbf{R}$ is the covariance matrix of $\{x\}$. Likewise, from $E(\mathbf{X}^{\mathrm{T}}\mathbf{x}_p)$ in Equation 2.19, we get:

$$E(\mathbf{X}^{\mathrm{T}}\mathbf{x}_p) = \begin{bmatrix} r_{xx}(1) \\ r_{xx}(2) \\ \vdots \\ r_{xx}(p) \end{bmatrix} \equiv \mathbf{r}_p \tag{2.21}$$

Equation 2.19 is therefore represented as

$$\mathbf{R}\mathbf{a}_{LS} = \mathbf{r}_p \tag{2.22}$$

Equation 2.22 is the expectation of the normal equations used to determine the coefficients of a stationary AR process. The finite-sample version of Equation 2.22 is referred to as the Yule-Walker equations (2.23):

$$\begin{bmatrix} r_{xx}(0) & r_{xx}(-1) & \cdots & r_{xx}(-(p-1)) \\ r_{xx}(1) & r_{xx}(0) & \cdots & r_{xx}(-(p-2)) \\ \vdots & \ddots & & \vdots \\ r_{xx}(p-1) & r_{xx}(p-2) & \cdots & r_{xx}(0) \end{bmatrix} \begin{bmatrix} -a_1 \\ -a_2 \\ \vdots \\ -a_p \end{bmatrix} = \begin{bmatrix} r_{xx}(1) \\ r_x(2) \\ \vdots \\ r_{xx}(p) \end{bmatrix}. \tag{2.23}$$

From the regression Equation 2.17, we have

$$\begin{aligned} \sigma^2 &= E(\mathbf{u}^{\mathrm{T}}\mathbf{u}) = E[(\mathbf{x}_p - \mathbf{X}\mathbf{a}_{LS})^T(\mathbf{x}_p - \mathbf{X}\mathbf{a}_{LS})] \\ &= E(\mathbf{x}_p{}^T\mathbf{x}_p - \mathbf{x}_p{}^T\mathbf{X}\mathbf{a}_{LS} - \mathbf{a}_{LS}{}^T\mathbf{X}^{\mathrm{T}}\mathbf{x}_p + \mathbf{a}_{LS}{}^T\mathbf{X}^{\mathrm{T}}\mathbf{X}\mathbf{a}_{LS}). \end{aligned} \tag{2.24}$$

Substituting Equation 2.19 into the above where

$$E(\mathbf{X}^{\mathrm{T}}\mathbf{x}_p) = \mathbf{r}_p = \mathbf{R}\mathbf{a}_{LS}, \tag{2.25}$$

and the fact that $E(\mathbf{x}_p{}^T\mathbf{x}_p) = r_0$ to get

$$\begin{aligned}\sigma^2 &= r_0 - \mathbf{r}_p{}^T\mathbf{a}_{LS} - \mathbf{a}_{LS}{}^T\mathbf{r}_p + \mathbf{a}_{LS}{}^T\mathbf{r}_p \\ &= r_0 - \mathbf{r}_p{}^T\mathbf{a}_{LS}.\end{aligned} \tag{2.26}$$

Combining Equation 2.22 and 2.26 together into one matrix equation as follows:

$$\begin{bmatrix} r_{xx}(0) & r_{xx}(-1) & \dots & r_{xx}(-p) \\ r_{xx}(1) & r_{xx}(0) & \dots & r_{xx}(-(p-1)) \\ \vdots & & & \vdots \\ r_{xx}(p) & r_{xx}(p-1) & \dots & r_{xx}(0) \end{bmatrix} \begin{bmatrix} 1 \\ a_1 \\ \vdots \\ a_p \end{bmatrix} = \begin{bmatrix} \sigma^2 \\ 0 \\ \vdots \\ 0 \end{bmatrix} \tag{2.27}$$

where the first row is given by Equation 2.26 and the remaining rows are given by Equation 2.22 with a new first column coming from the right side of the equation. These equations are called forward prediction-error equations. By varying the forward prediction-error equations, we obtain backward prediction-error equations as

$$\begin{bmatrix} r_{xx}(0) & r_{xx}(-1) & \dots & r_{xx}(-p) \\ r_{xx}(1) & r_{xx}(0) & \dots & r_{xx}(-(p-1)) \\ \vdots & & & \vdots \\ r_{xx}(p) & r_{xx}(p-1) & \dots & r_{xx}(0) \end{bmatrix} \begin{bmatrix} a_p \\ \vdots \\ a_1 \\ 1 \end{bmatrix} = \begin{bmatrix} 0 \\ \vdots \\ 0 \\ \sigma^2 \end{bmatrix}. \tag{2.28}$$

Equations 2.27 and 2.28 can be solved jointly using the Levinson-Durbin recursion (LDR), which requires only $\mathbf{O}(n^2)$ flops comparing to $\mathbf{O}(n^3)$ of Gaussian elimination method. The idea of Levinson-Durbin recursion is to start with a simple 1×1 system of equations. Then by induction we use that result to solve a 2×2 system, and recursively iterate until the solution to a $p \times p$ system is obtained. In summary, the Levinson-Durbin algorithm recursively computes the parameter sets $\{a_1(1), \sigma_1^2\}$,

$\{a_2(1), a_2(2), \sigma_2^2\}$, ..., $\{a_p(1), a_p(2), ..., a_p(p), \sigma_p^2\}$. The final set at order p is the desired solution of the Yule-Walker equations. The recursive algorithm is initiated by

$$a_1(1) = -\frac{r_{xx}(1)}{r_{xx}(0)} \tag{2.29}$$

$$\sigma_1^2 = (1 - |a_1(1)|^2) r_{xx}(0) \tag{2.30}$$

with the recursion for $k = 2, 3, ..., p$ given by

$$a_k(k) = -\frac{r_{xx}(k) + \sum_{l=1}^{k-1} a_{k-1}(l) r_{xx}(k-l)}{\sigma_{k-1}^2} \tag{2.31}$$

$$a_k(i) = a_{k-1}(i) + a_k(k) a_{k-1}^*(k-i), \quad i = 1,2,...,k-1 \tag{2.32}$$

$$\sigma_k^2 = (1 - |a_k(k)|^2) \sigma_{k-1}^2 . \tag{2.33}$$

The form of the algorithm given in Equation 2.31-2.33 is due to Levinson (1947), who formulated an efficient means of solving a hermitian Toeplitz set of equations, and to Durbin (1960), who refined the algorithm to take advantage of the special form of the right-hand-side vector.

One of the difficulties while computing PS using the AR method is that the model order, p, which describes the signal, is not predefined. For the HRV time series recorded during various physiological conditions, the statistical properties of the signal may differ. Hence, there is no single model order that uniformly describes HRV signals recorded from these diverse sources. Changing the model order across different physiological conditions and/or patients may introduce a new variable into the computation of PS. A number of criteria are defined in the literature to assist the selection of the model order (Kay and Marple, 1981; Kay, 1988; 1985). In this thesis we chose a model order between 12-14. This number is supported by Akaike information criterion (AIC) using six sets of

HRV data from healthy subjects (three male and three female, average age: 24±1 years) during both supine and standing condition (Figure 2.9 & 2.10). The AIC is defined as (Akaike, 1974):

$$AIC(k) = N \ln \rho_k + 2k \tag{2.34}$$

where N is the data record length, ρ_k is the estimate of the white noise variance (prediction error power) for the kth order AR model.

2.4.4 Comparison between Autoregressive Modelling & Blackman-Tukey Method

The AR PS usually has higher resolution than BT PS. It is due to an implicit extension of the measured ACF (Kay, 1988). Assume that an AR PS is desired and that the known ACF samples are $\{r_{xx}(0), r_{xx}(1), \ldots, r_{xx}(p)\}$. The AR coefficients are found by substituting the known ACF samples into the Yule-Walker equations and solving. Then the AR PS as defined on the z-plane is

$$P_{AR,e}(z) = \frac{\sigma_e^2}{A_e(z)A_e^*(1/z^*)} = \sum_{k=-\infty}^{\infty} r_{xx,e}(k) z^{-k} \tag{2.35}$$

where the subscript "e" denotes the estimated quantities. It can be shown that the implied ACF $r_{xx,e}(k)$, which is given by the inverse z-transform of $P_{AR,e}$, is

$$r_{xx,e}(k) = \begin{cases} r_{xx}(k) & \text{for } 0 \le k \le p \\ -\sum_{l=1}^{p} a_e(l) r_{xx,e}(k-l) & \text{for } k > p. \end{cases} \tag{2.36}$$

Hence the estimate of the ACF matches the known ACF up to lag p and the remaining samples are extrapolated by a recursive difference equation. In contrast to AR method, BT procedure windows the known ACF sequence and then extrapolates the sequence by appending zeros, thus giving rise to the usual smearing of the spectral estimator. The AR

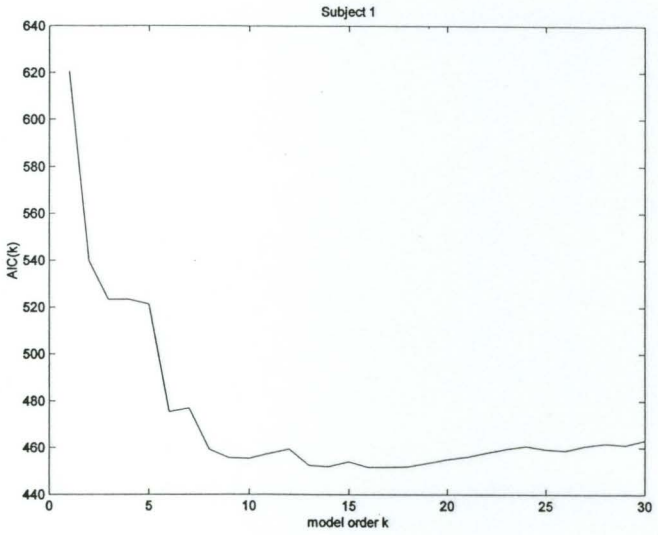

(a)

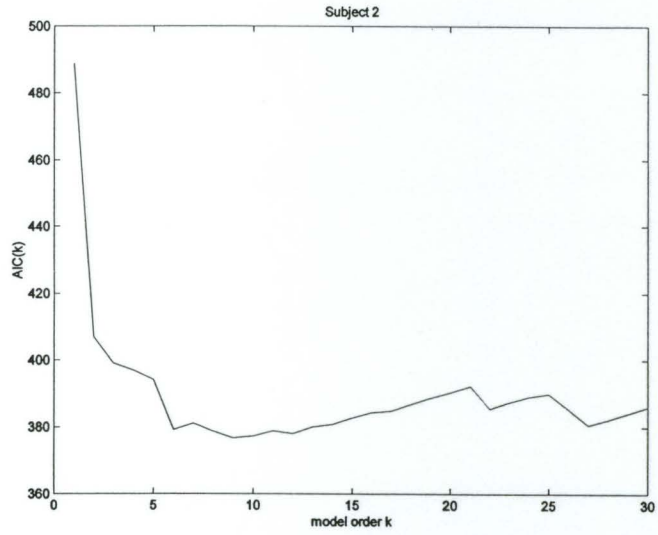

(b)

Figure 2.9 Examples of Akaike information criterion (AIC) in model order selection in six different healthy subjects (*supine position*). The data record length N is 256 and the model order k varies from 0 to 30. It is shown that the *AIC(k)* reaches a minimum around model order 12 for five of the six data sets (except (e)).

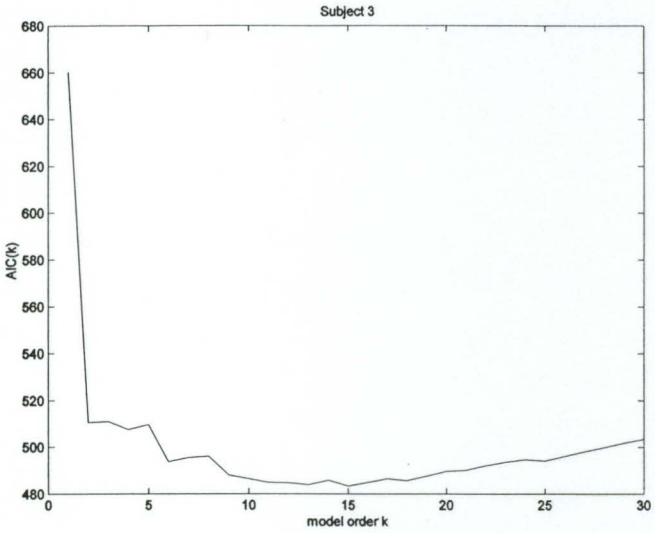

(c)

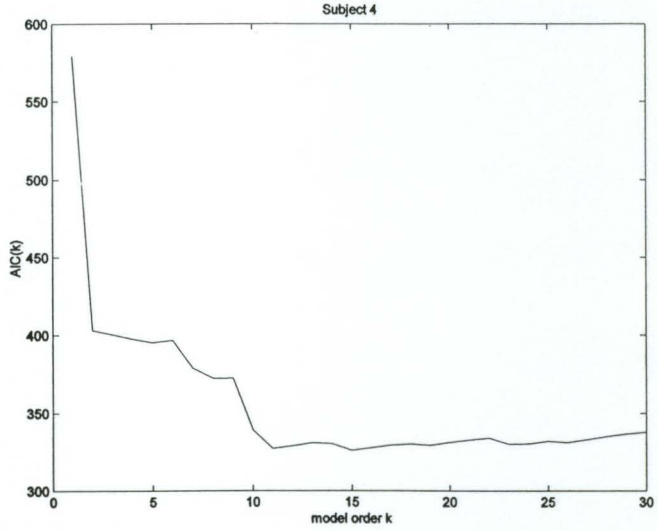

(d)

Figure 2.9 (*contd.*)

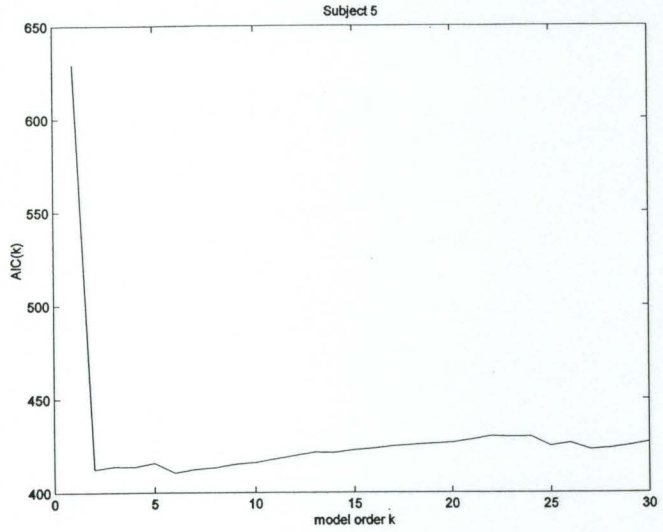

(e)

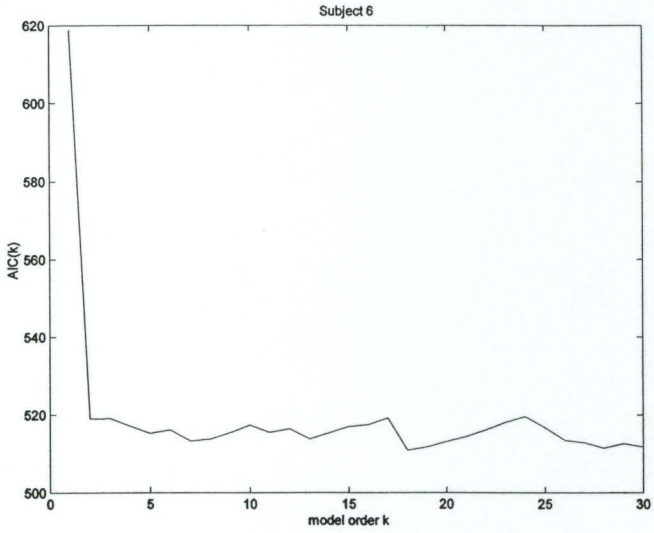

(f)

Figure 2.9 (*contd.*)

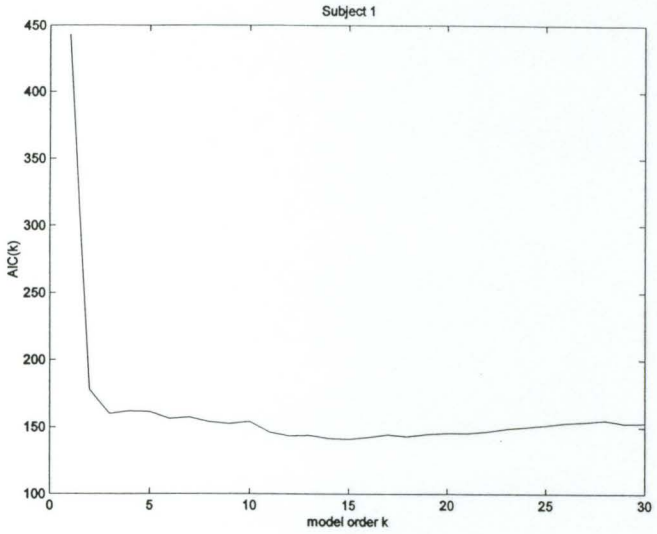

(a)

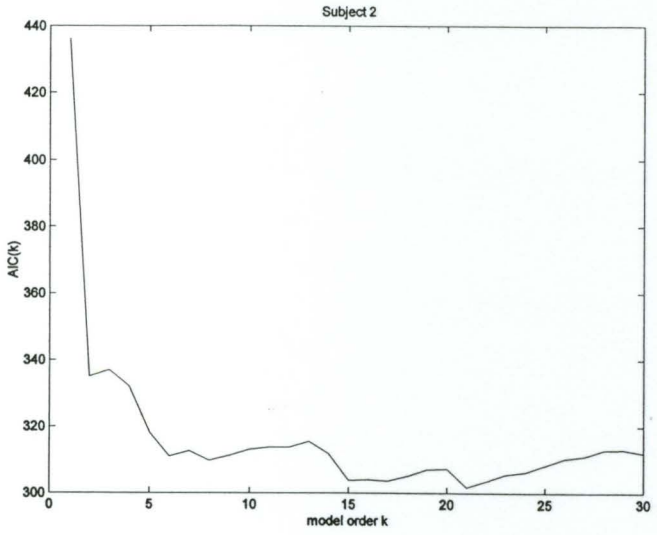

(b)

Figure 2.10 Examples of Akaike information criterion (AIC) in model order selection in six different healthy subjects (*standing position*). The data record length N is 256 and the model order k varies from 0 to 30. It is shown that the $AIC(k)$ reaches a minimum around model order 12 for three of the six data sets ((b), (d), (f)). Out of the other three data sets, two have a model order less than 10 and one has a model order more than 15. Hence the average model order is still around 12.

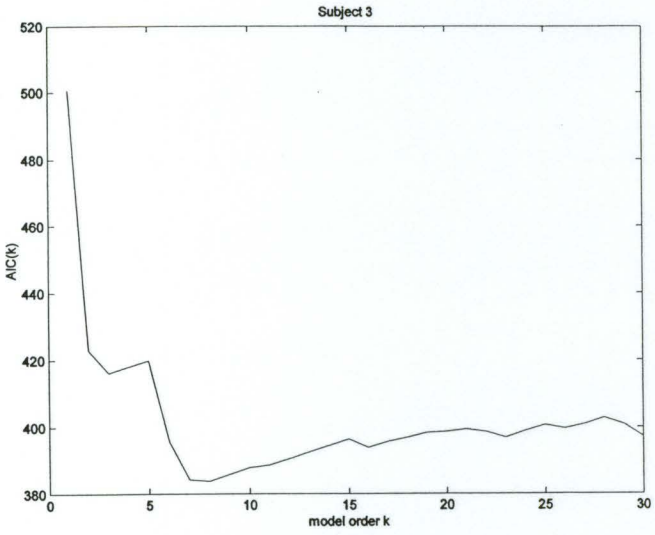

(c)

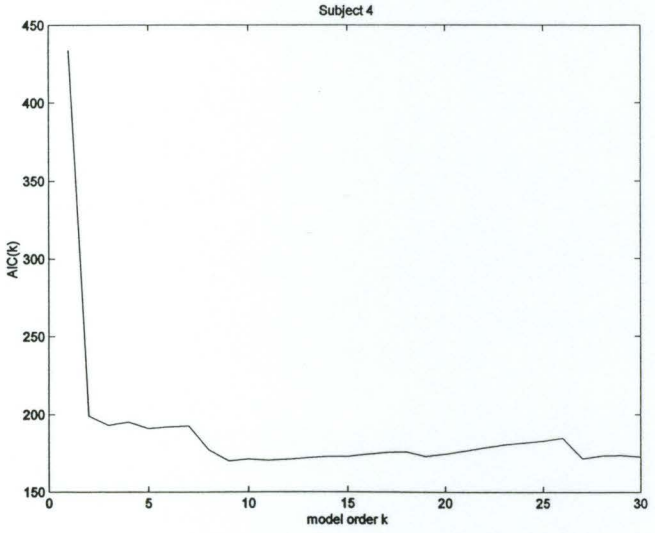

(d)

Figure 2.10 (*contd.*)

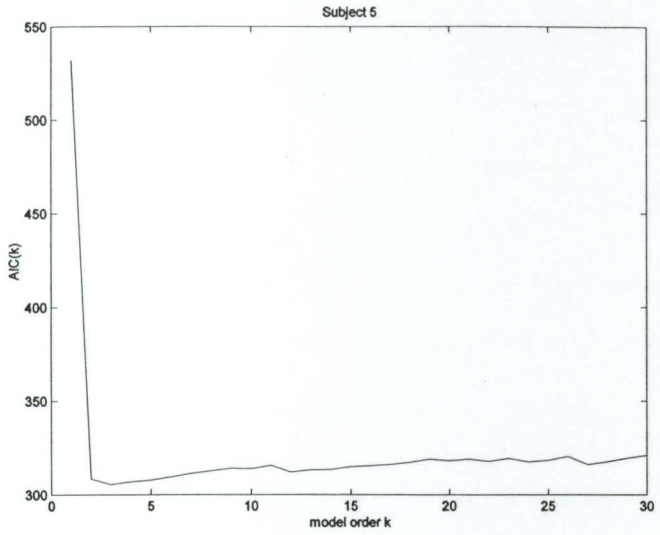

(e)

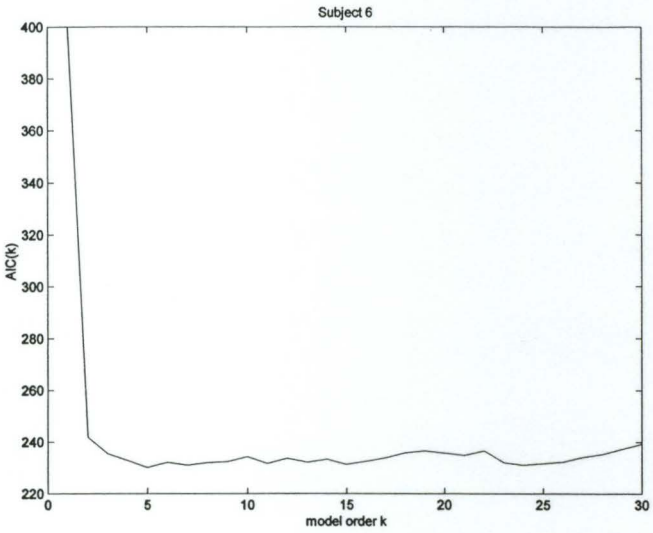

(f)

Figure 2.10 (*contd.*)

spectral estimator extrapolates the autocorrelation sequence according to Equation 2.36. As seen in Figure 2.11, the resultant spectral estimate is a less biased version of the true one. In summary, when the AR modelling assumption is valid, AR PS is less biased and has a lower variability than BT PS (Kay, 1988).

2.4.5 Frequency Bands and their Physiological Relevance

In Figure 2.12 the power spectrum of BT method of a 128 sec long HRV signal under supine condition is shown. It is stated in literature that there are three major frequency bands in the power spectrum in human subjects as well as in unconscious, anesthetized dogs (Sayers, 1973; Akselrod et al., 1981; Kamath and Fallen, 1993). A low-frequency (LF) peak that appears within the spectral band ranging from 0.06 to 0.15 Hz is associated with baroreceptor-mediated blood pressure control and believed to contain mainly a sympathetic component (Akselrod et al., 1981). A high-frequency (HF) peak in the range 0.15 to 0.5 Hz is strongly correlated with parasympathetically mediated respiratory sinus arrhythmia. A very-low-frequency (VLF) peak below 0.05 Hz has been linked with vasomotor control and/or temperature control. In the current study, the very-low-frequency band is removed before the calculation of PS because the frequency resolution in this band is poor and its huge peak usually obscures the study of the other two (LF & HF) bands.

The LF power, calculated by a summation of the power under the PS curve between 0.06 Hz to 0.15 Hz, is an index of the sympathetic modulation of the heart. On the other hand, the HF power, calculated by the same method but between 0.15 to 0.5 Hz band, reflects the modulation of the parasympathetic (or vagal) modulation of the heart.

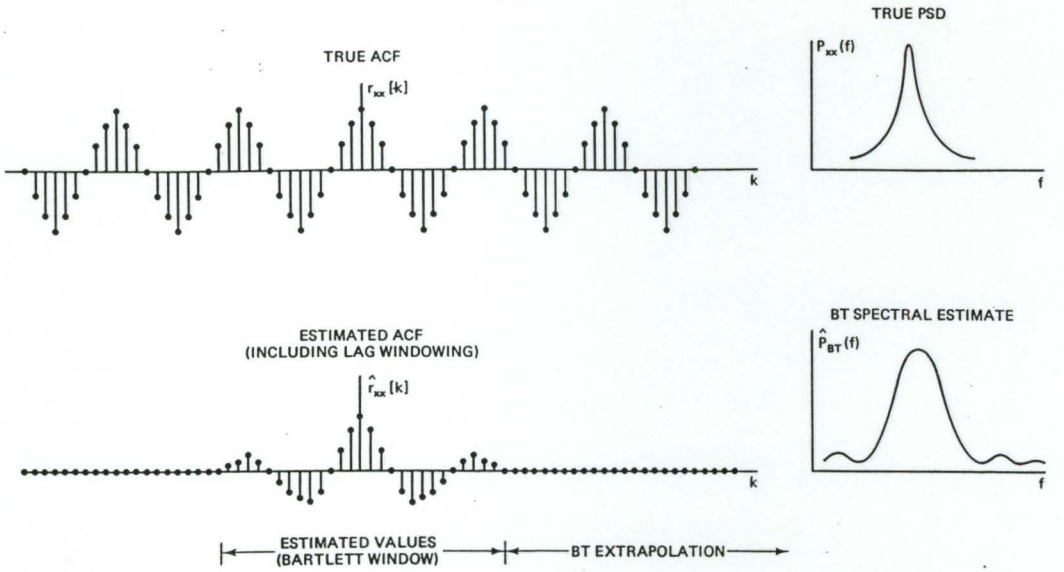

(a)

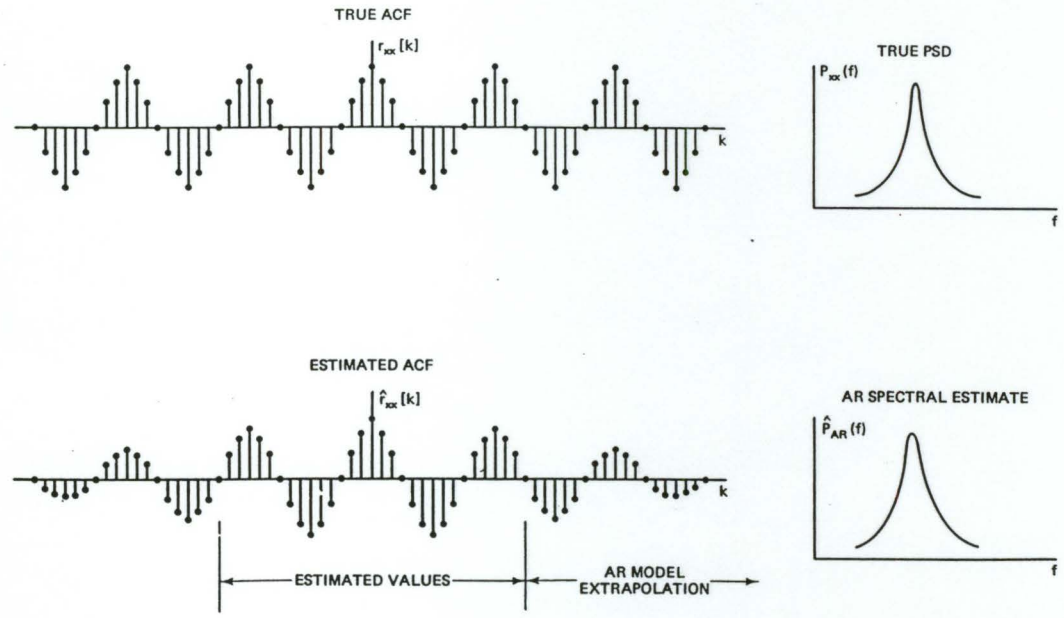

(b)

Figure 2.11 Implied autocorrelation extrapolation of BT & AR power spectrum: (a) BT procedure. (b) AR method. (From Kay SM, *Modern spectral estimation – theory & application*. Prentice-Hall: Englewood Cliffs, NJ, pp. 180-181, 1988).

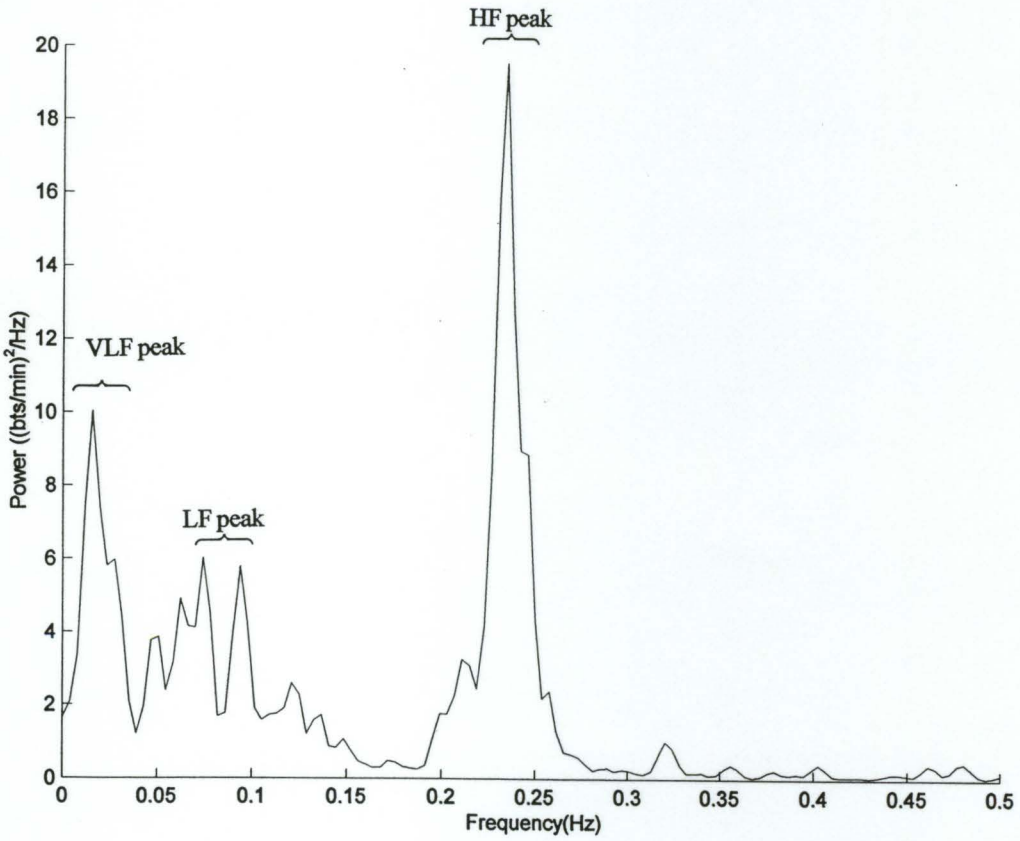

Figure 2.12 Illustration of three major frequency peaks in the Blackman-Tukey power spectrum of HRV signal in a healthy human subject under supine condition. VLF: very low frequency; LF: low frequency; HF: high frequency.

Finally the LF:HF ratio, the ratio between LF power and HF power, is an index of the balance between sympathetic and parasympathetic modulation of the sinus node.

2.5 COMPUTATION OF HRV PS FROM HEALTHY CONTROL SUBJECTS

In this section we demonstrate a step-by-step signal processing procedure to compute the AR & BT power spectrum from the raw ECG signal. A sample ECG signal recorded from a healthy control under supine condition for 5 min is used for analysis. In Figure 2.13 (a)-(f) it is shown that there are six signal processing stages: original ECG signal (2.13 (a)), linear digital bandpass filtering (2.13 (b)), QRS-detection and determination of R-R interval (2.13 (c)), calculation of HR signal (2.13 (d)), interpolation of HR signal (2.13 (e)), and highpass filtering (2.13 (f)).

Comparing power spectra obtained by AR and BT methods (Figure 2.13 (g) & (h)), it is found that the two methods yield similar mean LF:HF ratio throughout the 5 min data but AR power spectra are smoother and have well-defined peaks. Hence it is more helpful in identifying the central frequency (defined as the frequency corresponding to the peak in the PS).

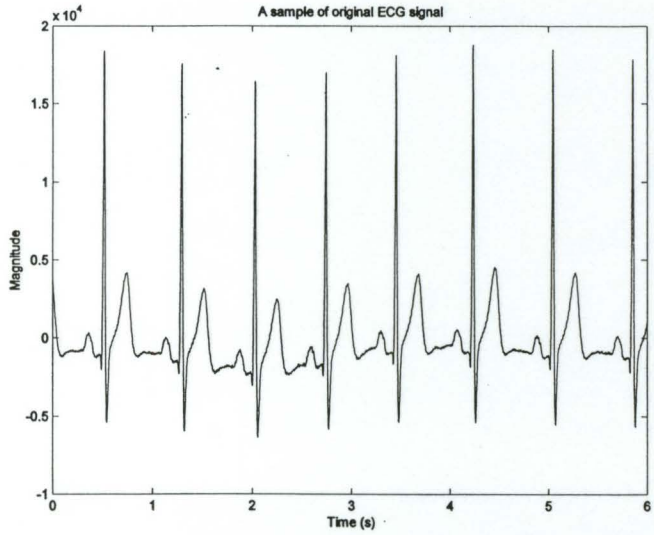

(a)

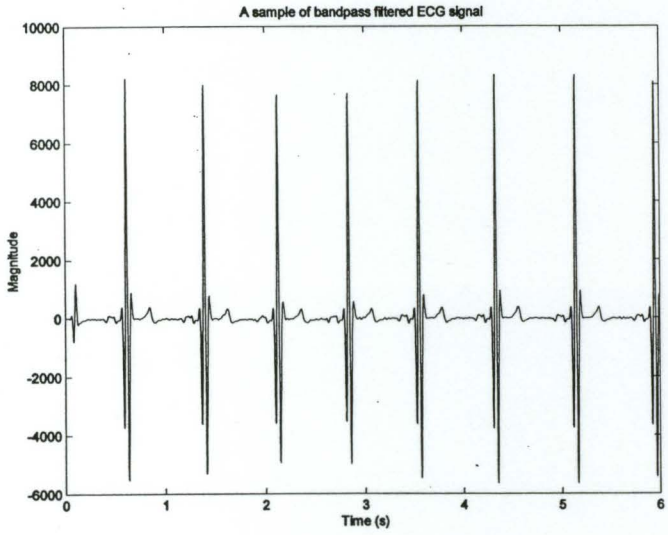

(b)

Figure 2.13 Signal processing results obtained from a five min long sample ECG signal under supine condition: (a) A sample of original ECG signal (6 sec). (b) A sample of ECG signal after linear bandpass filtering (6 sec). (c) R-R interval signal. (d) Instantaneous heart rate signal. (e) Interpolated heart rate signal. (f) Highpass filtered heart rate signal (i.e. the very low frequency (0-0.025 Hz) component is removed). (g) AR power spectra (128 sec data / power spectrum). (h) BT power spectra (128 sec data / power spectrum.

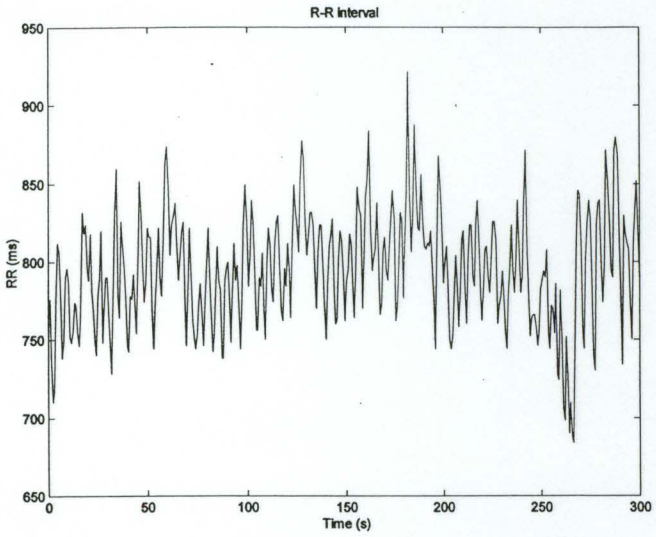

(c)

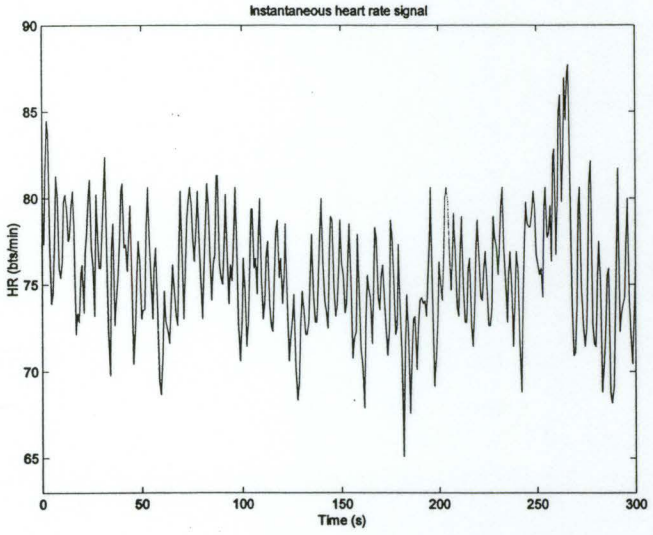

(d)

Figure 2.13 (*contd.*)

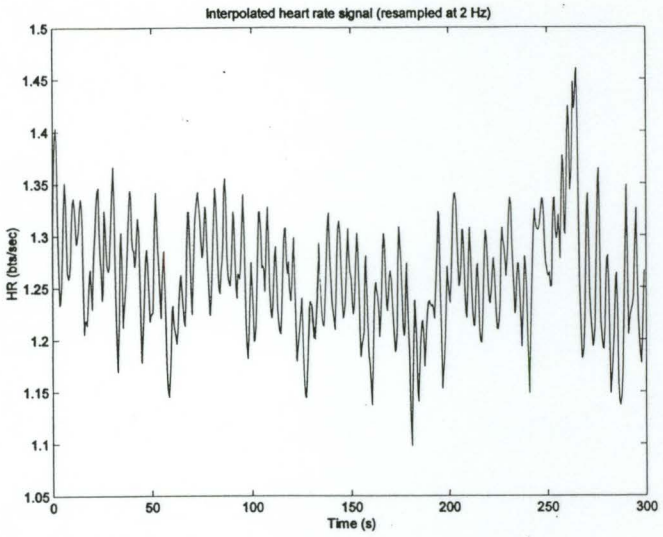

(e)

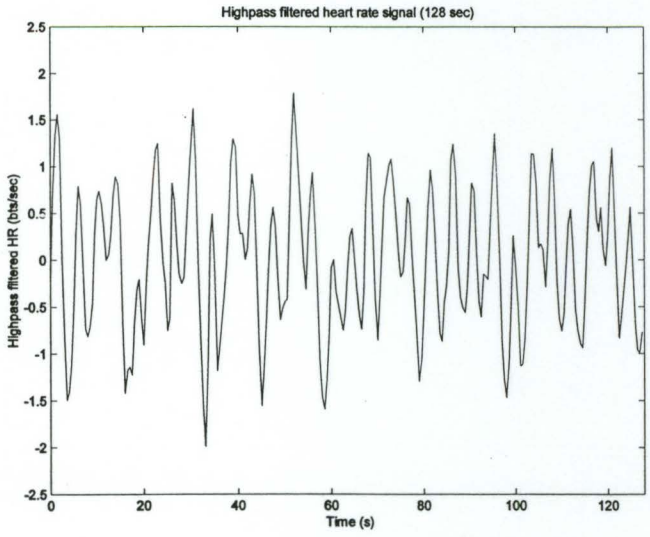

(f)

Figure 2.13 (*contd.*)

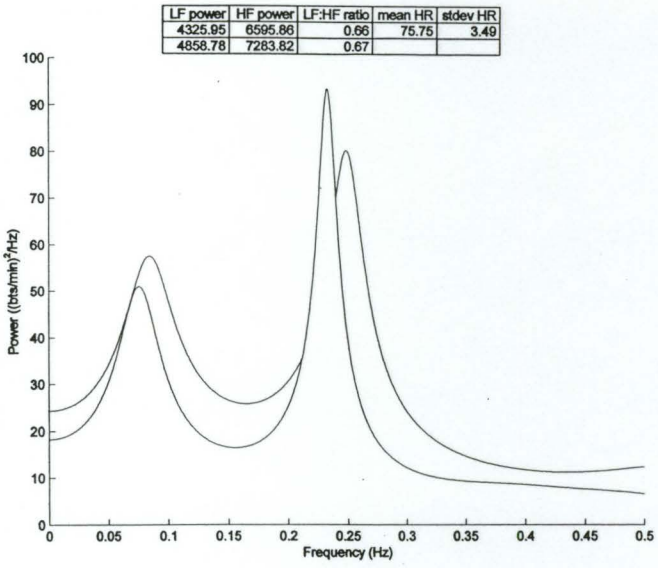

(g)

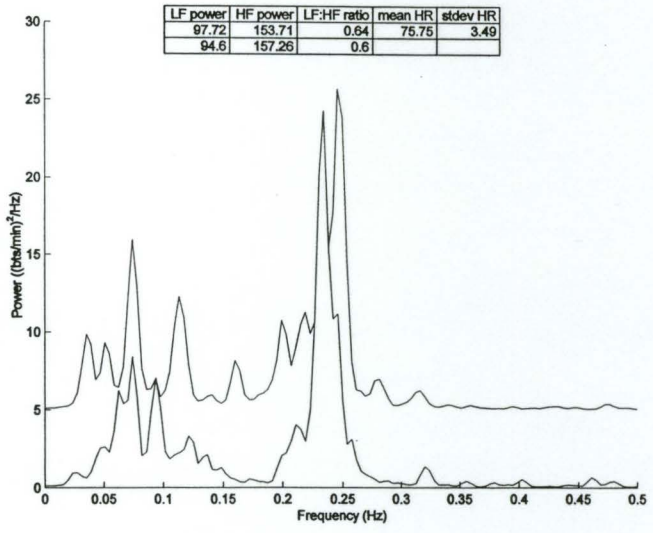

(h)

Figure 2.13 (*contd.*)

Chapter 3

Theory and Software Implementation of Time-Frequency Distribution

3.1 BACKGROUND

The usefulness of time-frequency distribution (TFD) in Medicine is based on the nonstationary nature of most physiological signals. Signals recorded from human subjects are a function of a number of biological variables. For example, physiological conditions such as exercise, and postural changes do not satisfy the criteria for stationarity, a basic assumption while computing power spectra using traditional methods such as Blackman-Tukey (BT) algorithm or autoregressive (AR) procedure (Kamath and Fallen, 1993). New techniques from the class of time-frequency distributions include Wigner-Ville distribution (WVD), wavelet transform (WT), short-time Fourier transform (STFT) may prove to be more relevant while dealing with nonstationary signals. Among these methods, Wigner-Ville distribution provides the most accurate estimate with the highest frequency resolution (Novak et al., 1997). The smoothed Wigner-Ville distribution has

been demonstrated to be a good estimation method for short nonstationary time series (Novak et al., 1997). Its resolution is enhanced by independent time and frequency smoothing using a moving N-event data window (Novak et al., 1993). This chapter describes Wigner-Ville distribution and its implementation for analyzing the HRV signal.

Time-frequency distributions map a one-dimensional signal into a two-dimensional function of time and frequency. They are conceptually similar to a musical score with time running along one axis and frequency running along the other axis (Lin and Chen, 1996). The time-frequency plane gives an indication of which spectral components are present at any time instant. Hence this technique permits one to understand and describe situations elegantly where the frequency content of a signal is changing with time.

The time-frequency distributions of a signal can be divided into two main classes: linear (please see Equation 3.3 for an example) and quadratic time-frequency distributions (please see Equation 3.9 below) (Hlawatsch and Boudreaux-Bartels, 1992; Cohen, 1989). Comparing Equation 3.3 and 3.9 we can see that a fundamental difference is the signal order utilized in the integrals. For the linear distribution, an integral of first order signal terms is used, while for quadratic method an integral of second order terms is computed. From a signal processing point of view, a linear time-frequency distribution means that if a signal is a linear combination of some frequency components, its time-frequency distribution is the same linear combination of each individual TFD component. Linearity is a desirable property in any application involving multi-component signals. Unfortunately the most commonly used linear method STFT has a crucial drawback, i.e., there is tradeoff between time and frequency resolutions. A longer window length gives

better frequency resolution but poorer time resolution, while a shorter window length gives better time resolution but poorer frequency resolution. Unfortunately, both time and frequency resolutions cannot be improved simultaneously.

On the contrary, the quadratic methods do not satisfy the property of linearity but are able to improve the time and frequency resolutions simultaneously. This group of methods includes the Wigner-Ville distribution, the exponential distribution (ED), and the reduced interference distribution (RID) (Chen and Lin, 1996).

The following is an example of the non-linear property of WVD. Assume *x(t)* contains two sinusoids of frequency f_1, f_2 as:

$$x(t) = A_1 \exp(j2\pi f_1 t) + A_2 \exp(j2\pi f_2 t), \quad f_2 \geq f_1 \tag{3.1}$$

The WVD can be shown to be (Garudadri, 1987):

$$\begin{aligned} W_f(t,f) &= 2\pi A_1^2 \delta(f - f_1) + 2\pi A_2^2 \delta(f - f_2) \\ &\quad + 4\pi A_1 A_2 \cos(2\pi(f_2 - f_1)t)\delta(f - \frac{1}{2}(f_1 + f_2)), \quad f_2 \geq f_1 \end{aligned} \tag{3.2}$$

where $\delta(f - f_i)$ is an impulse centered at $f = f_i$. It can be seen that the WVD of a two-component signal contains not only the addition of the WVD of two single-component signals but also an extra term whose frequency lies in the middle of the two original frequency components. The extra item is called cross-term. It makes the interpretation of WVD difficult. However, Equation 3.2 also reveals that the amplitude of the cross-term is oscillating along time, which suggests we might use time smoothing to remove the cross-term.

3.2 ALGORITHMS

3.2.1 Short-Time Fourier Tansform

The STFT is a natural extension of the ordinary Fourier transform. It localizes the frequency components in time by sliding a window, *h(t),* along the signal *x(t)* and then taking the Fourier transform as shown below:

$$X(t,f) = \int_{-\infty}^{+\infty} x(\tau)h(t-\tau)e^{-j2\pi f\tau}d\tau \tag{3.3}$$

By moving the window *h(t),* this process maps the signal into a two-dimensional function in a time-frequency plane. The main advantage of this method is its ease of implementation and application of fast Fourier transform algorithm for its computation (Lin and Chen, 1996). It is the most efficient method for computing a time-frequency mapping of a one dimensional signal varying with time. Furthermore, it is evident that the STFT is a linear time-frequency representation. However, the crucial drawback inherent in the STFT method is that there is tradeoff between time and frequency resolutions. For a particular signal, a particular window may be more appropriate (to yield better resolution) than another. If there is a signal that consists of two distinct signal components, each requires its own window for best results, clearly one window will not suffice. Therefore, one needs to test the type and the length of the window according to the practical situation. The spectrogram of a signal is defined as the squared magnitudes of the linear STFT (Lin and Chen, 1996):

$$SPEC(t,f) = \left| \int_{-\infty}^{+\infty} x(\tau)h(t-\tau)e^{-j2\pi f\tau}d\tau \right|^2 \tag{3.4}$$

The difference between the spectrogram and STFT is that STFT is linear signal decomposition and there are no cross-terms between signal components. However, the

spectrogram (Equation 3.4) is a bilinear signal energy distribution due to the magnitude squaring operation. Thus, the spectrogram also has cross-terms.

3.2.2 Quadratic Time-Frequency Distribution

In the definition of quadratic time-frequency transforms, the basic required condition will be determination of a two-dimensional function of time and frequency, which should represent an energy density per unit time and unit frequency. Thus, the energy associated with the time and frequency intervals Δt and Δf, respectively, would be defined by $\rho(t,f)\Delta f\Delta t$. However, point by point definition of time-frequency energy densities in the time-frequency plane is not possible, since the uncertainty principle prevents us from defining the concept of energy at a specific instant and frequency. This is the reason why some more general conditions are considered. Namely, one requires that the integral $\rho(t,f)$ over *f*, for a particular instant of time should be equal to the instantaneous power of the signal; while the integral over time for particular frequency should be equal to the spectral energy density function. These conditions are known as marginal properties (Stancovic, 1994). In summary, it is desirable that time-frequency distribution of a signal *z(t)* satisfies the following basic properties (Cohen, 1992):

$$\int_{-\infty}^{+\infty}\int_{-\infty}^{+\infty}\rho(t,f)dfdt = E \tag{3.5}$$

$$\int_{-\infty}^{+\infty}\rho(t,f)df = |z(t)|^2 \tag{3.6}$$

$$\int_{-\infty}^{+\infty}\rho(t,f)dt = |Z(f)|^2 \tag{3.7}$$

where *E* and *Z(f)* denote the energy and the Fourier transform of *z(t)* respectively.

3.2.3 A General Class of Quadratic Time-Frequency Distributions

Most popular time-frequency representations can be expressed in terms of the general quadratic time-frequency representation proposed by Cohen (1966, in a quantum mechanics context). This is defined as (Boashash, 1991):

$$\rho_z(t,f) = \int_{-\infty}^{+\infty}\int_{-\infty}^{+\infty}\int_{-\infty}^{+\infty} e^{j2\pi\upsilon(u-t)} g(\upsilon,\tau) z^*(u-\frac{1}{2}\tau) z(u+\frac{1}{2}\tau) e^{-j2\pi f\tau} d\upsilon du d\tau \qquad (3.8)$$

where *z(t)* is the analytic signal and $g(\upsilon,\tau)$ is termed kernel defining a particular distribution. Different kernels produce different distributions, such as the Wigner-Ville distribution, the spectrogram, the exponential distribution, and the reduced interference distribution. Desirable distribution properties and associated kernel requirements (sufficient conditions) are summarized in Table 3.1 (Lin and Chen, 1996). Once a kernel is chosen, the distribution is fixed. Table 3.2 illustrates how two commonly used distributions satisfy the desirable properties as defined in Table 3.2. Please note in Table 3.2, 'P1, P2, …, P10' refer to properties listed in Table 3.1.

Table 3.1 Desirable distribution properties

Properties	**Mathematical expressions**
P1 – real-valued	$\rho_z(t,f) = \rho_z^*(t,f)$
P2 – time shift	If $f(t) = z(t-t_o)$, then $\rho_f(t,f) = \rho_z(t-t_o,f)$
P3 – frequency shift	If $f(t) = z(t)\exp(j2\pi f_o t)$ then $\rho_f(t,f) = \rho_z(t,f-f_o)$
P4 – time marginal	$\int_{-\infty}^{+\infty} \rho_z(t,f)df = \lvert z(t)\rvert^2$
P5 – frequency marginal	$\int_{-\infty}^{+\infty} \rho_z(t,f)dt = \lvert Z(f)\rvert^2$
P6 – instantaneous frequency	$[\int_{-\infty}^{+\infty} f\rho(t,f)df]/[\int_{-\infty}^{+\infty} \rho(t,f)df] = f_i(t)$
P7 – group delay	$[\int_{-\infty}^{+\infty} t\rho(t,f)dt]/[\int_{-\infty}^{+\infty} \rho(t,f)dt] = \tau_g(f)$
P8 – time support	If $z(t) = 0$ for $\lvert t\rvert > T$, then $\rho_z(t,f) = 0$ for $\lvert t\rvert > T$
P9 – frequency support	If $Z(f) = 0$ for $\lvert f\rvert > 2\pi\Omega$, then $\rho_z(t,f) = 0$ for $\lvert f\rvert > 2\pi\Omega$
P10 - nonnegativity	$\rho_z(t,f) \geq 0$

Table 3.2 Comparison between two bilinear distributions

Name	**Kernel**	**P1**	**P2**	**P3**	**P4**	**P5**	**P6**	**P7**	**P8**	**P9**	**P10**
WVD	1	x	x	x	x	x	x	x	x	x	
spectrogram	$\int_{-\infty}^{+\infty} w(u-1/2\tau)e^{-j2\pi\theta u} \cdot w(u+1/2\tau)du$	x	x	x							x

3.2.4 Wigner-Ville Distribution

The concept of WVD was introduced by Wigner in the field of physics and incorporated into signal analysis by Ville (1948). A general definition of the continuous WVD of any complex function *z(t)* is given by:

$$W_z(t,f) = \int_{-\infty}^{+\infty} z(t+\tau/2)z^*(t-\tau/2)e^{-j2\pi ft}d\tau \qquad (3.9)$$

where t is the time domain variable and f is the frequency variable. The * denotes the complex conjugate. This estimator is sometimes referred to as the Wigner distribution (WD) if *z(t)* is a real function. The WVD yields high resolution in both time and

frequency and has several nice properties, including preservation of time and frequency support, instantaneous frequency, group delay, etc. (see Table 3.2). WVD also gives a remarkably good result for the linear chirp signal:

$$x(t) = \prod_T(t)\cos 2\pi(f_o t + \alpha t^2/2) \tag{3.10}$$

where $\prod_T(t)$ is a rectangular function of unit amplitude and duration T. Figure 3.1 (a) illustrates one linear chirp signal with the parameters: T = 500(s), f_o= 0(Hz), α = 0.001 (signal sampling rate is 2Hz). The 2-D contour plot of the WVD is illustrated in Figure 3.1 (b). The range of the frequency is from 0-0.5 Hz, which models the frequency range of the heart rate variability signal.

The main drawback of the WVD is that it produces cross-terms (or interference) if the signal contains more than one frequency component due to its quadratic nature (see Equation 3.2). Besides, the WVD is generally not fully positive for the total range of time and frequency, which obscures its physical interpretation (Cohen, 1992). We can minimize these problems as follows: a) we can use an analytic signal instead of real signal to suppress cross-terms between positive and negative frequencies and b) we can perform time and frequency smoothing to suppress regions where spectra are negative and also reduce cross-terms.

3.2.5 Necessity and Calculation of Analytic Signal

In most practical cases, the signals to be analyzed consist only of real values. In these cases it is necessary to form the corresponding analytic signal. To see the importance of using the analytic signal, consider the Wigner distribution (WD) defined by:

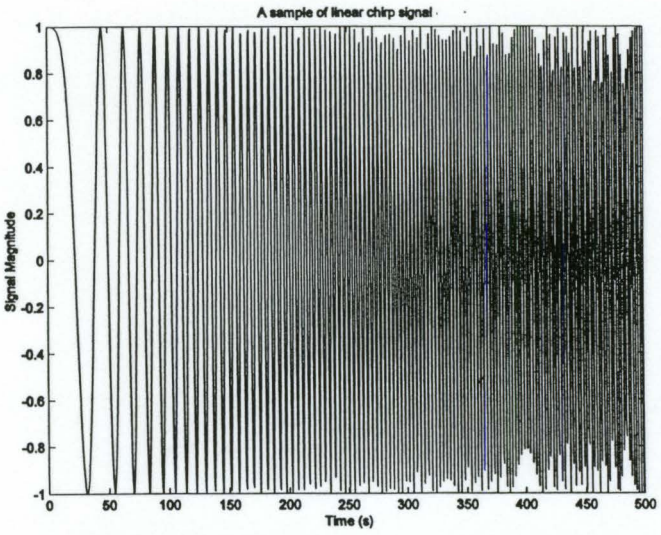

(a)

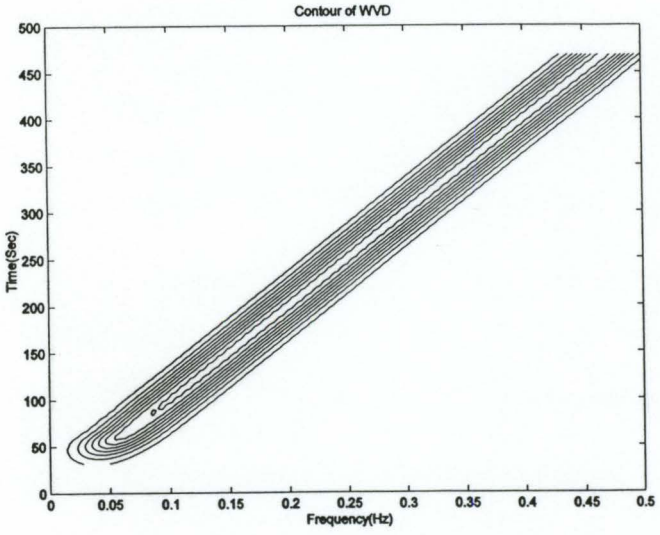

(b)

Figure 3.1 A sample of linear chirp signal: (a) Signal in time domain. (b) 2-D contour plot of Wigner-Ville distribution.

$$W_x(t,f) = \int_{-\infty}^{+\infty} x(t+\tau/2)x^*(t-\tau/2)e^{-j2\pi f\tau}\,d\tau \qquad (3.11)$$

where *x(t)* is the real signal to be analyzed. This distribution differs from the Wigner-Ville distribution (Equation 3.9) by its use of the real signal, *x(t),* instead of the analytic signal, *z(t).* The relationship between the Wigner distribution and Wigner-Ville distribution is (Boashash B., 1991):

$$W_x(t,f) = \frac{1}{4}[W_z(t,f) + W_z(t,-f)] + \gamma(t,f) \qquad (3.12)$$

where $\gamma(t,f)$ represents the cross-terms between positive and negative frequencies and is oscillatory in nature. For example, if *x(t)* is the chirp signal of Equation 3.10, then (Boashash, 1991):

$$\gamma(t,f) = \frac{1}{\sqrt{2a}}\prod_T(t)\prod_{B'}(f)\cos 2\pi\left(\frac{f^2}{\alpha} - 2f_o t - \alpha t^2 - \frac{1}{8}\right) \qquad (3.13)$$

where $\prod_T(t)$ is a rectangular function of unit amplitude and duration T and $B' = B(1-2|t|/T)$ *and* $\alpha = B/T$. From the above example, we can clearly see that the WVD will produce cross-terms between positive and negative frequencies if we do not use the analytic signal.

The analytic signal *z(n)* corresponding to *x(n)* is defined in the discrete time domain as:

$$z(n) = x(n) + jH[x(n)] \qquad (3.14)$$

where H[x*(n)*] represents the Hilbert transform of *x(n).* Alternatively, the analytic signal can be defined in the frequency domain as:

$$Z(f)=\begin{cases}2X(f), & 0<\mathrm{f}<1/2\\ X(f), & \mathrm{f}=0\\ 0, & -1/2<\mathrm{f}<0.\end{cases} \tag{3.15}$$

There are two main methods to obtain an analytic signal from a real world and in our case, a physiological signal. A direct method is to use its frequency definition: a signal with no negative frequency components. That is, form the Fourier transform of the signal, set the negative frequency values to zero, and perform the inverse Fourier transform. Another method is to use a Hilbert transform filter to produce the required complex component of the signal, which when added to the real part produces the desired analytic signal as given by Equation 3.14. Hilbert transform filter has the ideal impulse response given in Equation 3.16.

$$h(n)=\begin{cases}\dfrac{2\sin^2(\pi n/2)}{\pi n} & \text{for } \mathrm{n}\neq 0\\ 0, & \text{for } \mathrm{n}=0\end{cases} \tag{3.16}$$

3.2.6 Time and Frequency Smoothing

As mentioned previously, in order to suppress negative regions and cross-terms it is necessary to apply smoothing in the time and frequency domain. Theoretically the smoothing process is a 2-D convolution of the WVD with a function *G(t,f)* given by (Garudadri, 1987):

$$W(t,f)=\frac{1}{2\pi}\int_{-\infty-\infty}^{+\infty+\infty}\int W(\tau,\xi)G(t-\tau,f-\xi)d\tau d\xi \tag{3.17}$$

It is shown that using *G(t,f)* as definied below (DeBruijin, 1967) can help the situation:

$$G(t,f)=\frac{1}{T\Omega}e^{-t^2/T^2}e^{-4\pi f^2/\Omega^2} \tag{3.18}$$

With $T\Omega \geq 1$, the Equation 3.17 yields a positive WVD. Here, T and Ω define the amount of smear in the time and frequency domains respectively. Such a smoothed WVD has no cross-terms and no negative regions. The price paid is a smear in the time and frequency domain and a loss in the phase information. However, partially smoothed WVD has proved to be a very useful tool (Garudadri, 1987).

Large computational savings can be achieved by computing the smoothed WVD directly, rather than computing the WVD and then performing a 2-D convolution. In analog form, the smoothed WVD is given directly by (Garudadri, 1987):

$$W_z(t,f) = \int_{-\infty}^{+\infty} |h(\tau/2)|^2 \int_{-\infty}^{+\infty} z(t+\tau/2-\tau')z^*(t-\tau/2-\tau')g(\tau')d\tau' e^{-j2\pi f\tau} d\tau \quad (3.19)$$

where t is the time variable and f is the frequency variable, $g(\tau')$ and $h(\tau/2)$ are the time and frequency smoothing window respectively. For discrete signals, the smoothed WVD is given by (Novak, 1993):

$$W_z(n,m) = \frac{1}{2} N \sum_{k=0}^{N-1} |h(k)|^2 \left[\sum_{p=-M}^{M} g(p)z(n+p+k)z^*(n+p-k) \right] e^{-j2\pi km/N} \quad (3.20)$$

where n is the time index, m is the frequency index, $g(p)$ and $h(k)$ are time and frequency smoothing windows respectively. M is the parameter defining the time smoothing window width and N is the time window over which a spectral estimation is calculated.

3.2.7 Choice of the Smoothing Windows

In order to use Equation 3.20 to produce the smoothed Wigner-Ville distribution of a given signal, we must decide the window shape and corresponding parameters. For our specific application, a rectangular time window $g(p)$ with length $2M+1$ ($M = 9$) (Novak, 1993) and a Gaussian frequency window $h(k)$ with length N ($N = 127$) have been

chosen. Note first that the length of the time window *g(p)*, *2M+1*, is much shorter than *N* in this case. Also the time window *g(p)* is centered at the actual time index, *n*, (see Equation 3.20, *p=-M, ..., +M*). Therefore this smoothing method is able to provide a good time resolution. The Gaussian frequency window *h(k)* is given by:

$$h(k) = e^{-\frac{(k-N/2)^2}{2(N/10)^2}} \qquad 0 \le k \le N-1 \qquad (3.21)$$

With these parameters, it has been possible to generate reliable estimates of time-frequency distributions that follow the signal structure particularly well under nonstationary conditions. Moreover, they allow a better evaluation of the frequency content of transitory periods that cannot be obtained otherwise (Novak et al., 1993).

3.3 SOFTWARE PACKAGE FOR COMPUTING THE TFD

3.3.1 Overview of Software Package

We have developed a C++ software package called **Wigner95**, to compute and display Wigner-Ville distribution of the heart rate variability signal. **Wigner95** is written in Visual C++ language and developed in Microsoft Visual Studio97. Its main purpose is to compute the Wigner-Ville distribution in an efficient, user-friendly and intuitive fashion in a Windows95 environment. Modern object-oriented programming (OOP) principles have been incorporated. Furthermore careful documentation will enable one to extend or upgrade the package in the future. The package has been tested for simulated and real world physiological data, namely the HRV.

3.3.2 Software Design

Initially, a software package for computing Wigner-Ville distribution was developed using MATLAB. Experience gained from this exercise led me to define the specifications for **Wigner95**. Two important software engineering concepts have been utilized right from the beginning of the software development, i.e. modularization and object-oriented programming. First, in order to achieve modularization, the software design task is divided into four modules, i.e. Main Application Module, User Input Module, Data Analysis Module and Graphical Output Module. Their relationship is illustrated in Figure 3.2. Notice the user-computer interaction takes place in the two-way control between Main Application Module and User Input Module. The Graphical Output Module can be influenced by either Main Application Module (when program first starts) or User Input Module (when user intentionally click a button).

Functions of individual modules are as follows. Main Application Module is used to initialize, organize and direct all the windows and standard function calling. User Input Module is intended to get input from the user, such as to get the name of the target data file. Data Analysis Module performs an extensive mathematical calculation on the input R-R interval signal and transform it into the joint time-/frequency- domain mapping. This module is the inner core of the software and contains a lot of user-defined functions. Lastly User Output Module is used to display warning/help boxes and the figures to inform user the state of the program and demonstrate the results of the internal processing respectively. It also produces hardcopies of all the figures. Due to the need of a comprehensive demonstration, it includes many user-defined drawing functions.

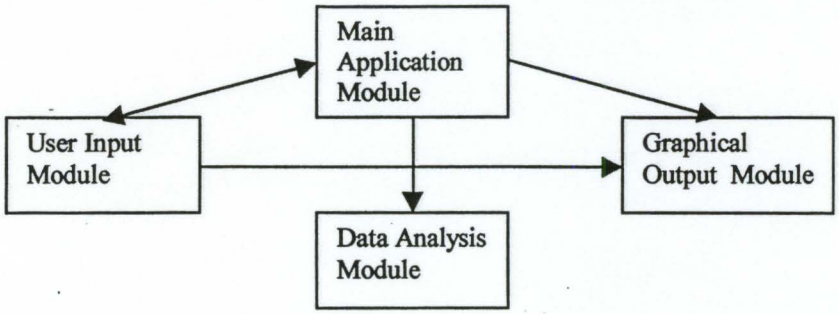

Figure 3.2 Relationship between four modules

Second, in order to utilize the concept of object-oriented programming, one needs to understand the concept of class. A class is an entity that groups data and functions together to perform a task. A module may contain as many classes as it needs. The relationships between different modules and the classes of **Wigner95** are shown in Table 3.3.

Table 3.3 Relationship between modules and classes

Modules	**Related classes**
Main Application	CWigner95App, CMainFrame, CChildFrame
User Input	CIrrnameDlg, CPatientDlg
Data Analysis	CWigner95Doc
Graphical Output	CPlotRR_WVD, CPlotLfHfVw, CWarnDlg, CAboutDlg

3.3.3 Design of Main Application Module

The Main Application Module includes an application class (CWigner95App), a main frame class (CMainFrame) and a child frame class (CChildFrame). Functions of the application class include starting up the software package, carrying out the initialization of the windows and displaying the main frame window. In order to perform a user-defined function, we add functionality to the existing Microsoft Foundation Class (MFC) library. The two related functions in the application class are listed in Table 3.4.

Table 3.4 Functionality added in two functions of application class

Function name	**Functionality added**
InitInstance()	Definition of two Multiple Document Template pointers, whose functions are to group the document class, view class and window
OnFileNew()	Direct the command flow to the Data Analysis Module when user first starts the program

The main frame class (CMainFrame) and child frame class (CChildFrame) control all frame features of the windows such as the menu bar, toolbar and icons. The most important purpose of these classes is to create new windows or to activate existing ones.

These operations are invoked by window messages, and the proper classes must be arranged to receive and act on these messages. The description of these actions is listed in Table 3.5.

Table 3.5 Description of operations in frame window class

Function acting on window message	**Class being served**	**Operation**
OnViewLfhflfhf()	CPlotLfHfVw	Create or activate window of the figure of LF power, HF power, LF:HF ratio, R-R interval versus time
OnViewRrwvd()	CPlotRR_WVD	Create or activate window of the contour figure of Wigner-Ville distribution

3.3.4 Design of User Input Module

In general, User Input Module must provide an intuitive interface between the user and the software. In **Wigner95**, two task-oriented dialog boxes are created in order to achieve that goal and they are related to two dialog classes, i.e. CPatientDlg and CIrrnameDlg. These are accomplished by the aid of Microsoft visual resource editor.

3.3.5 Design of Data Analysis Module

The purpose of the **Wigner95** software package is to produce Wigner-Ville Distribution (WVD) from the original R-R interval data series. Due to the intensive computation involved with this technique, a lot of effort has been directed towards an optimum design of Data Analysis Module.

The general data operation performed from R-R interval retrieval to WVD calculation is illustrated in the flowchart in Figure 3.3. The detailed WVD calculation is illustrated in Figure 3.4.

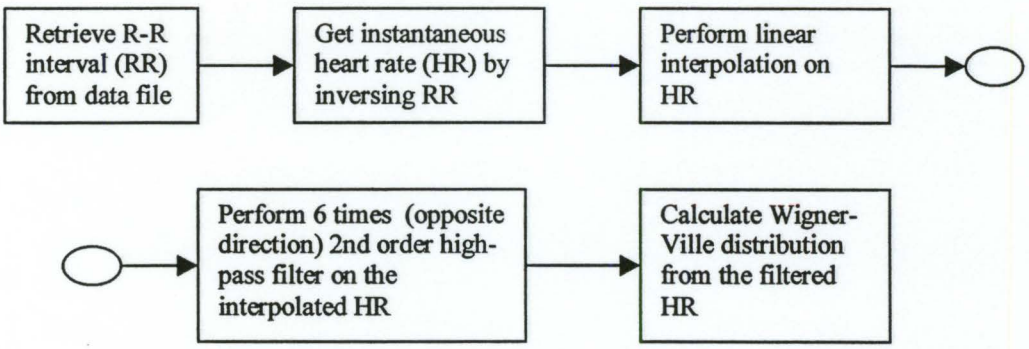

Figure 3.3 Block diagram of data operation from R-R retrieval to WVD calculation

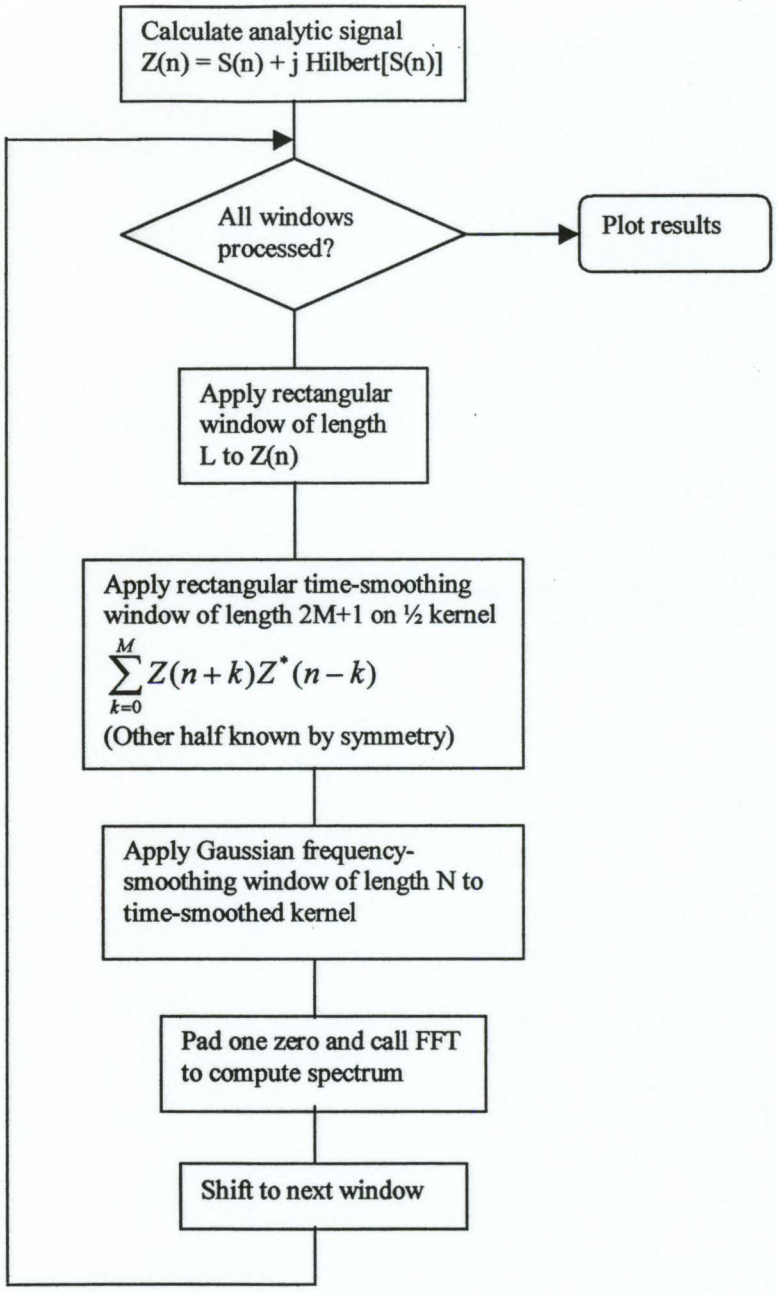

Figure 3.4 Flowchart of the algorithm implementing the WVD. (Mainly from Boashash, *Time-frequency signal analysis*, in Haykin S., Ed., *Advances in Spectrum Analysis and Array Processing*, vol. 1, Prentice Hall, pp. 459, 1991).

CWigner95Doc class holds the data and the functions that operate on the data. The description of the data and the functions are listed in Table 3.6 and 3.7. Since the computation demands several big arrays, care is taken to reuse the arrays as many times as possible. Because the original code was developed in MATLAB, the array index is chosen to start from one instead of zero (except W).

Table 3.6 Description of data in class CWigner95Doc

Data	**Description**
CWigner95Doc::irr_in_sec	Holds the 1x12000 R-R interval series in second
CWigner95Doc::hr	Holds the 1x12000 heart rate series in Hz Reused to hold the filtered interpolated heart rate series
CWigner95Doc::intp_hr	Holds the 1x12000 interpolated heart rate series in Hz
CWigner95Doc::W	Holds the 128x12000 Wigner-Ville Distribution array

Table 3.7 Description of functions in class CWigner95Doc

Function	**Description**
Intp_mrg()	Interpolate the heart rate series
Filter2()	High-pass filter the interpolated heart rate series
Hilbert2()	Perform Hilbert transform on filtered heart rate series
Wigner2()	Calculate Wigner-Ville distribution
Fft_comp2()	Perform FFT transform on complex data series
Ifft2()	Perform inverse FFT transform on complex data series
Fft_h2_2()	Perform FFT transform on real data series

A major challenge while estimating the Wigner-Ville Distribution was the computation of Hilbert transform. Based on our experience with programming using MATLAB, frequency domain method was chosen. A Visual C++ FFT transform and inverse FFT transform on complex data series was developed using algorithms available in literature (Kay, 1988). Relationships among these operations are illustrated in Figure 3.5. The arrow direction means 'builds on'.

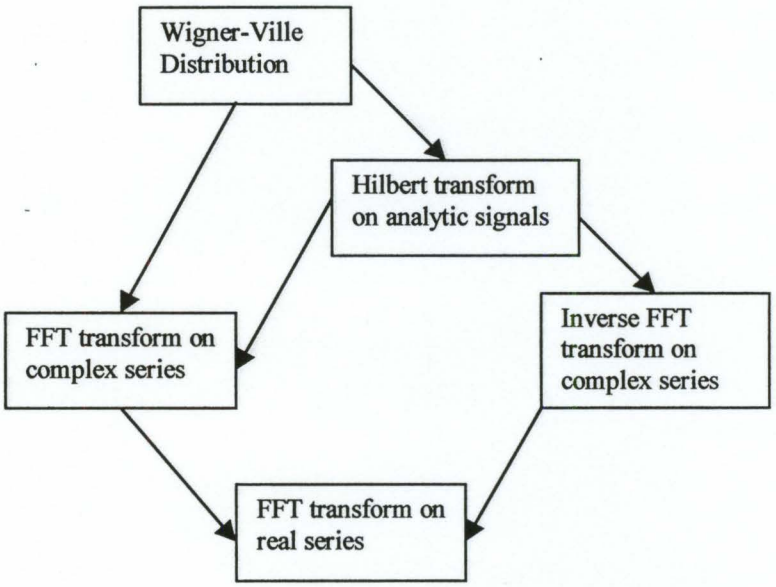

Figure 3.5 Relationships among signal processing operation modules

3.3.6 Design of Graphical Output Module

The critical part of a signal processing software is to show user a meaningful and intuitive graphical output. Efforts have been made to display an accurate, clear and comprehensive picture of what has been computed using **Wigner95**. Two classes involved and the related functions are listed in Table 3.8. In order to draw the contour figure we must extract the contour lines from a two-dimensional array. A public domain contour-plot function called conrec() was downloaded from the world wide web (http://www.mhri.edu.au/~pdb/, search "conrec") and linked with the in-house C++ code. This led to display similar to that obtained from MATLAB.

Table 3.8 Graphical display classes and functions

Class	Function	Description
CPlotRR_WVD	WriteHead()	Write the patient information as the header
	DrawRRvsTime()	Draw R-R interval versus time
	ContourWVD()	Draw contour of Wigner-Ville Distribution
CPlotLfHfVw	WriteHead()	Write the patient information as the header
	DrawRRvsTime()	Draw R-R interval vs. time in second
	DrawPower_vs_Time()	Draw LF, HF power and LF:HF vs time

3.3.7 Demonstration of Graphical User Interface

The following figures are the major dialog boxes and output plots of **Wigner95** (Figure 3.6-3.11).

3.3.8 Software Testing

The testing of **Wigner95** was performed in two stages. First stage focused on testing the validity of Wigner-Ville distribution algorithms using the simulated signals generated by MATLAB. Second stage focused on testing the Visual C++ software package against an algorithm written in MATLAB.

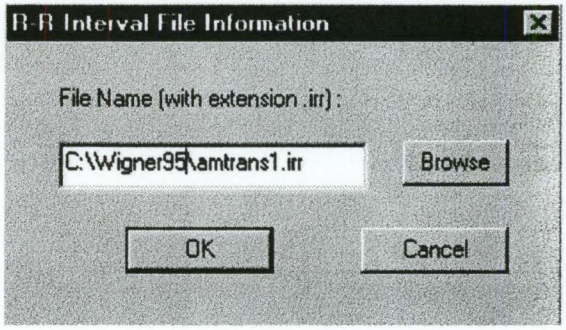

Figure 3.6 Dialog box for user to enter the name of the target data file

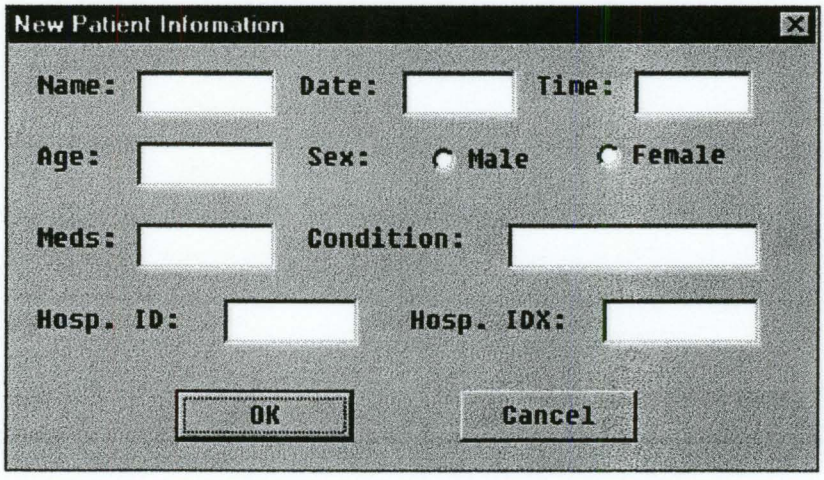

Figure 3.7 Dialog box for user to enter the new patient information

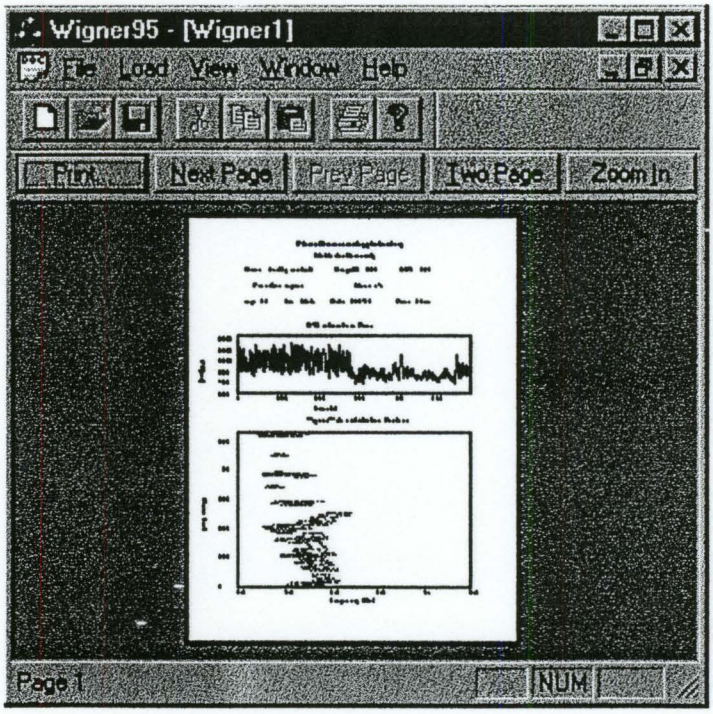

Figure 3.8 Wigner95 user interface for the information sheet of R-R interval and Wigner-Ville contour plot.

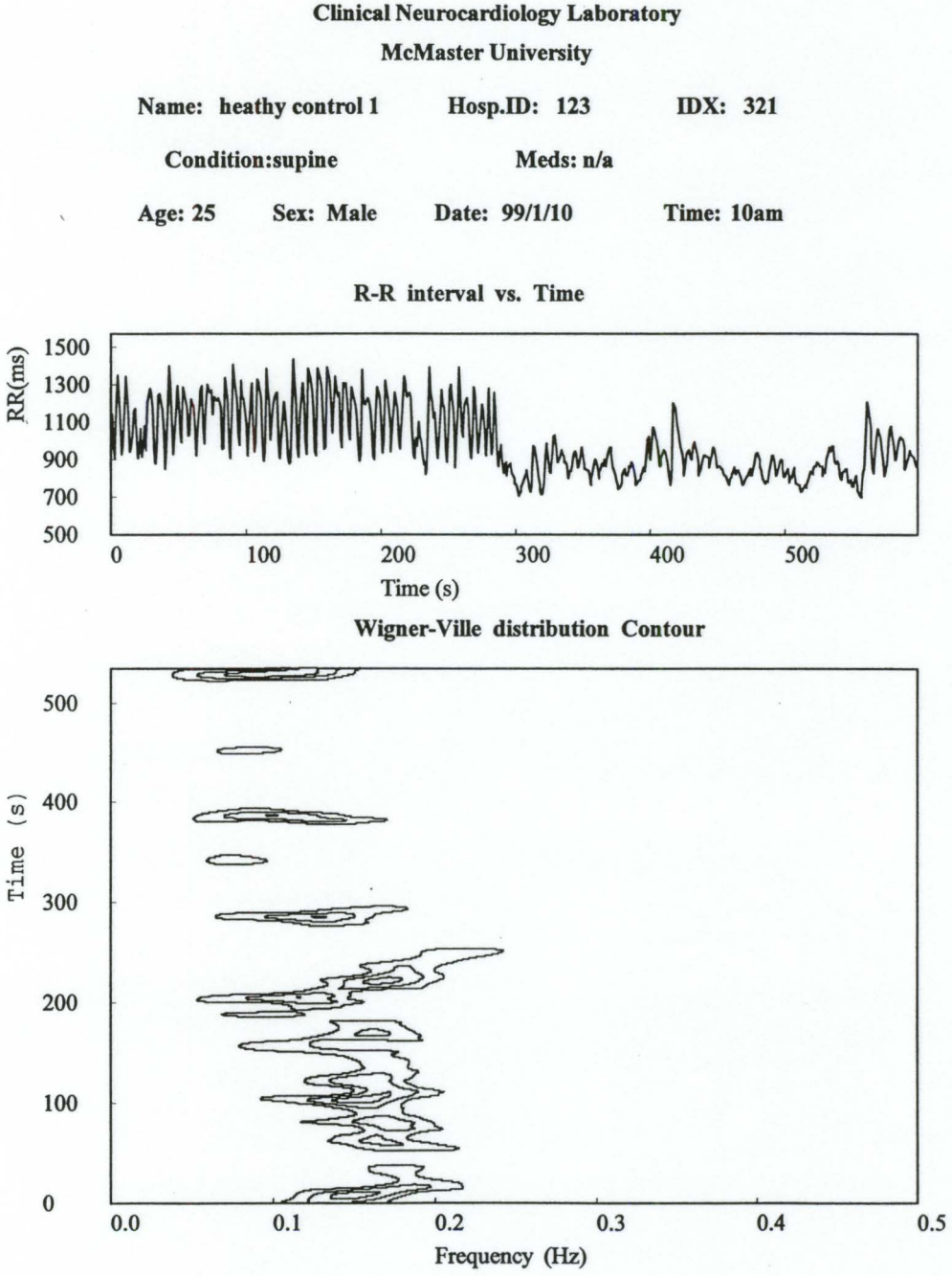

Figure 3.9 Wigner95 printout for the information sheet of R-R interval and Wigner-Ville contour plot.

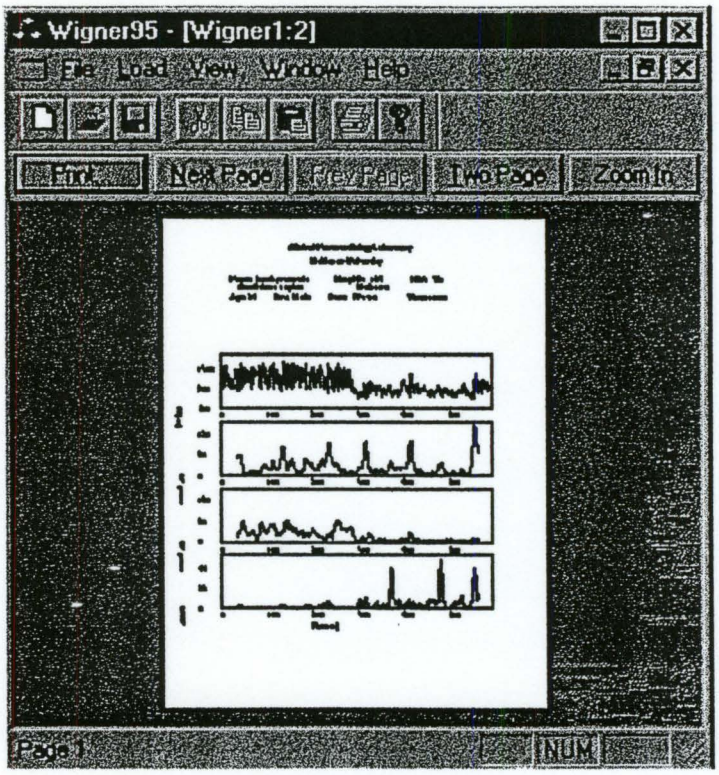

Figure 3.10 Wigner95 user interface for the information sheet of R-R interval and Low-Frequency (LF) power & High-Frequency (HF) power & LF:HF ratio.

Clinical Neurocardiology Laboratory

McMaster University

Name: heathy control 1 **Hosp.ID: 123** **IDX: 321**
Condition: supine **Meds: n/a**
Age: 25 **Sex: Male** **Date: 99/1/10** **Time: 10am**

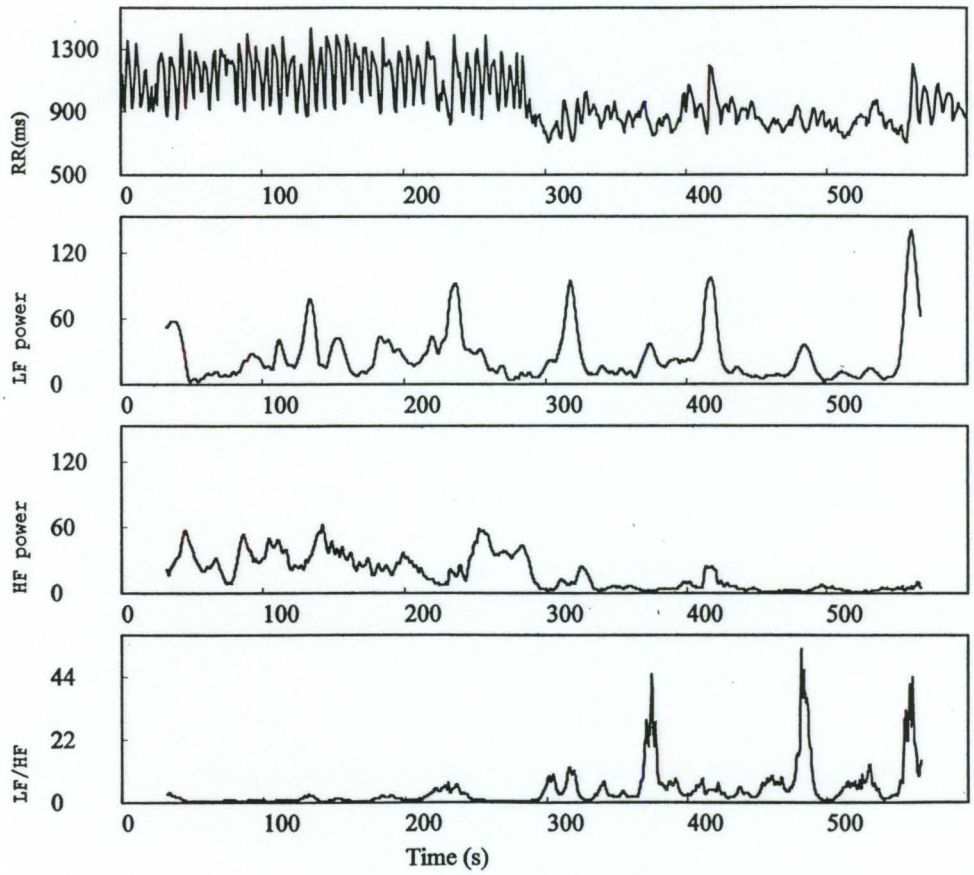

Figure 3.11 Wigner95 printout for the information sheet of R-R interval and Low-Frequency (LF) power & High-Frequency (HF) power & LF:HF ratio.

In Section 3.2.4, we briefly demonstrated the result of the WVD of a linear chirp with the parameters: $T = 500(s), f_o = 0(Hz), \alpha = 0.001$ (signal sample rate is 2Hz) (Figure 3.1). The result of the WVD can be tested in light of the parameters chosen in the implementation of the WVD, such as time smoothing window and frequency smoothing window. One can make the following observations:

a) The chirp signal is not detected in the WVD time-frequency (T-F) plane until around 32nd second. This is because in order to produce one power spectrum at time *n*, 32 seconds of data before and after the instance of time *n*, are needed. Hence the earliest detection will happen at 32nd second.

b) The chirp signal disappears in the WVD T-F plane at around 468th second although the signal continues until 500th second. Again, a 32 seconds of data after the current time instance *n*, is required. The latest detectable instant of time is 500-32 = 468 (s).

c) Finally, the most prominent contour line (or the highest peaks in 3-D display) of the WVD in the T-F plane faithfully reflects the instantaneous frequency of the chirp signal. For example, at t = 100 (s), using the Equation 3.10 we know the instantaneous frequency should be: 0+(0.001)(100) = 0.1(Hz), which appears in Figure 3.1 (b).

We generated another simulated signal *x(t)* to test the **Wigner95** (see Figure 3.12 (a)):

$$x(t) = \begin{cases} 0.5\sin(2\pi 0.1t) + \sin(2\pi 0.2t), & 0 \le t \le 500(s) \\ \sin(2\pi 0.1t) + 0.5\sin(2\pi 0.2t), & 500 \le t \le 1000(s) \end{cases} \qquad (3.22)$$

The signal contains two frequency components, i.e. 0.1 Hz and 0.2 Hz. The dynamics is reflected in the amplitude of these two components. During the first 500 seconds,

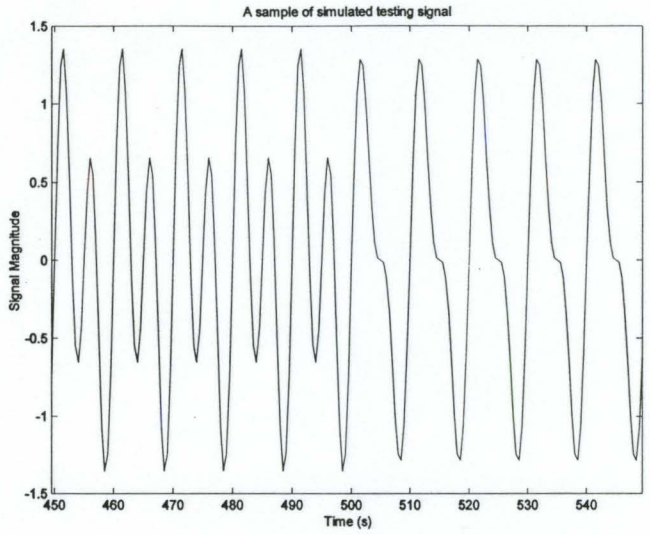

(a)

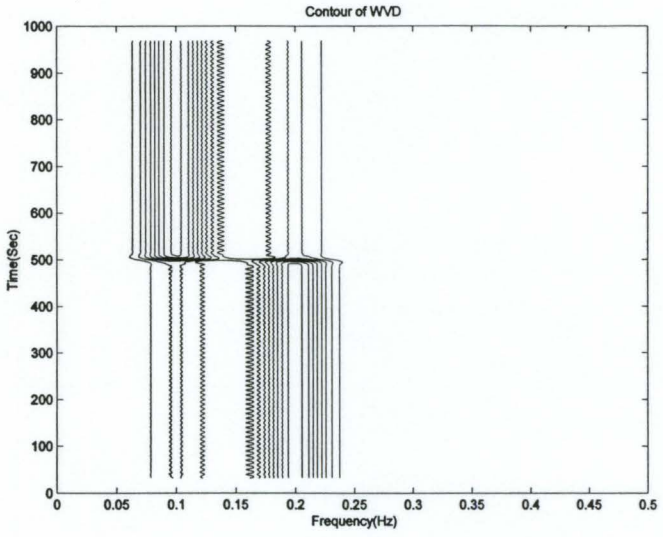

(b)

Figure 3.12 1000-second long simulated testing signal with two frequency components (0.1 Hz & 0.2 Hz), the amplitudes of these two components change abruptly at 500th second. (a) A 100-second long sample display centered at 500th second. (b) 2-D contour plot of Wigner-Ville distribution. (c) 3-D plot of Wigner-Ville distribution.

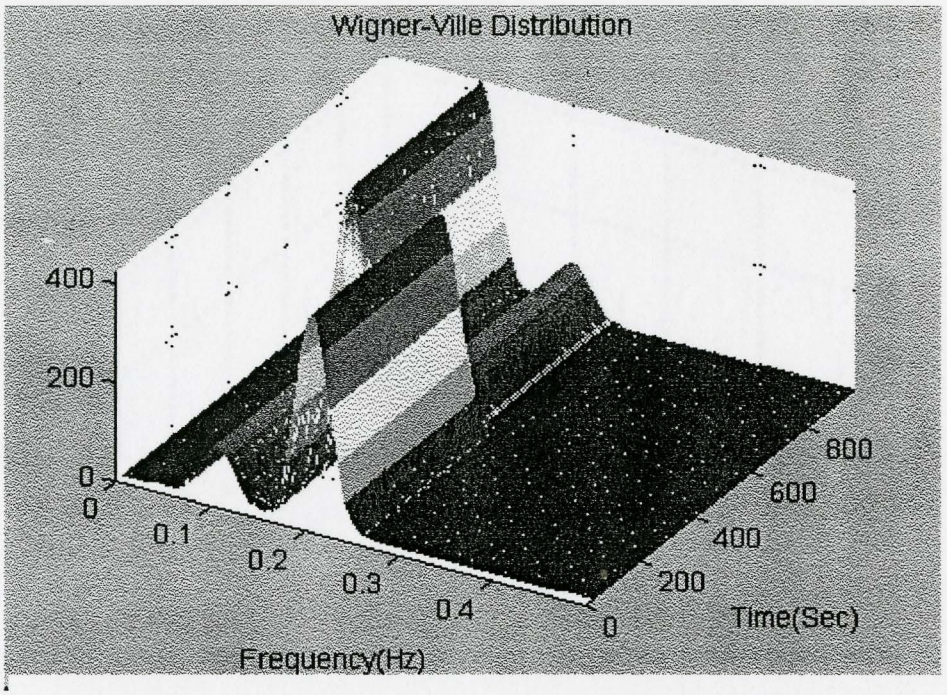

(c)

Figure 3.12 (*contd.*)

component at 0.2 Hz has amplitude that is twice as high as at 0.1 Hz. And during the next 500 seconds, the situation is opposite to the first 500 seconds. This signal design simulates the dynamic changes that take place in the heart rate signal during a passive tilt from 0° to 90°. The 2-D and 3-D results of the WVD for Equation 3.22 are illustrated in Figure 3.12 (b)-(c). One can see that **Wigner95** is able to accurately locate the two frequency components 0.1 Hz and 0.2 Hz and capture the amplitude change. In addition, the WVD demonstrates a good time resolution at the time instant of abrupt change of the frequency content.

The two-dimensional Wigner-Ville distribution array computed through **Wigner95** was compared with results obtained through MATLAB software. These results agree with each other, up to 5 decimal places.

3.4 Wigner-Ville Distribution of the Heart Rate Variability Signal

A ten-minute segment of the R-R interval signal (Figure 3.13 (a)) recorded during a 'supine-tilt operation-90° tilt' experiment was used for evaluation of the **Wigner95**. The recording was started 5 minutes before the tilt operation. At the 5th minute, the tilt operation from 0° to 90° was carried out in about 15 seconds. The recording was stopped at about the tenth minute. The signal was then analyzed using **Wigner95** software to demonstrate the application of the WVD in real life setting (Figure 3.13 (b)-(d)). In addition, the signal was processed using conventional power spectral analysis methods i.e., AR and BT algorithms (Figure 3.13 (e)-(f)).

We can make following observations from these results:

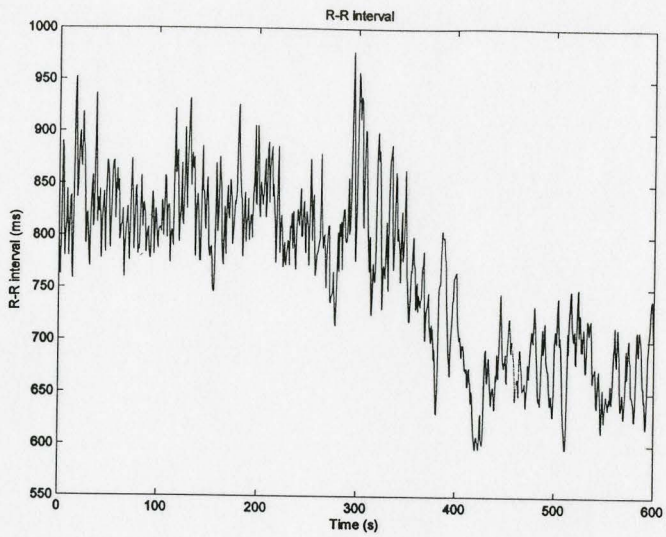

(a)

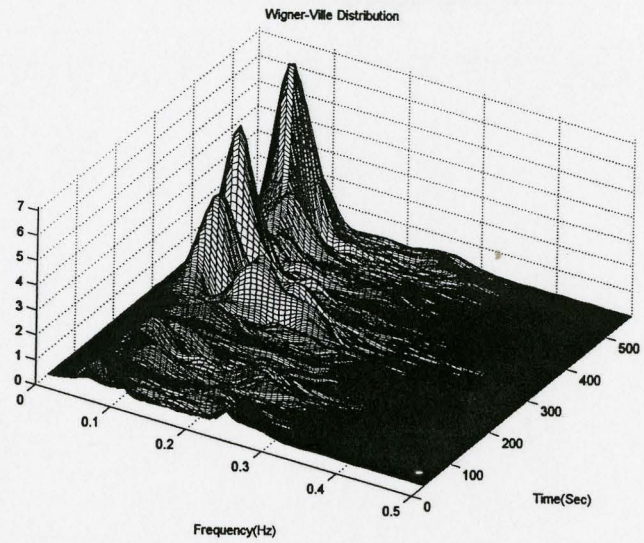

(b)

Figure 3.13 A sample of ten-minute long R-R interval signal and results from three different signal processing techniques: (a) R-R interval signal. (b) 3-D plot of Wigner-Ville distribution. (c) 2-D contour plot of Wigner-Ville distribution. (d) LF, HF, LF:HF ratio along with R-R interval signal. (e) Four AR power spectra. (f) Four BT power spectra.

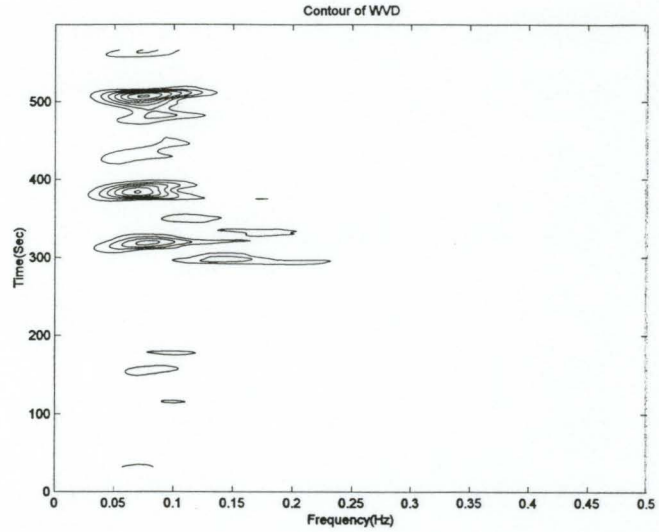

(c)

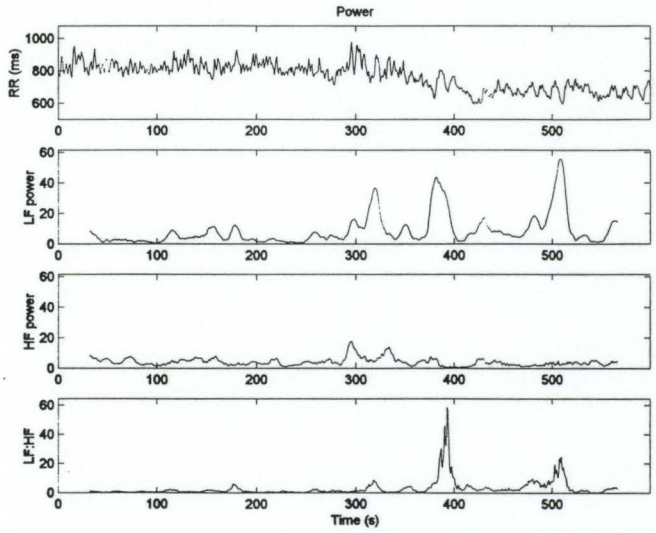

(d)

Figure 3.13 (*contd.*)

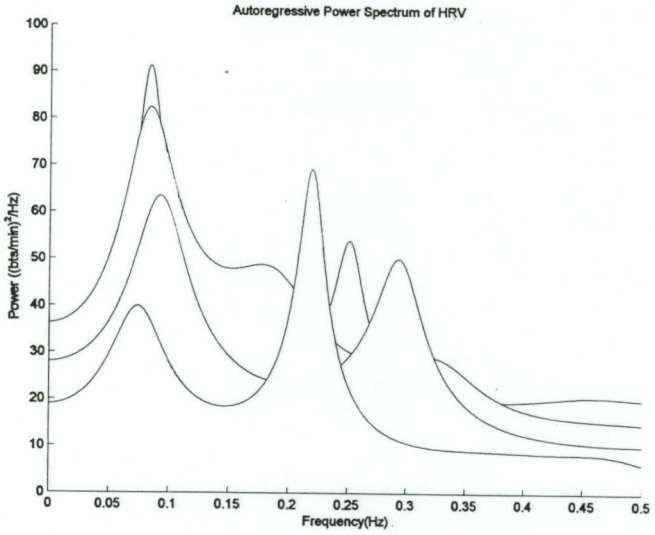

(e)

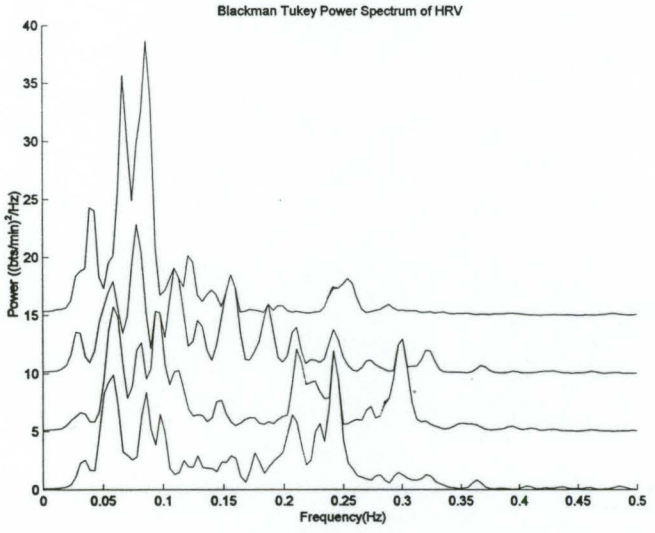

(f)

Figure 3.13 (*contd.*)

a) All three methods are able to demonstrate, through changes in the LF power, HF power and LF:HF ratio, the difference between supine position and 90° tilt (Table 3.9-3.11). For example, from the statistics generated by the AR method, the LF:HF ratio increased from 0.66 (first 128 sec data) to 1.32 (last 128 sec data) for a change from supine to 90° tilt. For the BT method, the LF:HF ratio increased from 0.91 (first 128 sec data) to 6.01 (last 128 sec data) for a similar change in the position of the body. And the WVD algorithm showed an increase from 0.59 (first 128 sec data) to 3.39 (last 128 sec data).

b) Conventional power spectral computation and the WVD technique show a large difference in their ability to capture the dynamics that occurred at the 5th minute (Figure 3.13 (a)). Both AR & BT methods only provide four power spectra (one for every 128-second data segment) while WVD is able to produce 1072 power spectra (2×600-128 = 1072) through the 10 minute data. Hence subtle details of the changes in power spectra are revealed.

In order to fully make use of the information in the 3-D plot of WVD, we generated a display of the LF power, HF power and LF:HF ratio versus the same 10-minute time index along with R-R interval (Figure 3.13 (d)). By examining this figure, we can identify a significant increase in LF power at the 300th second even though the R-R interval decreased only at the 360th second. Using WVD technique to investigate the nonstationary signals originating in the autonomic nervous system is a topic we want to explore in greater depth in the future.

Table 3.9 Statistics of AR power spectra of ~10 min HRV signal

	LF power	**HF power**	**LF:HF ratio**
0-128 second	4042.81	6168.13	0.66
128-256 second	5643.45	6286.57	0.9
256-384 second	7008.37	6347.9	1.1
384-512 second	5091.67	3844.17	1.32

Table 3.10 Statistics of BT power spectra of ~10 min HRV signal

	LF power	**HF power**	**LF:HF ratio**
0-128 second	120.12	132.5	0.91
128-256 second	138.77	111.98	1.24
256-384 second	154.3	98.37	1.57
384-512 second	217.61	36.23	6.01

Table 3.11 Statistics of averaged WVD of ~10 min HRV signal in every 128 sec

	LF power	**HF power**	**LF:HF ratio**
0-128 second	2.62	4.7	0.59
128-256 second	4.02	3.47	1.37
256-384 second	13.85	7.99	2.32
384-512 second	9.33	3.21	3.39

Chapter 4

Ontologic Assessment of the Autonomic Nervous System in Preterm and Full term Infants through Power Spectral Analysis

4.1 INTRODUCTION

The delivery and subsequent management of very low birth weight (VLBW) premature infants in the neonatal intensive care unit (NICU) provides a unique opportunity to study the ontogeny of the ANS. To date, development and maturation of the ANS in infants of 24 to 28 weeks gestational age (GA) has not been adequately studied. Previous studies in premature infants and in animal models imply a sympathetic predominance in the developing fetus until birth, at which point parasympathetic outflow becomes evident (Clairambault et al., 1992; Pomeranz et al., 1985; Malliani et al., 1991). Recently, in a cross-sectional study of 35 neonates, Chatow et al. (1995) found that sympathetic modulation of HR was the predominant component of the HRV signal with increasing gestational and post-natal age.

The objective of the present study was to employ the non-invasive methodologies

developed in this research on PS/HRV to study longitudinally the post-natal development and maturation of the ANS in VLBW premature infants of 24-28 weeks gestational age. The study reported in this chapter was conducted in collaboration with Dr. Kevin Jacobson from the Department of Pediatrics at McMaster University Medical Center. I developed and tested the algorithms of power spectral analysis of premature infant ECG signal. In addition, I helped him to analyze the data and interpret the results.

4.2 METHODS

4.2.1 Patient Population

Fourteen consecutive premature infants of GA 24-28 weeks admitted to the NICU and 41 full term healthy infants of GA 38-41 weeks were recruited at McMaster University Medical Center between June 1997 and December 1997. Ethics approval was obtained from the McMaster University Medical Center Hospital Ethics Advisory committee prior to commencement of the study. Written informed consent was obtained from parents prior to the inclusion of any infant into the study.

Medications and health status of all subjects including the mothers were documented. All recruited preterm infants had a birth weight of <1200 g (mean 873±223g). On each infant, continuous ECG and respiratory data were recorded between 10 AM and 4 PM for 20 minutes during quiet or active sleep (determined qualitatively by observation of head and limb movements). Lead II ECG was recorded from monitors (PC Express 90308, Space Labs Medical, Redmond, WA, USA), and sampled at 500 Hz. Recordings were obtained weekly during the first four weeks of life (initial recording at 2.6±0.9 days), biweekly for the next four weeks, and then monthly until discharge. Three recordings were obtained from infants who were less than 26 weeks GA, but were

omitted from further analysis due to poor quality of the data and insufficient sample size of the population. An average of 6 recordings was obtained for each infant between birth and discharge. Age was expressed as conceptional age (CA = gestational age (GA) + post- natal age (PA)). In addition blood pressure data were recorded, twice daily from the arterial line in those infants who had an arterial line and then via cuff occlusion at 4 AM and 4 PM.

We also recorded heart rate and respiratory data for comparison from 41 full term infants delivered either vaginally or by cesarean section, and admitted to the nursery at the McMaster University Medical Center for observation. These full term infants (n=41, Table 4.1), gestational age 38-41 weeks (39.9±1.3 weeks) had no abnormalities or complications on delivery. Following informed parental consent, a single recording for each infant was obtained 8-36 hours after birth. Three ECG electrodes were attached to the chest, and real-time, 20-minute recordings of HR and respiratory data were sampled at 500 Hz by a NARCO Scientific monitor (model HRRM71-1) and stored on a personal computer.

4.3 DATA ANALYSIS

4.3.1 Signal Acquisition and Power Spectral Analysis of Heart Rate Variability

The neonatal ECG and respiration signals were digitized using a 12 bit analog-to-digital converter (AT/CODAS, DATAQ Instruments, Inc., Akron, Ohio 44333, USA) at 500 Hz and processed on a Personal Computer. A QRS detection algorithm was implemented in the software to locate a stable and noise independent fiducial point on the R-wave (Ruha et al., 1997). An RR-interval series was then generated from the continuous ECG data. Occasional ectopic beats were corrected using ectopic correction

Patient	Sex	Mode of Delivery	Gestational Age (wks)	Birth Weight (g)
P1	m	vag	27	1059
P2	m	vag	27	1030
P3	m	vag	26	878
P4	f	c/s	26	680
P5	f	c/s	26	609
P6	m	c/s	27 (?)	1325
P7	f	vag	25	743
P8	m	c/s	28	930
P9	f	vag	25	759
P10	f	c/s	27	533
P11	f	vag	26	968
P12	m	vag	26	1162
P13	m	vag	27	684
P14	m	vag	26	860
MEAN	m:f= 8:6	n/a	26.4 ± 0.8	872.9 ± 223.2
Full Term (n=41)	m:f= 24:17	n/a	**39.9±1.3**	3556.9± 533.4

Table 4.1 Subject demographics.

algorithms (Kamath and Fallen, 1995). A beat-to-beat heart rate variability signal was computed and then re-sampled at 6 Hz using linear interpolation to obtain an equally sampled time series. A record length of 768 points from the re-sampled signal (128 seconds) was selected for power spectral analysis. Since the mean value of the signal contributes only to the direct current (DC) value of the PS/HRV, the mean value of the signal was removed and the equally sampled HRV signals were fed through a fourth order high-pass Butterworth filter with a cut-off of 0.015 Hz (Oppenheim and Schafer, 1975). A Blackman-Tukey power spectral algorithm was then applied to the zero mean, filtered heart rate variability data (Kay and Marple, 1981). The power spectrum was divided into two bands: low frequency (LF, 0.02-0.2 Hz) and high frequency (HF, 0.2-1.0 Hz). The area subtended by each spectral band was then computed by numerically integrating the power contained therein. This was expressed in absolute units $(\text{beats/min})^2/\text{Hz}$. The LF:HF ratio was then computed as the ratio of these areas and used as a measure of sympathovagal balance (Akselrod et al., 1981; Kamath and Fallen, 1993; Kamath and Fallen, 1995; Pagani et al., 1986; Hirsch and Bishop, 1981).

4.3.2 Respiratory Signal Analysis

A frequency analysis of the respiratory signal was performed using Blackman-Tukey algorithm (Kay and Marple, 1981), for each recording session.

4.3.3 Sleep State Assessment

In full term and preterm subjects, quantitative analysis of sleep state was performed, using modified Prechtl guidelines (Prechtl, 1974). Patients were observed and

categorized according to the following criteria; eyes open or closed; duration and magnitude of startles, head, arm and leg movements; presence or absence of vocalizations. Using this information, sleep states were assigned as: a) quiet sleep (QS); b) active sleep (AS).

4.3.4 Statistical Analysis

The HRV indices derived from power spectral analysis of HRV were analyzed by a two-way analysis of variance (ANOVA) on each individual preterm infant, and then collectively according to CA. Regression analysis was performed to compare respiratory frequencies to HRV parameters, as classified by sleep state, gender and mode of delivery. A multivariate analysis of variance (MANOVA) was also performed, using CA as the grouping factor, and LF:HF area and blood pressure (AM and PM considered separately) as the dependent variables. Results with a p value <0.05 were considered statistically significant. Results are expressed as group mean values ± SEM, unless otherwise stated. Statistical analysis was carried out using SPSS/PC+ statistical package software for Windows (Version 6.1, SPSS Inc., Chicago, IL, USA).

4.4 RESULTS

From the 15 preterm infants with 84 recording sessions, 14 infants with 72 recording sessions were analyzed for this study. Recordings from one infant were excluded from analysis due to poor quality ECG signals. The population was grouped according to CA: group A (n=13, 26-28 weeks), group B (n=13, 28-30 weeks), group C (n=9, 30-32 weeks), group D (n=8, 32-34 weeks), group E (n=6, 34-36 weeks), group F

(n=5, 36-38 weeks). As the population size decreased significantly over time, subgroup analysis was performed on 5 preterm infants in whom recordings were obtained for the full duration of the study from 26 to 38 weeks CA (Figure 4.2). The analysis of the smaller group revealed similar changes in PS/HRV parameters as compared to the entire group of preterm infants (n=14). The full term infant data (n=41), (Table 4.1) was analyzed as a single group (group G), and was used as a comparative control to groups A to F. However, Group G was not used in the statistical analysis of preterm infants.

Figure 4.1 shows a sample power spectrum of HRV from a preterm infant recorded during six periods of the study. No significant change was observed in the mean resting heart rate (HR) of the study group for the duration of the study. As shown in Figure 4.2, analysis of the heart rate spectra in all preterm infants revealed that the LF:HF area increased initially from 26 to 30 weeks CA, peaked at 30-32 weeks and decreased during subsequent recordings. Two-way analysis of variance using conceptional age groups A to F, revealed an increase in the LF:HF area to a maximal level at 30-32 weeks CA ($p=0.053$).

In preterm infants with increasing CA, no noticeable differences were observed in the HR during AS or during QS. The LF:HF area increased progressively with CA in preterm infants during AS, however, there were no appreciable changes over time in the LF:HF ratio during QS (Figure 4.3). This finding suggests an increase in responsiveness of the ANS with increasing CA, which is likely due to sympathetic nervous system activation. In full term infants, the LF:HF area was found to be higher during AS than during QS. In these infants, the respiratory frequency had a negative correlation of 0.46 with LF:HF area (Figure 4.4), whereas in preterm infants, no significant correlation

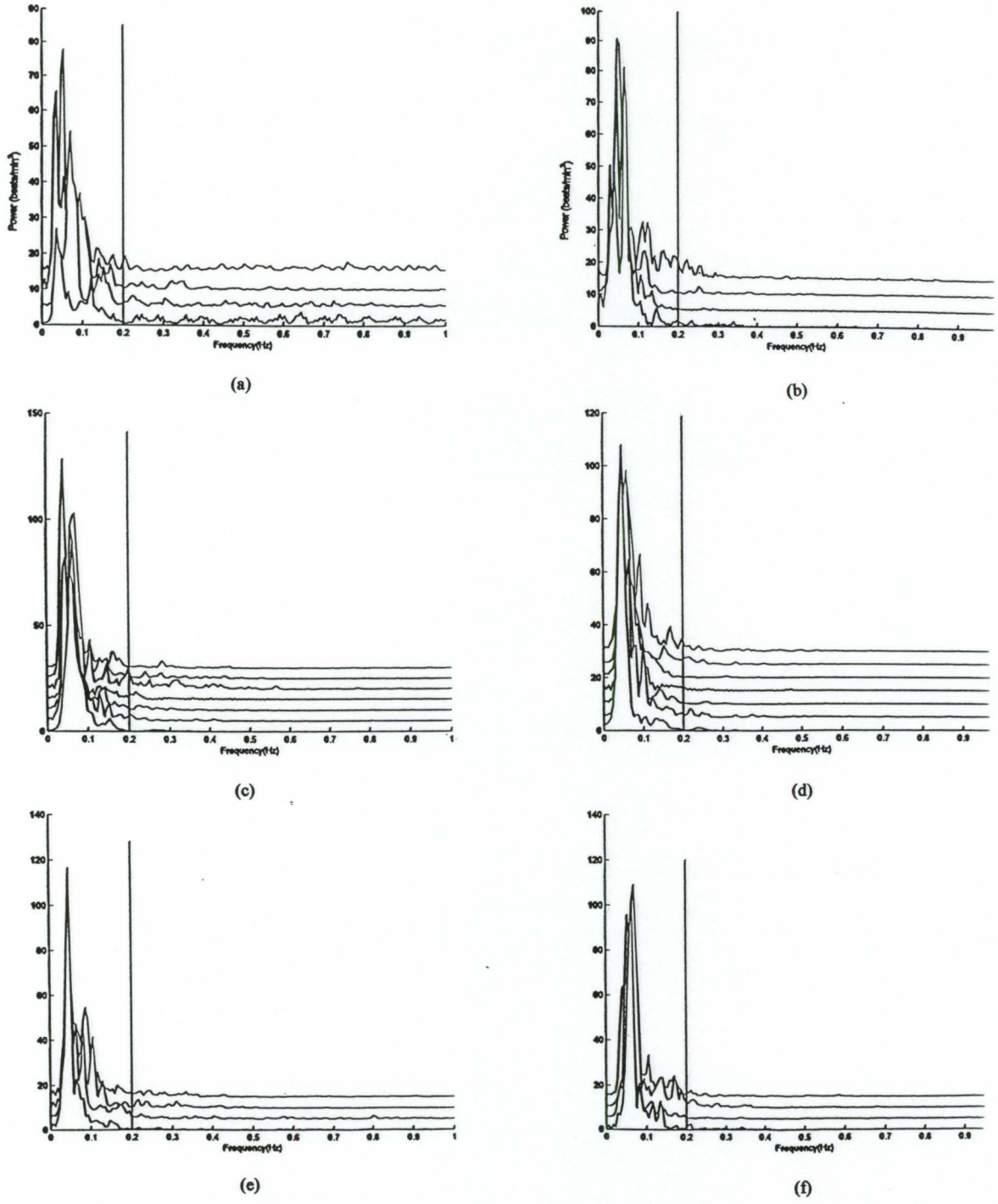

Figure 4.1 Multiple HRV/PS data of a premature infant (P1). HRV/PS as seen by Power ((beats/min)^2) versus Frequency (Hz). A vertical line at 0.2 Hz shows the separation of low frequency (LF) and high frequency (HF) powers. Each panel represents the power spectra of 20 minutes of HRV data, and segments of data which contained artifacts were discarded. The infant was recorded at: (a) 26-28 weeks GA, (b) 28-30 weeks GA, (c) 30-32 weeks GA, (d) 32-34 weeks GA, (e) 34-36 weeks GA, (f) 36-38 weeks GA.

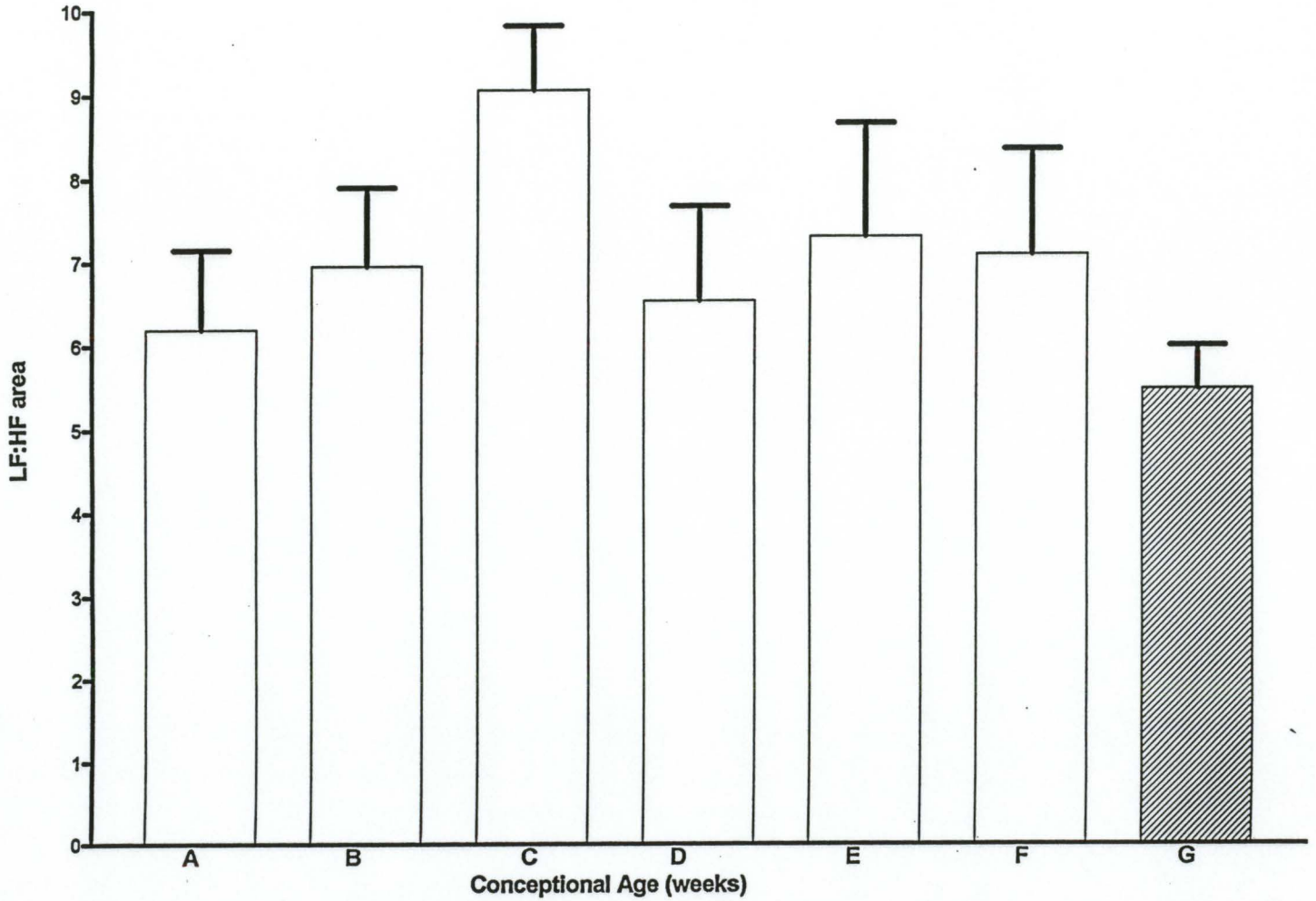

Figure 4.2 Infant LF:HF area versus conceptional age. Group A (24-28 weeks, n=13); group B (28-30 weeks, n=13); group C (30-32 weeks, n=9); group D (32-34 weeks, n=8); group E (34-36 weeks, n=6); group F (36-38 weeks, n=5); group G (38-41 weeks, n=41).

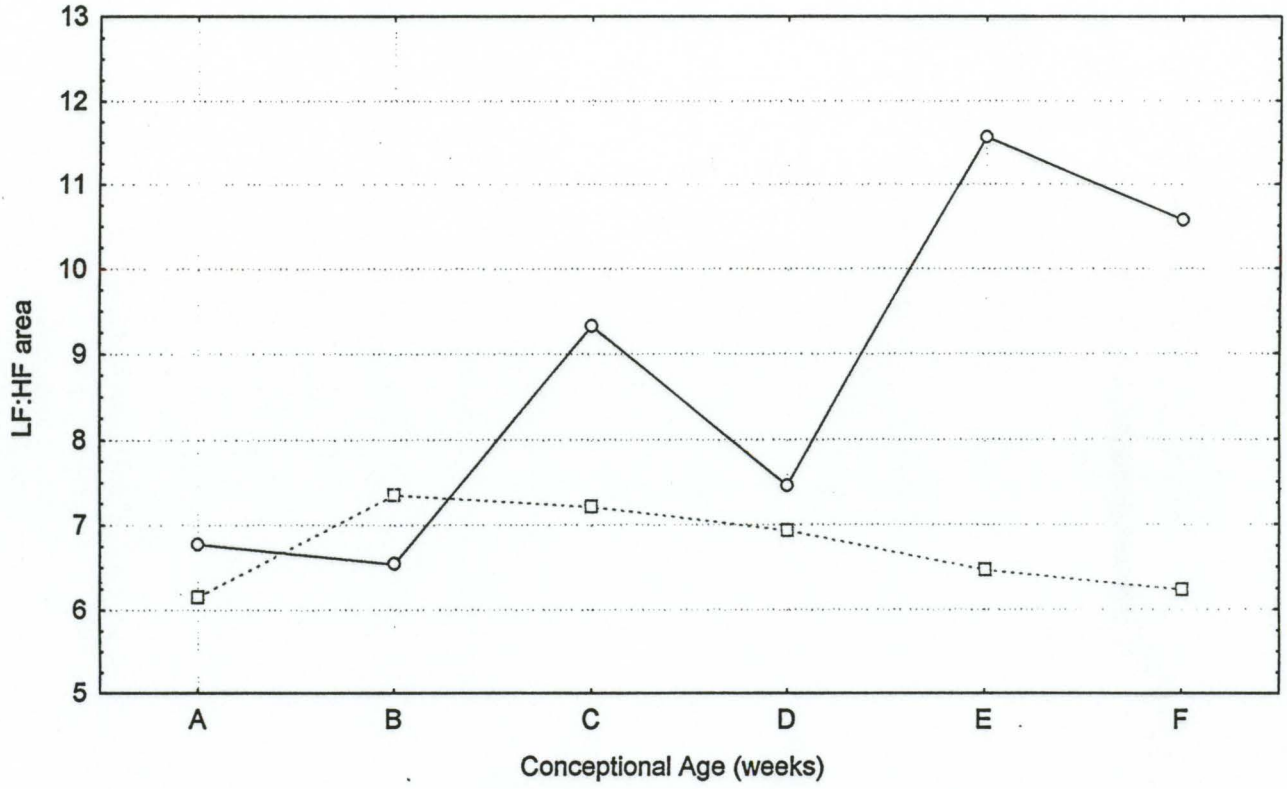

Figure 4.3 Comparison of sleep states in preterm infants. Active sleep (circle); quiet sleep (square). Group A (24-28 weeks, n=13); group B (28-30 weeks, n=13); group C (30-32 weeks, n=9); group D (32-34 weeks, n=8); group E (34-36 weeks, n=6); group F (36-38 weeks, n=5).

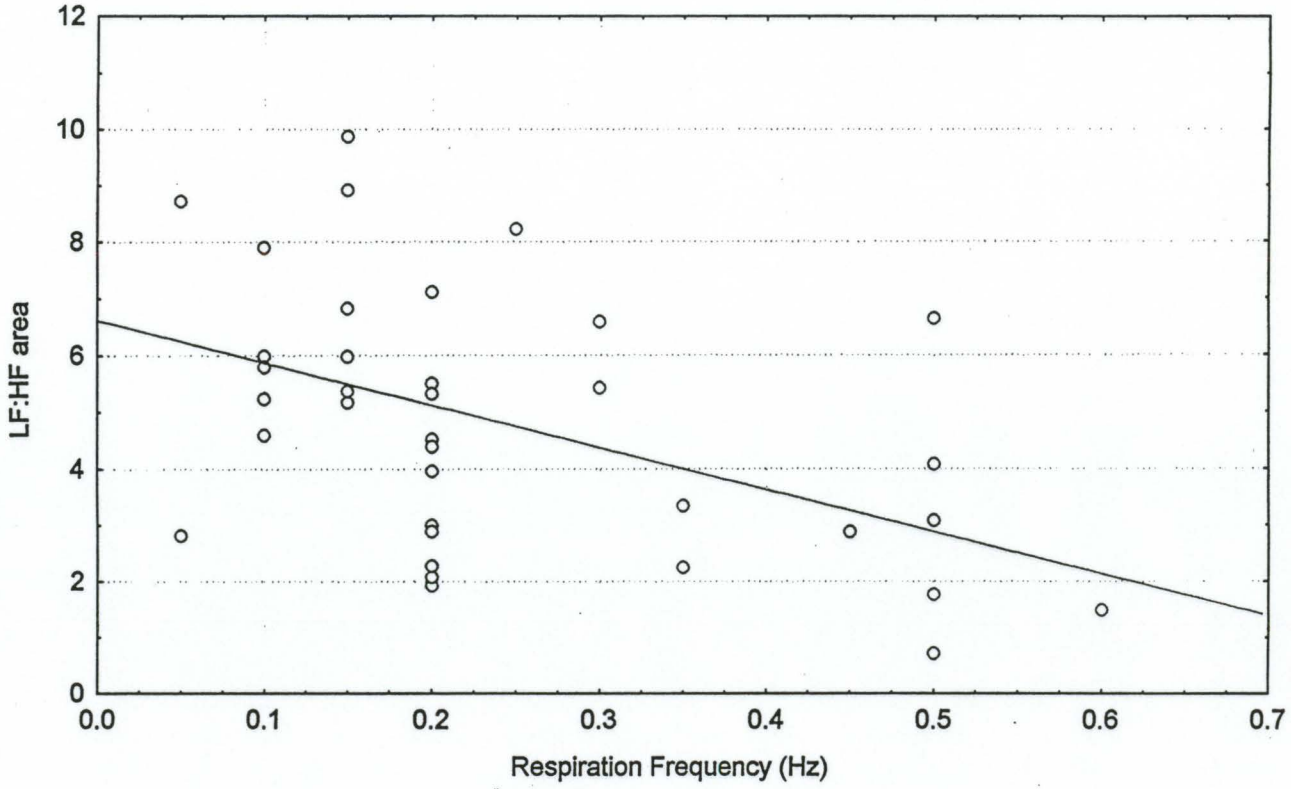

Figure 4.4 Scatterplot of full-term infant LF:HF area versus respiration frequency (Hz). Full-term infants (38-41 weeks GA, n=41) recorded at 8-36 hours after birth. Statistical analysis: r = -0.46 (removal of three outliers).

(0.13) was observed (Figure 4.5).

A plot of systolic (SBP) and diastolic blood pressure (DBP) with CA showed a bimodal distribution resembling that observed with LF:HF ratio, which was confirmed by MANOVA, (Figure 4.6) with CA as the grouping factor, and LF:HF area and blood pressure (AM and PM considered separately) as the dependent variables ($p<0.05$).

4.5 PHYSIOLOGICAL RELEVANCE

This longitudinal study in the preterm infant population was designed to evaluate non-invasively the ontogeny of the ANS using power spectral analysis of heart rate variability. Our results suggest a sympathetic predominance in early post-natal life with a peak in sympathetic outflow at 30-32 weeks followed by an increase in vagal outflow and an increase in ANS responsiveness with increasing post-natal age.

A limitation of the study is the high drop out rate of infants due to early transfer of healthier babies to outlying health care centers. Therefore, a subgroup analysis was performed on the 5 preterm infants in whom recordings were obtained for the full duration of the study from 26 to 38 weeks CA (10.0 ± 1.1 weeks). Analysis of the HRV parameters from this group ($n=5$) was in agreement with the HRV indices of the larger group ($n=14$) (Figure 4.7).

Assali et al (1978) have previously demonstrated sympathetic predominance in resting HR in lambs prior to term delivery, which was followed by a post-natal increase in parasympathetic modulation. In a cross-sectional study of preterm infants, Clairambault et al. (1992) have observed a gradual increase in LF power from 31 weeks to 41 weeks CA, and a rapid increase in HF power at 36-38 weeks CA. Our observation

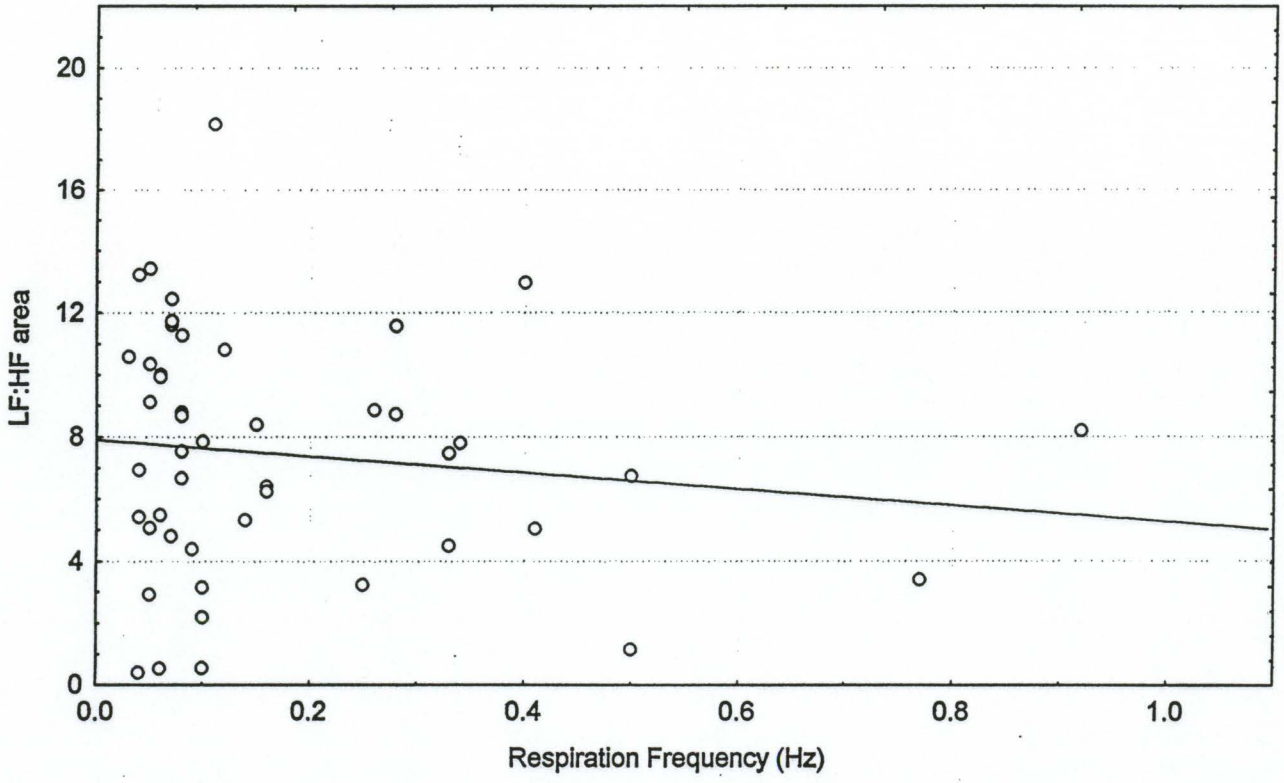

Figure 4.5 Scatterplot of preterm infant LF:HF area versus respiration frequency (Hz). Preterm infants (24-28 weeks GA, n=14) examination of changes in respiratory frequency and LF:HF area over duration of study. Statistical analysis: r = -0.13.

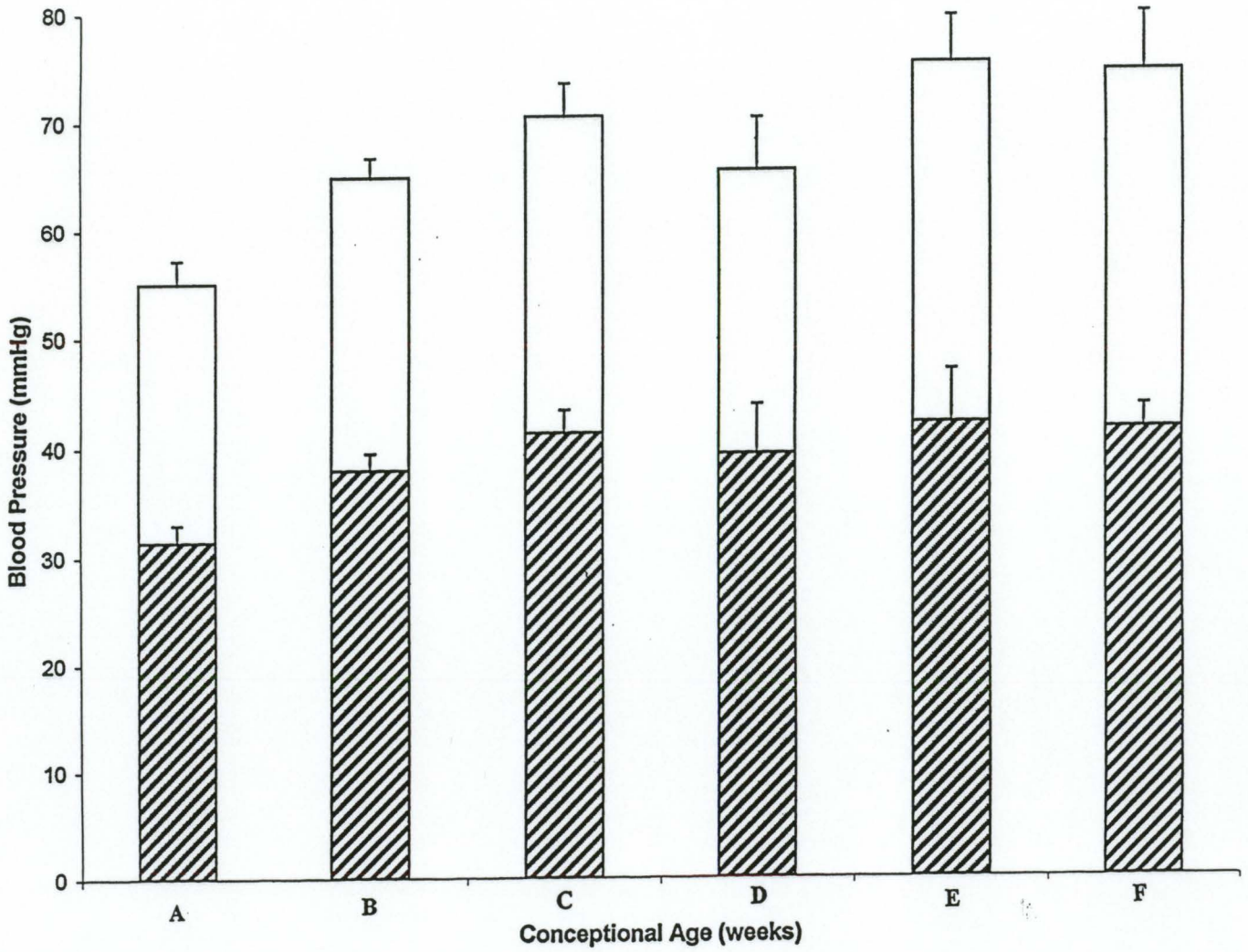

Figure 4.6 Preterm infants blood pressure versus conceptional age (bar with no pattern: systolic BP; bar with diagonal line: diastolic BP). Group A (24-28 weeks, n=13); group B (28-30 weeks, n=13); group C (30-32 weeks, n=9); group D (32-34 weeks, n=8); group E (34-36 weeks, n=6); group F (36-38 weeks, n=5).

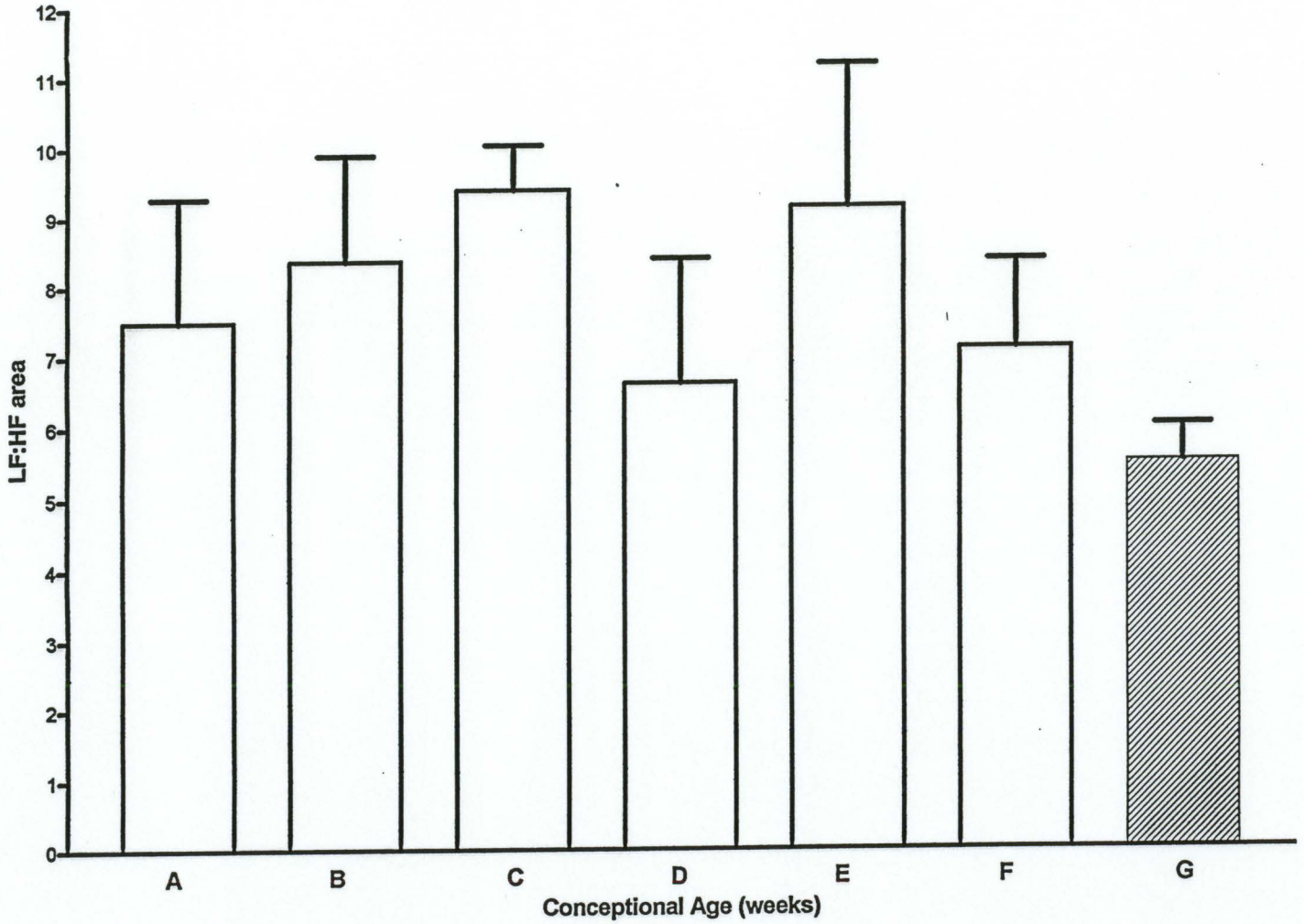

Figure 4.7 Infant LF:HF versus conceptional age. Group A (24-28 weeks, n=5); group B (28-30 weeks, n=5); group C (30-32 weeks, n=4); group D (32-34 weeks, n=5); group E (34-36 weeks, n=3); group F (36-38 weeks, n=5); group G (38-41 weeks, n=41).

of increased LF:HF area for CA of 26-34 weeks can thus be interpreted as evidence of increasing sympathetic modulation of the sinus node. Furthermore, the subsequent decrease in LF:HF area with increasing CA in our study represents an increasing vagal modulation and maturation of the parasympathetic nervous system. These observations are in agreement with Clairambault et al. (1992). In addition, a diminished LF:HF ratio in full term infants lends support to the belief that the development reached at term reflects a later stage in ANS maturation *in-utero*. The LF:HF area ratio in the preterm population at 36-38 weeks CA was not significantly different from that observed in full term infants (7.10±1.27 at 36-38 weeks vs 5.49±0.51 at 38-41 weeks GA, NS), suggesting that the *ex-utero* maturation of the ANS in preterm infants reaches a similar end point.

Using sleep state as an independent variable (active or quiet sleep), the responsiveness of the ANS can be observed through the changing LF:HF area. Our findings among preterm infants, although not statistically significant, suggest that during active sleep, LF power increases progressively with increasing CA. This lends support to the hypothesis that a decline in LF:HF area seen after 30-32 weeks CA is not due to a decline in sympathetic modulation, but rather due to an increase in the vagal outflow. Van Ravenswaaij-Arts et al. (Clairambault et al., 1992; Van Ravenswaaij-Arts et al., 1991; Eiselt et al., 1993; Van Ravenswaaij-Arts et al., 1994), also noted an increase in LF in infants during AS. Other investigators have confirmed these observations (Clairambault et al., 1992; Eiselt et al., 1993; Harper et al., 1987).

Due to frequent mechanical ventilation in the very low birth weight population, the influences of respiration was difficult to ascertain. A majority of infants studied required ventilator assistance at birth and for up to two months post delivery. There was

poor correlation between respiratory frequency and LF:HF ratio in both preterm and full term infants (Figure 4.4 & 4.5).

Similarities in progression of LF:HF ratio and blood pressure with CA suggest maturational mechanisms of both ANS and hemodynamic systems are working concomitantly. The commonly observed spike in blood pressure in very low birth weight infants a few weeks after birth has previously been an unexplained phenomenon (Georgief et al., 1996; Greenough and Emerey, 1993; Alpert, 1995). Previous studies have attempted to correlate clinical interventions with the rise in blood pressure (Georgief et al., 1996; Greenough and Emerey, 1993). Studies using intravenous morphine infusions have failed to demonstrate any significant effect on mean arterial blood pressure (Sabatino, et al., 1997), whereas, in a small, uncontrolled trial of ventilated preterm infants requiring post-natal steroids, blood pressure has been seen to increase (Cabanas et al., 1997). In a prospective study of infants in 14 regional NICU's, blood pressure was found to correlate significantly with post-conceptional age. However, treatment variables were found to have had some small influence (Zubrow et al., 1995). While the influence of medications such as corticosteroids and inotropic agents cannot be ruled out, it is more likely that these observations are due to maturation of the ANS and represent central ontological mechanisms modifying sympathetic and parasympathetic outflow of the ANS.

Chapter 5

Heart Rate Variability in Small Animal Models

5.1 INTRODUCTION

In many studies involving human subjects, it is not possible to test the effects of stress and a number of pharmacological agents. In such studies, rat models have been useful. Development of algorithms suitable for studying PS/HRV of small animal models was a challenge that has interested our group. In this chapter we describe development and application of algorithms for evaluating heart rate variability (HRV) and its power spectra (PS) during experimental investigations on a rat model.

The autonomic nervous system contributes to the control of respiratory function. The vagus nerve can modulate airway narrowing and is a determinant of bronchomotor tone (Barnes, 1995). Acetylcholine released from postganglionic cholinergic nerves induces airway smooth muscle contraction and mucus secretion, effects that are blocked by muscarinic antagonists such as ipratropium bromide or atropine (Osmond, 1995).

In the PS of HRV of the rat, two distinct frequency bands can be identified, associated with sympathetic and vagal activity. The first, low frequency (LF) band is observed within the spectral band ranging from 0.015 to 1.0 Hz, and largely reflects sympathetic activity. The second, high frequency (HF) band (1.0 - 3.0 Hz), is very strongly correlated with vagal activity (Kuwahara et al., 1994; Sgoifo et al., 1994; Rubini et al., 1993; Cerutti et al., 1991; Japundzic, 1990). Thus LF:HF power ratio can be used as an index of relative sympathovagal balance in the rat.

These parameters can be obtained from freely moving animals through telemetric ECG recordings using implanted recording devices, thereby providing a non-invasive signature of vagal and sympathetic outflow that is not confounded either by anaesthesia or restraint.

In the present study, we examined changes in vagal and sympathetic outflow in freely moving, previously sensitized rats, following atropine, methacholine and antigen challenges. At the same time, airflow obstruction was assessed by whole body plethysmography.

These studies were conducted in collaboration with Dr. Veljko Djuric from the Department of Psychiatry and Behavioural Neurosciences at McMaster University. I developed/tested the algorithms of power spectral analysis of rat ECG signal and helped him to analyze the data and interpret the results.

The objective of this chapter is a) to develop algorithms suitable for processing ECG signals in a rat model and to compute the power spectrum of HRV signal during normal condition and b) to evaluate algorithms designed to compute PS/HRV during pharmacological interventions known to alter sympathovagal balance.

5.2 METHODS

Prior approval for this study was obtained from McMaster University Animal Care Committee and all procedures were conducted in accordance with the Guidelines of the Canadian Council of Animal Care.

5.2.1 Animal Surgery

All experiments were performed on freely moving male Sprague Dawley rats (Charles River Breeding Laboratories, Saint Constant, QC, Canada). The rats (10-14 weeks old at the beginning of each experiment) were housed in standard micro-isolator cages equipped with filter hoods, and specific-pathogen free environment under controlled temperature (20° C). They were maintained on a 12:12 hour light-dark cycle starting at 8 AM, with free access to standard rat chow and tap water.

Rats were first anaesthetized with ketamine hydrochloride (90 mg/kg) and xylazine (20 mg/kg) mixture given intramuscularly, and then implanted with a Data Sciences International (DSI) biopotential activity transmitter TA10ETA-F20 (10). The transmitter was placed in the back of the animals, and the two implanted ECG electrodes were respectively positioned on the right anterior chest wall, near the shoulder, and the left upper abdominal musculature, so that the heart was located between the two electrodes. The rats were given acetominophen for analgesia in the next two days.

5.2.2 Sensitization to Antigen

After recovery from surgery (2-3 weeks) the rats were sensitized to ovalbumin (OA). The rats were first immunized with a subcutaneous injection of 10 μg of OA (grade V, Sigma Chemical Co., St Louis, MO) mixed with 4.4 mg aluminum hydroxide

gel and an ip injection of Bordetella pertussis vaccine (Connaught Laboratories, Willowdale, Ontario, Canada; 1 ml containing 10^{10} organisms). Fourteen days later, the animals were boosted with a subcutaneous injection of 10 μg of OA in aluminum hydroxide gel (Djuric, 1995).

5.2.3 Experimental procedure

ECG signal was recorded before, during and after atropine, methacholine, and antigen challenges. Three weeks following sensitization to OA rats were injected with five consecutive intraperitoneal injections of 0, 0.5, 2.5, 5.0 and 7.5 mg/kg of atropine methyl bromide (Sigma Chemical Co., St Louis, MO) each given at 30 min intervals. Atropine methyl bromide has no CNS penetration, being a quaternary amide. Seventy-two hours later the rats inhaled aerosols of saline and four-fold increasing concentrations of methacholine (Sigma Chemical Co., St Louis, MO) ranging from 4 mg/ml to 256 mg/ml, each for 5 min. ProNeb compressor nebulizer with an airflow of 5 litres/min (Pari-Werk GmbH, Starnberg, Germany) was used to generate aerosols. The order of atropine and methacholine challenge was balanced across the rats. Seventy-two hours after the last atropine or methacholine challenge (28 days after initial sensitization) the rats were subjected to antigen challenge (inhalation of 5% OA for 5 min).

5.2.4 Measurement of bronchoconstriction

In each animal, airflow was assessed using non-invasive bias flow ventilated whole body plethysmographic technique and non-invasive pulmonary analyser (Buxco Electronics Inc., Sharon, CT, USA) as was described previously (Djuric, 1998).

Experience to date has shown that the enhanced pause (Penh) is a reliable and sensitive index of bronchoconstriction, superior to other derived parameters such as box pressure or box flow, in assessing the degree of bronchoconstriction (Djuric, 1998, Hamelman, 1997). This index of bronchoconstriction was calculated on-line for every breath from the air flow derived parameters.

Baseline data were recorded for 5 min at the end of 10-15 min habituation period in the plethysmograph. The animal was then moved to an identical chamber for a 5 min challenge with either nebulized antigen, saline or methacholine. Following challenge, the animal was returned to the plethysmograph and data were recorded for 10 minutes. Penh values averaged across ten consecutive 1 min periods after challenge were considered to be an index of bronchoconstriction.

5.2.5 Processing of ECG signal and power spectral analysis of heart rate variability

A telemetry system (Data Sciences International, St. Paul, Minnesota) was employed for gathering ECG data from freely moving rats. The ECG signal was digitized using a 12 bit analog conversion (DATAQ Instruments, Akron, Ohio) and recorded on a Pentium-90 MHz computer (Dell Dimension XPS90, Dell Computer Corporation, Austin, Texas) using a 1 kHz sampling frequency.

Data were processed as follows. A QRS detection algorithm was implemented in the software to locate stable and noise independent fiducial point on the R wave (Ruha, 1997). An R-R interval series was then generated from the continuous ECG data. A beat-to-beat heart rate variability signal was computed, and then resampled at 6 Hz using linear interpolation to obtain an equally sampled time series. A record length of 768

points from the resampled signal (128 seconds) was selected for power spectral analysis. The mean value of the signal was removed and the equally sampled HRV signals were fed through a fourth order high pass Butterworth filter with a cut-off of 0.015 Hz. Blackman-Tukey power spectral method was then applied to demeaned filtered heart rate variability data. The information contained within the power spectrum was analyzed in the following manner. From published literature we found much of the LF power was in the range of 0.015 – 1 Hz and HF power was in the range 1.0 – 3.0 Hz (Kuwahara, 1994, Cerutti, 1991). The maximum peak amplitudes of the LF and HF bands were identified. The frequencies at which these peaks occurred (central frequencies) were obtained and the area subtended by each spectral band was then computed by numerically integrating the power contained therein. This was expressed in absolute units $(beats/min)^2$ /Hz. In addition, the normalized areas within both LF and HF bands were derived by dividing the integrated power within each band by the total power contained in the entire spectrum. The LF:HF ratio was computed as the ratio of these normalized areas.

5.2.6 Bronchoalveolar lavage

Bronchoalveolar lavage (BAL) was done 24 hours after antigen challenge. Rats were anaesthetized with Halothane (Halocarbone Laboratories, River Edge, NJ) and then euthanised by exanguination through the inferior vena cava. The lungs were lavaged with 10 ml of sterile PBS in consecutive fractions of 5, 2 and 3 ml. The BAL was centrifuged for 10 min at 1100 rpm.

5.2.7 Cell Counting

Total cell counts were done using Trypan Blue stain (Gibco Lab, NY) and were counted in Neubauer chamber (VWR/Canlab, Toronto, Ontario, Canada) under a light microscope. Differential cell counts were determined from cytospin preparations stained by DiffQuick stain (Baxter Scientific, McGaw Park, Il) under a light microscope using basic morphology. Percentage and absolute number of each cell type were calculated from the average of 400 consecutively counted cell under X400 magnification. Allergen-induced airway inflammation was assessed by counting inflammatory cells (neutrophils and eosinophils) relative to mononuclear cells (macrophages, monocytes and lymphocytes).

5.2.8 Data Analysis

All respiratory and heart rate variability data after either methacholine or atropine challenge were analyzed by repeated measures analysis of variance (in order to determine a cumulative dose response). Responses to antigen challenge were analyzed by repeated measures analysis of variance (LF:HF power, before and after antigen challenge), one-way analysis of variance (comparing indices of airway inflammation between the group challenged with antigen and the group challenged with saline) and by a split-plot analysis of variance (comparing the group challenged with antigen and the group challenged with saline with respect to bronchoconstriction and respiratory rate). The level of statistical significance was set at $p < 0.05$. All data were expressed as mean $\pm$ standard error of mean (SEM).

5.3 RESULTS

5.3.1 Power Spectral Analysis of Heart Rate Variability

Different patterns of heart rate variability were observed across four experimental conditions in this study. The atropine challenge reduced, while methacholine and antigen challenges enhanced beat-to-beat heart rate variability that was observed at baseline (Figure 5.1). Corresponding PS of HRV revealed that atropine challenge enhanced LF (predominately sympathetic) spectral component, while methacholine and antigen challenges enhanced HF (parasympathetic) component (Figure 5.2).

5.3.2 Effect of Cumulative Atropine & Methacholine Challenges on Sympathovagal Balance

Increasing concentrations of cholinergic antagonist, atropine, induced rise in sympathetic dominance and dose-dependent increase of LF:HF power ratio ($p = 0.005$, Figure 5.3). Increasing concentrations of inhaled cholinergic agonist methacholine, led to dose-dependent decrease of LF:HF power ratio ($p = 0.001$) indicating methacholine-induced rise in parasymapthetic dominance relative to baseline (Figure 5.4).

5.3.3 Effect of Antigen Challenge on Sympathovagal Balance

Seventy-two hours after the last atropine/methacholine challenge rats were subjected to antigen challenge (inhalation of 5% OA for 5 min). Exposing sensitized rats to nebulized antigen led to profound changes in their autonomic balance ($p = 0.03$) indicating antigen-induced rise in vagal activity (Figure 5.5).

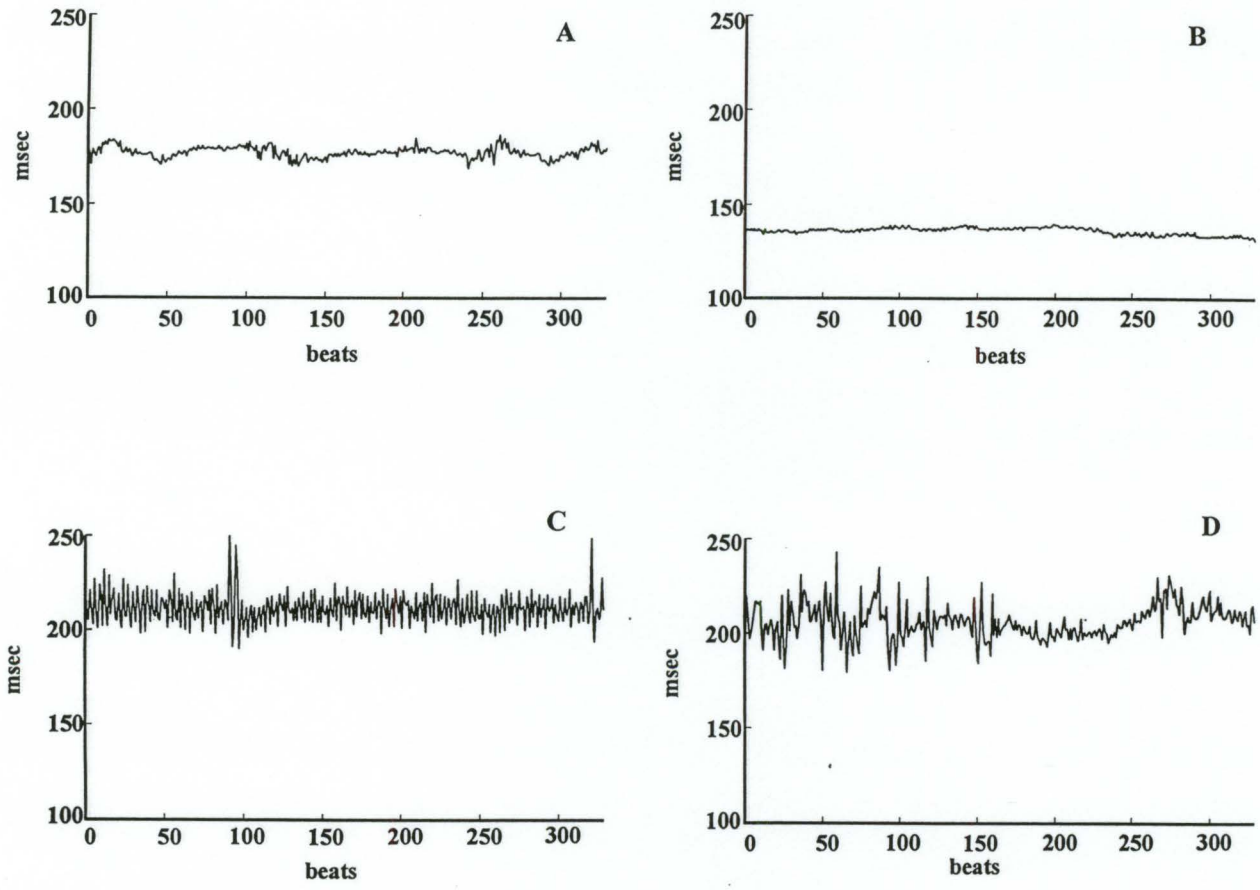

Figure 5.1 Example of R-R interval variability series obtained under four experimental conditions: A) at baseline; B) following i.p. injection of 7.5 mg/kg atropine; C) following 5 min inhalation of 256 mg/ml methacholine; and D) following inhalation of nebulized antigen. The presence of high frequency oscillations (spikes) is an indication of increased vagal activity. Note the absence of high frequency oscillations following atropine challenge and their presence following methacholine and antigen challenges.

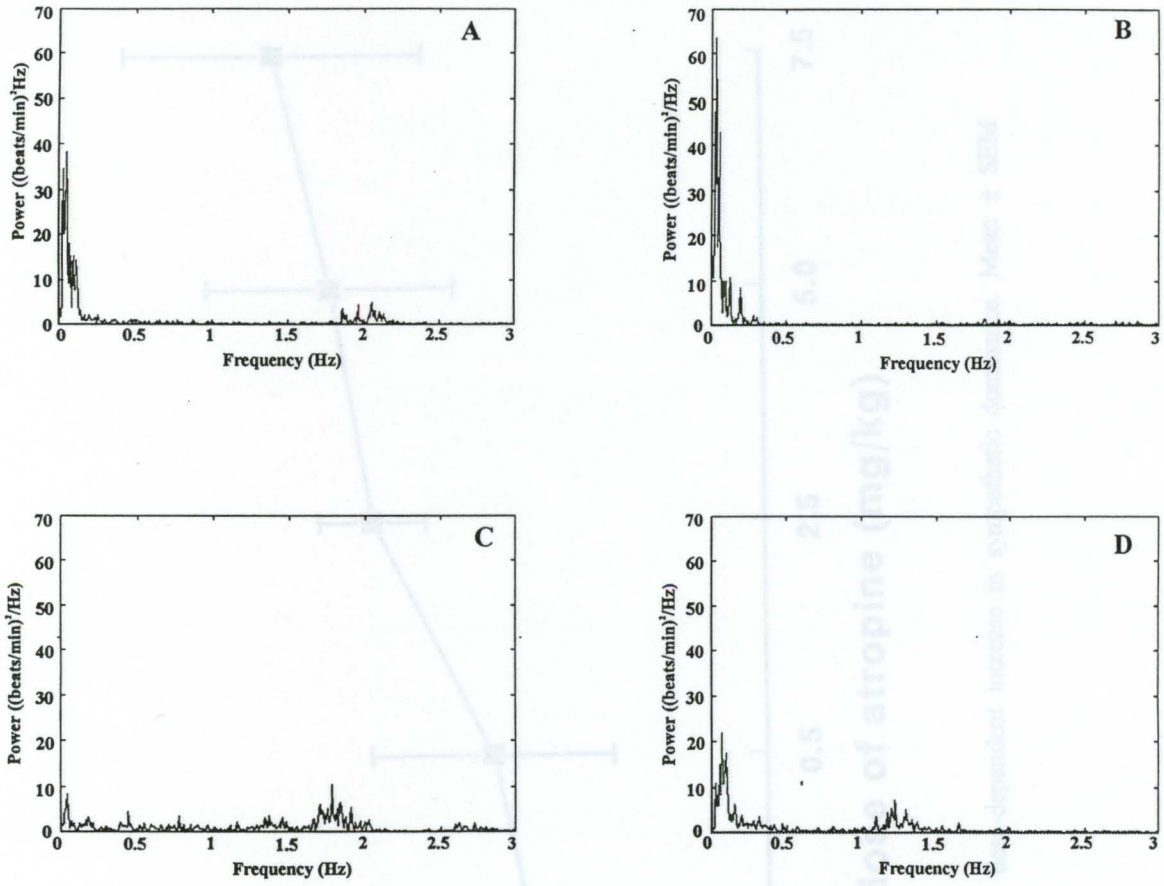

Figure 5.2 Effect of experimental manipulation on power spectrum of heart rate variability. Representative spectrum A) at baseline; B) following injection of 7.5 mg/kg atropine; note vagolytic effect of atropine: high frequency peak (associated with parasympathetic activity) has disappeared completely; C) following 5 min inhalation of 256 mg/ml methacholine; note vagal dominance: low frequency peak (associated with sympathetic activity) has disappeared completely; and D) following inhalation of nebulized antigen; note enhanced high frequency area and a reduction in low frequency area.

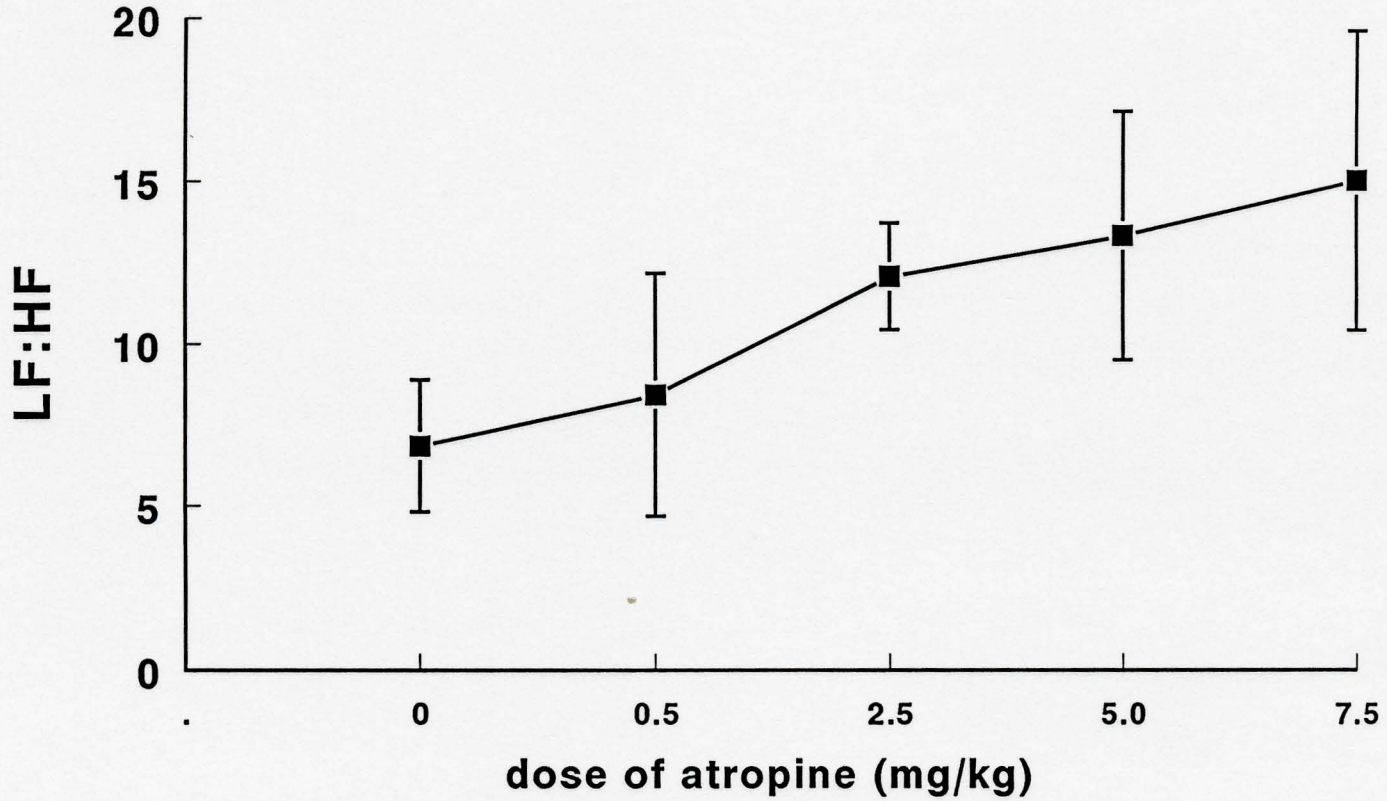

Figure 5.3 Atropine-induced dose-dependent increase in sympathetic dominance. Mean ± SEM LF:HF power

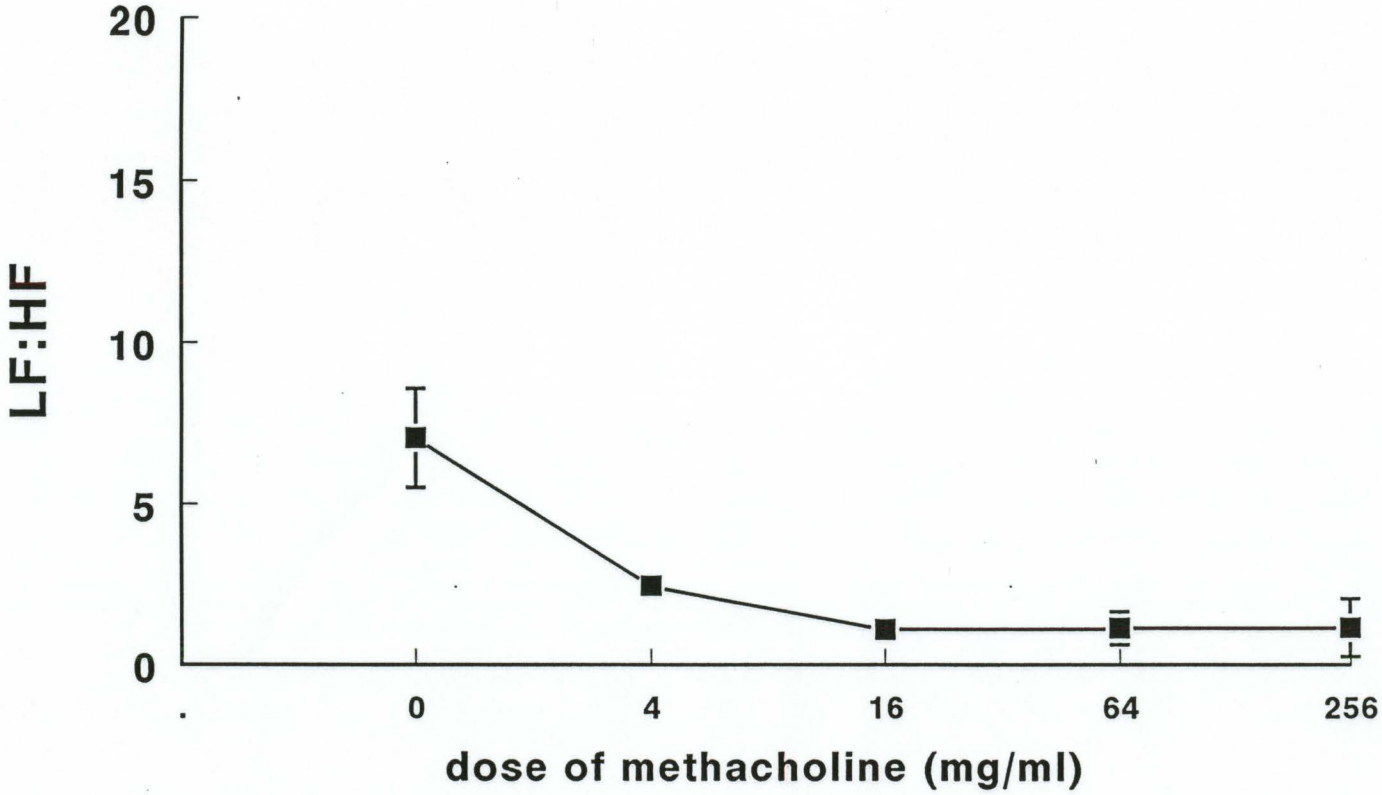

Figure 5.4 Methacholine-induced increase in parasympathetic dominance. Sympathetic (LF) to parasymapthetic (HF) power ratio declined with increasing doses of inhaled methacholine. Mean ± SEM LF:HF power.

Figure 5.5 Allergen-induced parasympathetic dominance in the rat. Sympatho-vagal balance before and after 5 min inhalation of nebulized OA. Mean ± SEM LF:HF power for two independent groups.

5.3.4 Effect of Cumulative Atropine and Methacholine Challenges on Breathing

Consecutive injections of atropine had no effects on respiration. There was no statistically significant effect of atropine on either bronchoconstriction ($p = 0.541$) or respiration rate ($p = 0.525$, Figure 5.6). Exposing rats to nebulized methacholine led to dose-dependent increase in bronchoconstriction ($p < 0.001$) and a dose-dependent decrease of respiration rate ($p< 0.001$, Figure 5.7).

5.3.5 Effect of Antigen Challenge on Breathing

Differences between sensitized SD rats that were challenged with antigen as compared to saline were clearly established. Five-minute exposure to aerosolized antigen resulted in laborious breathing. There was a statistically significant difference between the two groups across the 10 min post-challenge period with respect to bronchoconstriction ($p = 0.006$) and frequency of respiration ($p < 0.001$, Figure 5.8).

5.3.6 Effect of Antigen Challenge on Airway Inflammation

The difference in *the early phase reaction* was accompanied by a difference in cell counts taken 24 hours after the challenge. Total number of white blood cells obtained from BAL fluids was greater in rats challenged with OA ($p = 0.016$) indicating more pronounced inflammation. In addition, BAL fluids from animals challenged with antigen had relatively more inflammatory cells: neutrophils ($p < 0.001$) and eosinophils ($p<0.001$) and consequently, relatively fewer mononuclear cells ($p < 0.001$, Table 5.1). Table 5.1 shows the effect of 5 min exposure to nebulized ovalbumin on the immune cell profile of male SD rats that were challenged either with antigen or saline. Each value

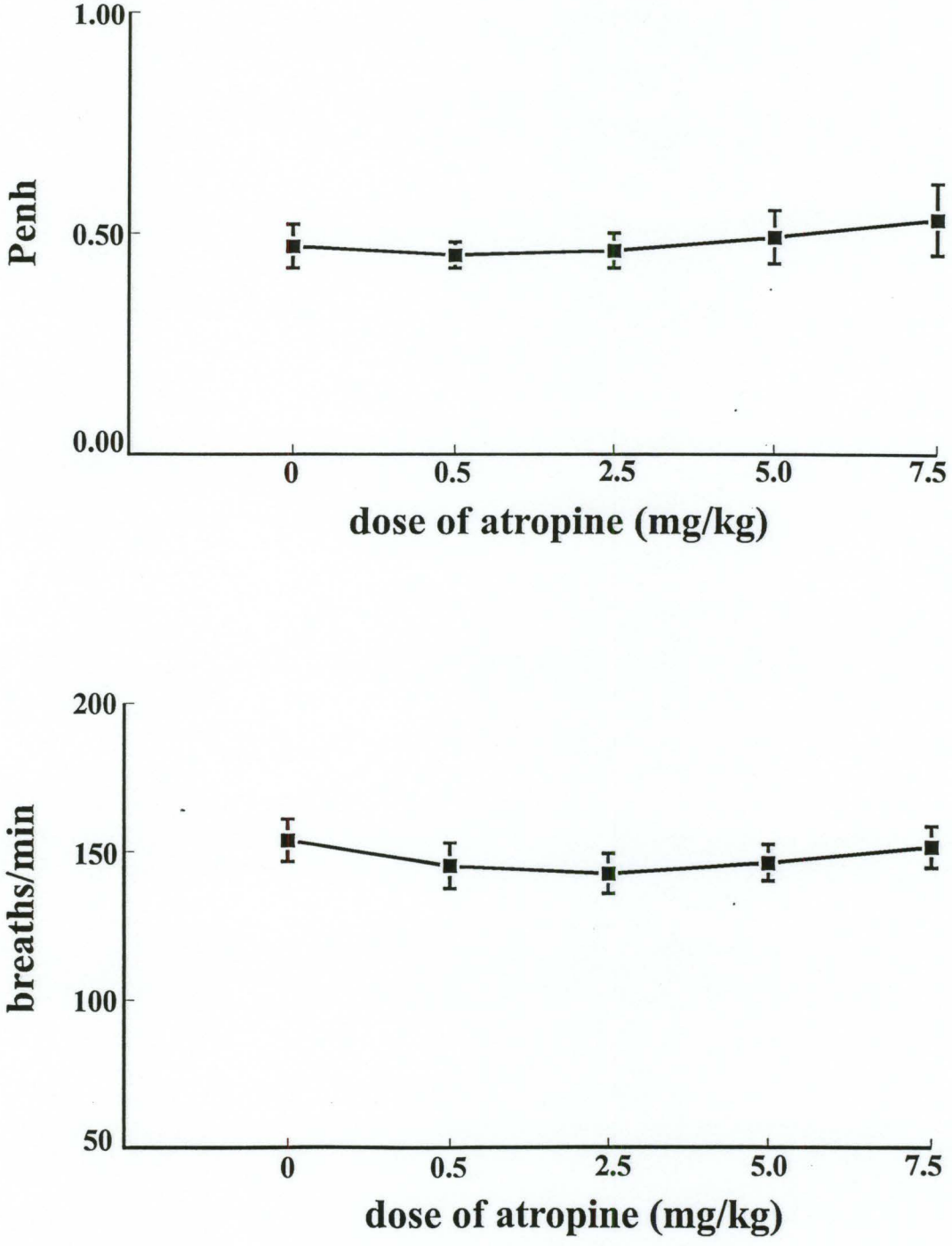

Figure 5.6 Breathing following consecutive ip injections of atropine. Increasing doses of atropine did not have any effect on bronchoconstriction (upper panel) and respiratory rate (lower panel). Mean SEM ± Penh values and mean ± SEM frequencies, respectively.

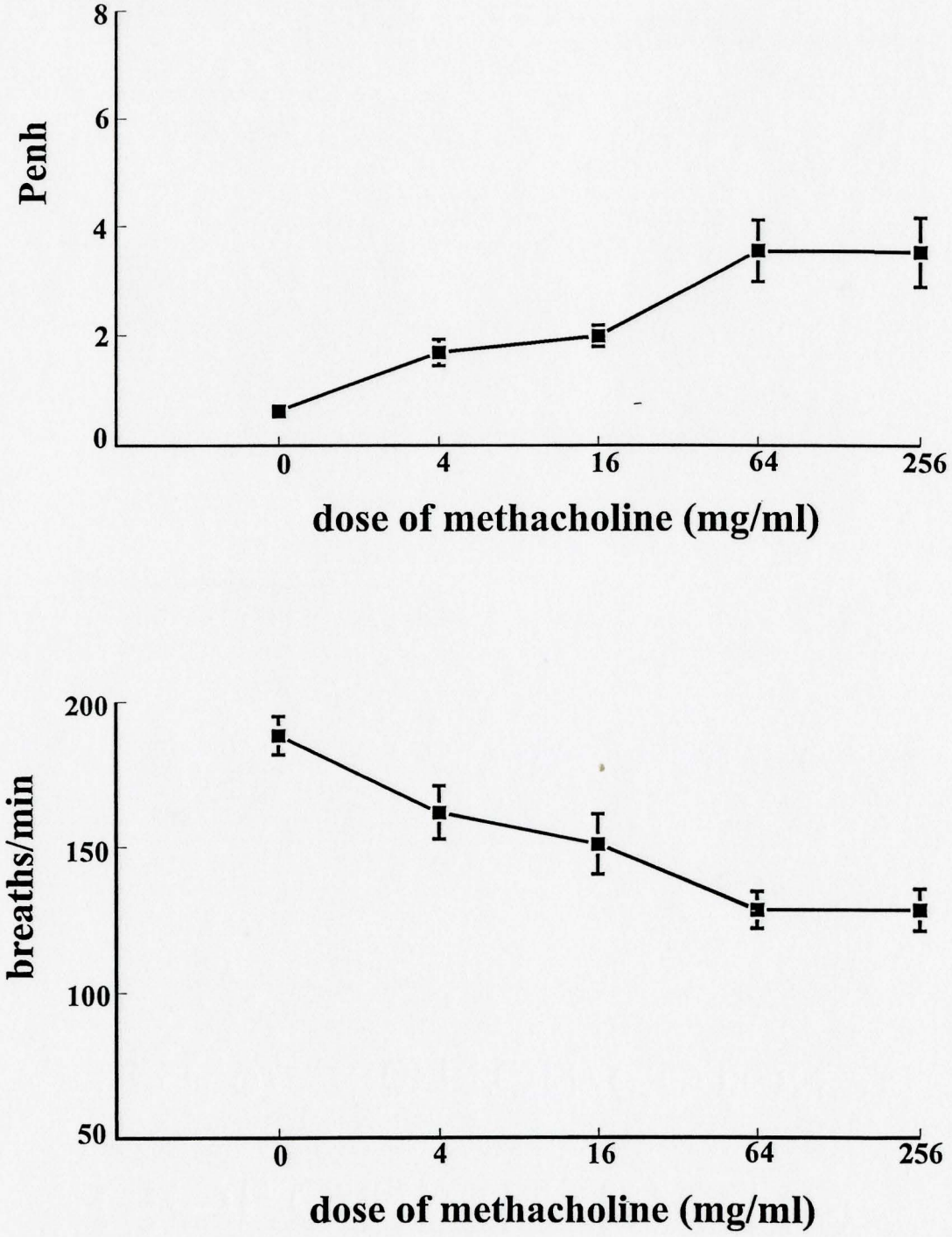

Figure 5.7 Changes in respiration following 5 min inhalation of nebulized methacholine in freely moving male Sprague Dawley rats. The rats were found to have increasing difficulty breathing following 5 min inhalation of increasing doses of methacholine. Mean SEM ± Penh values (upper panel) and mean ± SEM frequencies (lower panel).

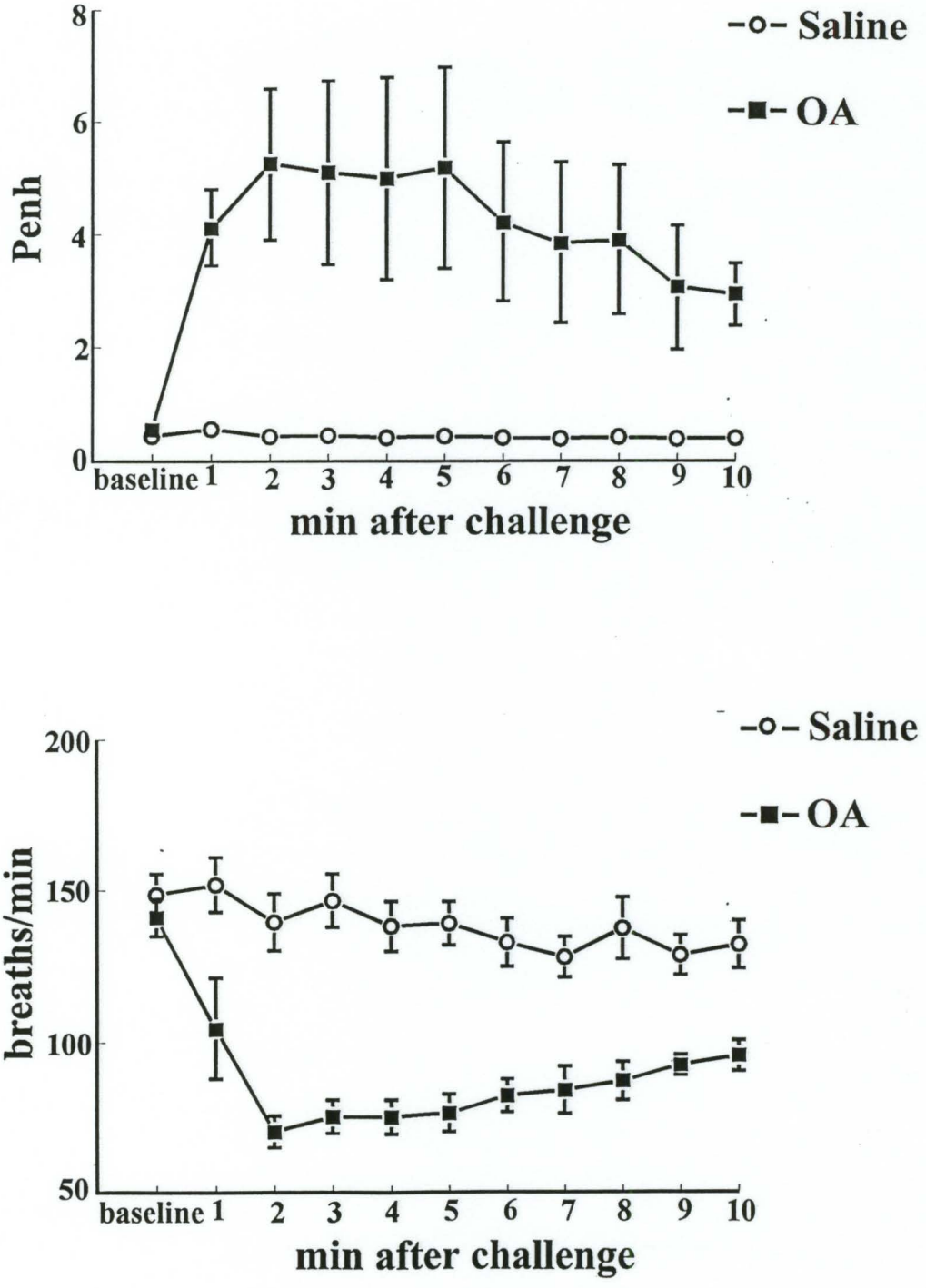

Figure 5.8 Allergen-induced bronchoconstriction in the rat. Sensitized male Sprague Dawley rats exposed to nebulized antigen developed marked bronchoconstriction as indicated by their high Penh values and a significant drop of respiratory rate. No indication of bronchoconstriction and no change in frequency of respiration was observed in sensitized animals that were exposed to nebulized saline. Mean ± SEM Penh values (upper panel) and mean ± SEM frequencies (lower panel) for two independent groups.

represents mean ± SEM for a given cell type identified in the BAL fluid 24 hours after the challenge.

Table 5.1 Allergen-induced airway inflammation.

{PRIVATE }	Total number of{PRIVATE } white blood cells x 10^6	% Mononuclear cells	% Neutrophils	% Eosinophils
Saline (n = 9)	1.03 ± 0.11	98.62 ± 0.39	1.08± 0.30	0.30± 0.17
{PRIVATE }OA (n = 9)	2.30 ± 0.46	57.21± 5.43	26.26 ± 4.78	16.53± 3.53

5.4 PHYSIOLOGICAL RELEVANCE

In vivo animal model is an indispensable tool for the study of pathophysiology of asthma. They offer the possibility to examine the mechanisms of asthma at a depth not possible with human studies, and to investigate risk factors and potential treatment interventions at a preclinical stage. Procedures involving anesthesia, surgical interventions and/or removal of tissues and cells from the animal for *in vitro* measurements provide only imperfect correlates of the *in vivo* pathophysiological response, and in particular of the integrative control mechanisms involved. However, in recent years, *in vitro* rather than *in vivo* observations often direct asthma related research (Persson, 1997).

In this study, we present an *in vivo* model suitable for the study of the relationship between the autonomic nervous system, the immune system and airway hyperresponsiveness in spontaneously breathing, unrestrained animals. The model provides simultaneous measurements of the respiratory function (whole body plethysmography), and of the autonomic nervous system (ECG telemetry) in conscious rats.

This experimental approach is uniquely suitable for longitudinal studies involving large numbers of animals. The only invasive procedure involved in our model is the minor surgical intervention (performed a number of weeks prior to the experiments) to implant the transmitters. Thus, the actual data collection is completely non-invasive and can be performed repeatedly during the lifetime of the experimental animal. The two components of our experimental model can operate either simultaneously or independently providing an opportunity to monitor respiratory and/or autonomic function during different phases of an experiment. Other current animal models of increased airway responsiveness preclude such long-term *in vivo* assessments.

The present study describes respiratory and autonomic changes following methacholine, atropine, and antigen challenges in freely moving rats under controlled experimental conditions. Methacholine- and antigen-induced bronchoconstriction was paralleled by a decrease in frequency of respiration and an increase in parasympathetic (vagal) activity. The methacholine- and antigen-induced changes in respiration are consistent with the previous observations (Djuric, 1998). Changes in heart rate during intravenous allergen challenge have been reported in mice (Martin, 1993). To the best of our knowledge, this is the first evidence of vagally mediated cardiac reflex response following challenge with either nebulized methacholine or nebulized antigen. This response was present in all animals suggesting that changes in respiratory parameters reflect a general shift in autonomic regulation.

There was no cumulative dose response to atropine, neither with respect to bronchoconstriction nor with respect to respiratory rate. This finding is in accordance with earlier studies reporting that atropine had no effects on respiration in dogs (Hsu,

1985) and monkeys (Birnbaum, 1988). On the other hand, as indicated by increases in LF:HF power ratio, there was a marked dose-dependant vagolytic effect of atropine indicating that sympathovagal balance can be manipulated in spite of any apparent changes in respiration.

The BAL fluids from rats challenged with antigen contained significantly more white blood cells, particularly inflammatory cells (eosinophils and neutrophils). This profile is similar to the cellular distribution in BAL fluid recovered from asthmatics after exposure to allergen. Data from this study are in line with our previous findings that severity of bronchoconstriction is highly predictive of subsequent airway inflammation.

The methodology outlined above can be used to further address relationship between autonomic function and experimental asthma. Recently, Djuric et al. (1998) reported that genetically transmitted autonomic dysfunction (cholinergic hyperresponsiveness) of Flinders Sensitive Line (FSL) rats was highly predictive of their increased susceptibility to allergen-induced bronchoconstriction and inflammation of the airways. Other data (Djuric, 1997) indicate that it is the heightened basal sympathetic tone that predisposes the FSL rats to their cholinergic- and antigen hyperresponsiveness. Chronic inflammatory diseases such as rheumatoid arthritis, insulin-dependent diabetes mellitus and multiple sclerosis have been associated with an increase in baseline sympathetic tone (Wietse, 1996). This alteration of autonomic function may be an index of disease and may also in part determine its expression. More experiments are needed in order to establish whether there is a similar change in symapatho-vagal balance associated with chronic

inflammation of the airways, and whether high resting sympathetic tone invariably predisposes to heightened responsiveness to vagal stimulation (Spaziani et al., 1996).

Many medications that are currently prescribed for asthma (β2 agonists, anticholinergics, theophylline) are sympathomimetic, but we know very little about their short- and long-term effects on autonomic nervous system function. Studying how the autonomic nervous system responds to repeated allergen challenges and concurrent treatment with anti-asthma medications may elucidate the potential neural mechanisms underlying airway hyperresponsiveness and other phenomena attributable to bronchial asthma.

Our data demonstrate that changes in the autonomic nervous system occur in parallel with respiratory changes following methacholine or antigen challenge. This provides additional evidence supporting the role of the autonomic nervous system in asthma. Quantitative information derived from the power spectral analysis of heart rate variability reflects changes in sympathetic and parasympathetic regulatory activities that occur during experimental asthma. Methacholine- or antigen-induced bronchoconstriction results in a general change in autonomic balance and development of parasympathetic dominance. Neural factors are involved in response to antigen challenge and thus may be relevant for the expression of asthma. Studies involving unanaesthesized, non-intubated animals may lead to important insights into neuro-immune regulation in experimental asthma. Studying autonomic activation can be important for better understanding of various phenomena attributable to bronchial asthma.

Chapter 6

Applications of Time-Frequency Analysis in Physiological Studies

6.1 INTRODUCTION

In this chapter, we present applications of Time-Frequency Analysis (TFA) of HRV signal recorded during non-stationary states in human volunteers. Specifically we discuss the results of two studies conducted on healthy human subjects during tilt and during sleep.

6.2 TIME-FREQUENCY ANALYSIS OF HRV DURING HEAD-UP TILT

The objective of this study is to evaluate the TFA algorithm during head-up tilt (passive tilt). Once a human subject assumes the upright posture, there is increased vulnerability to the effects of gravity on the circulation (Wieling and Lieshout, 1997). The crucial problem posed by the upright posture is the vertical displacement of blood below the heart resulting in a decline in venous return. Because the heart cannot pump out what it does not receive, ventricular stroke volume declines with each beat and

arterial pressure tends to fall. A series of cardiovascular-regulatory mechanisms or reflexes are activated to offset the imbalances in the circulation. The dynamics of the underlying cardiovascular control mechanisms should be taken into account when investigating orthostatic circulatory control (Wieling and Lieshout, 1997). An investigation of passive tilt may help us to understand the cause of certain cardiovascular pathophysiology such as vasovagal syncope.

6.2.1 Methods

6.2.1.1 Subjects

Seven subjects (four male and three female; average age 24 ± 1 years) participated in this study. The studies were conducted in the Radiology Unit at McMaster University Medical Center. Ethics approval was obtained from the McMaster University Medical Center Hospital Ethics Advisory Committee prior to commencement of the study. Written informed consent was obtained from each subject prior to the data recording.

6.2.1.2 Measurements

The subjects were instructed to lie on an electrical tilt table (angle adjustable from 0^{o} to head-up 90^{o}). The electrocardiogram (ECG) signal, the respiration signal and the blood pressure signal were amplified through an ECG monitor (Hewlett-Packard), a respiration monitor (Narco Scientific) and a blood pressure monitor (Finapres) respectively. The outputs of all the monitors were connected to the CODAS data acquisition system and interfaced with a personal computer (Gateway 2000/486).

6.2.1.3 Experimental Design

The experimental recording took 75 minutes. The tilt table was set to the varying angles according to the following protocal, where angle 1 and angle 2 were randomly assigned to either 30° or 60°. This experimental design ensures that subjects go through all three different angles. Figure below outlines the experimental protocal.

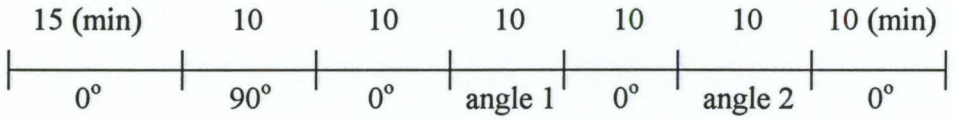

6.2.2 Wigner-Ville Distribution of HRV during Tilt

Three of the seven data sets were discarded since the respiratory frequency was too low (~0.15 Hz), which leads to a combined peak in the PS/HRV consisting of LF & HF peaks. In each of the remaining HRV data from four subjects there were three major transition periods: (1) Supine to 90° tilt; (2) Supine to 60° tilt; (3) Supine to 30° tilt. A five-minute segment of HRV recorded in the supine state and three five-minute (different angles) segments during tilt were subjected to analysis. There were four five-minute segments for each subject. For each data set, the Wigner-Ville distribution, as well as AR and BT power spectra, were calculated. The results of WVD are shown in Figure 6.1-6.4 and the results of AR and BT methods are illustrated in Figure 6.5-6.6. It can be seen that the LF:HF ratio in the time-frequency plane increases as the tilt angle increases.

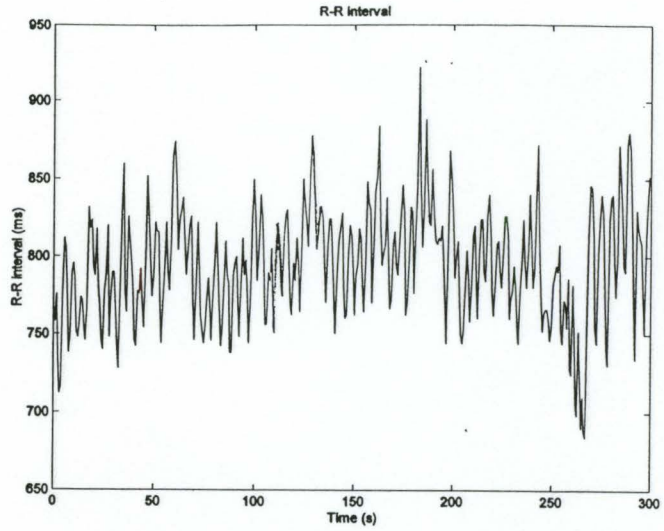

(a)

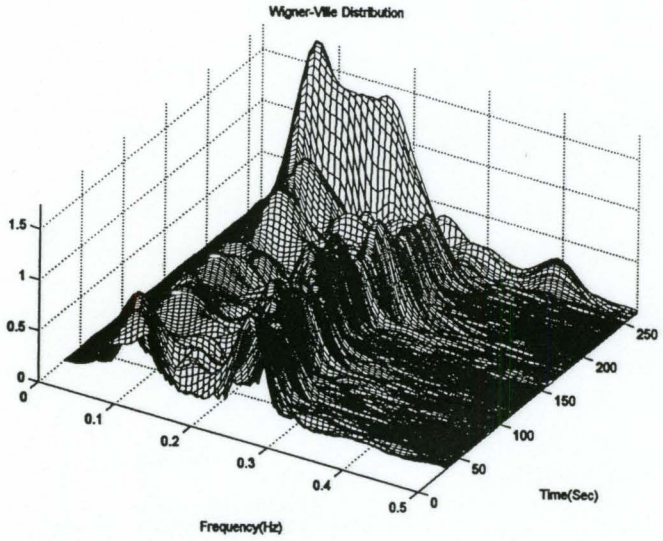

(b)

Figure 6.1 Example of Wigner-Ville distribution obtained during supine condition: (a) R-R interval vs. time. (b) Wigner-Ville distribution 3-D plot (power vs. time & frequency). (c) Wigner-Ville distribution 2-D contour plot. (d) Power (LF & HF) and LF:HF ratio vs. time plotted along with R-R interval vs. time for comparison.

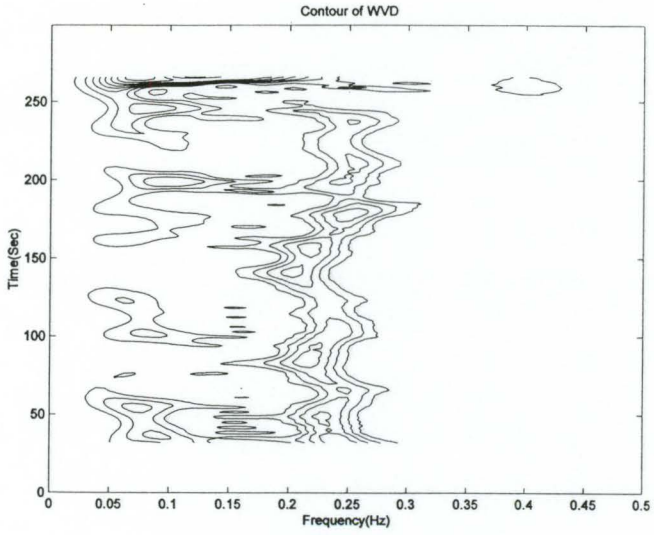

(c)

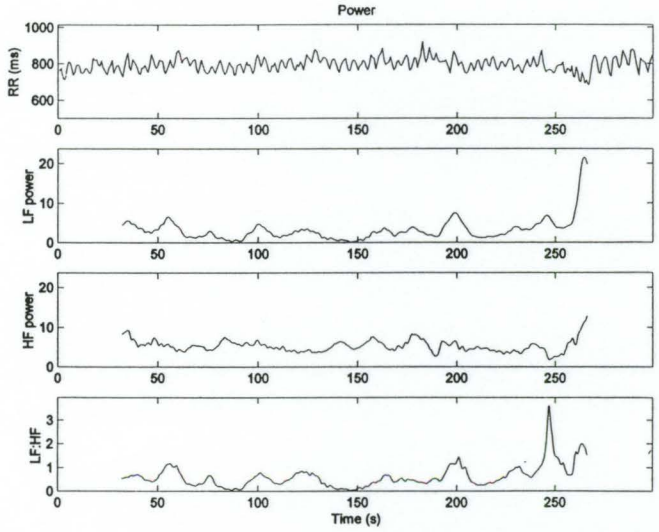

(d)

Figure 6.1 (*contd.*)

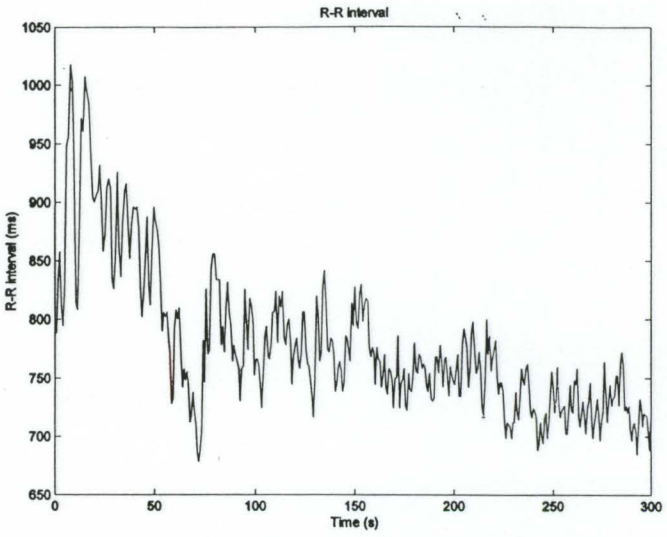

(a)

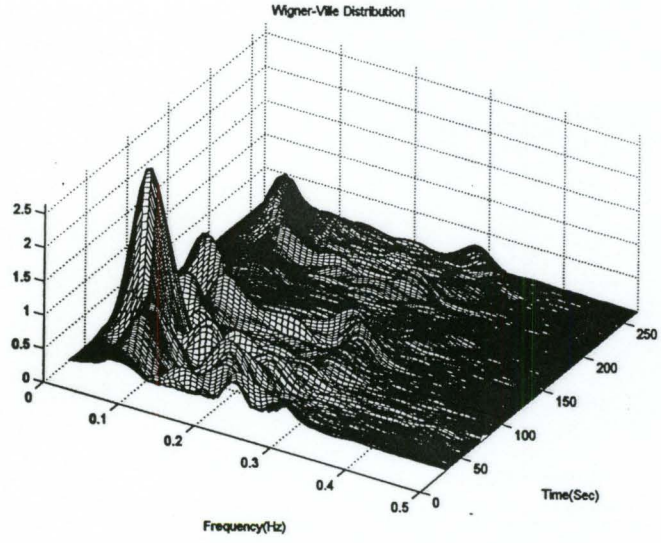

(b)

Figure 6.2 Example of Wigner-Ville distribution obtained during 30° tilt: (a) R-R interval vs. time. (b) Wigner-Ville distribution 3-D plot (power vs. time & frequency). (c) Wigner-Ville distribution 2-D contour plot. (d) Power (LF & HF) and LF:HF ratio vs. time plotted along with R-R interval vs. time for comparison.

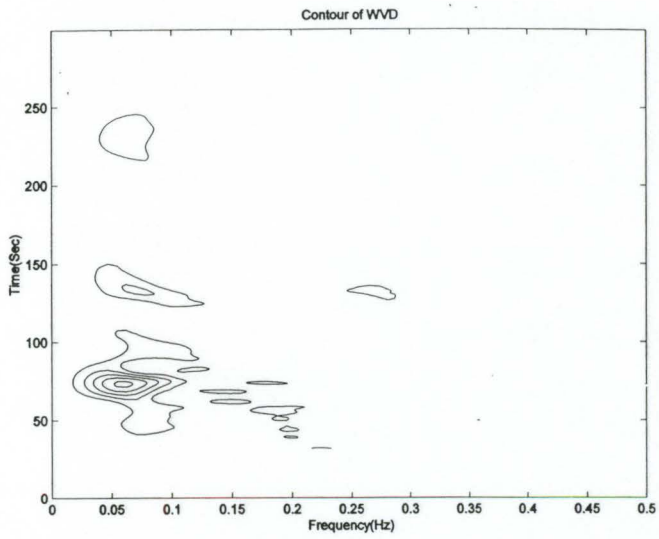

(c)

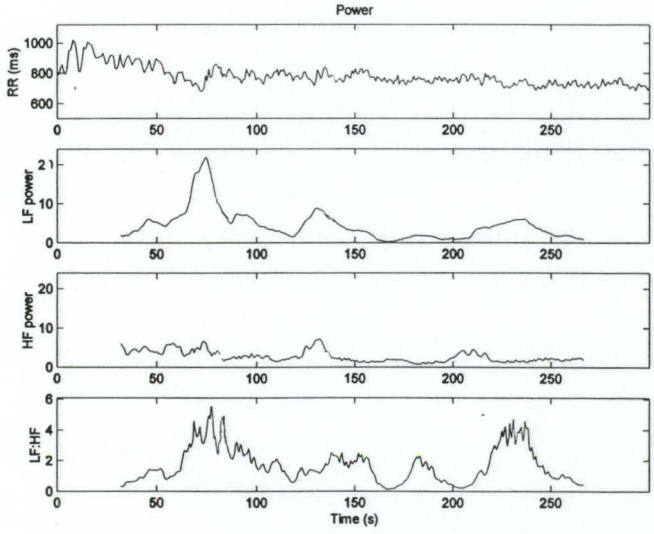

(d)

Figure 6.2 (*contd.*)

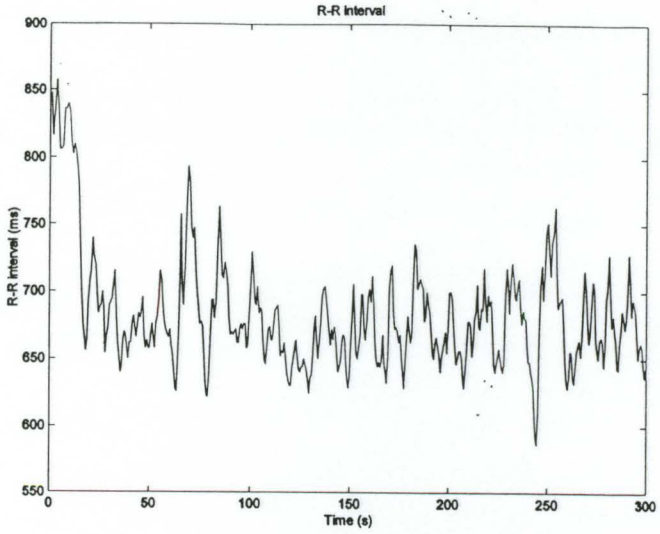

(a)

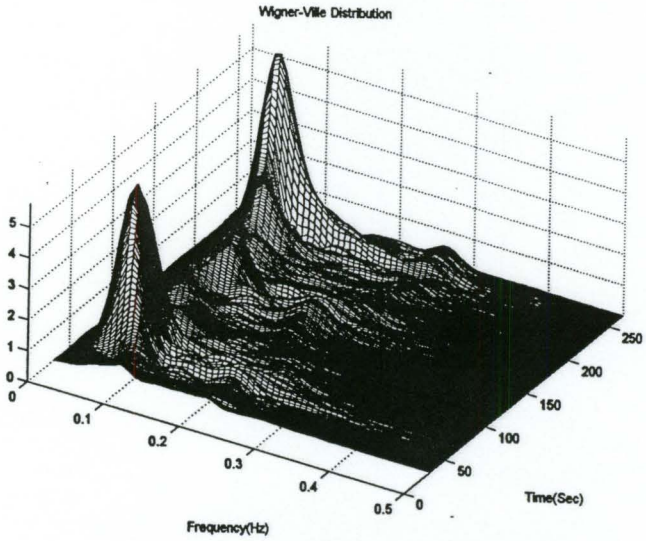

(b)

Figure 6.3 Example of Wigner-Ville distribution obtained during 60° tilt: (a) R-R interval vs. time. (b) Wigner-Ville distribution 3-D plot (power vs. time & frequency). (c) Wigner-Ville distribution 2-D contour plot. (d) Power (LF & HF) and LF:HF ratio vs. time plotted along with R-R interval vs. time for comparison.

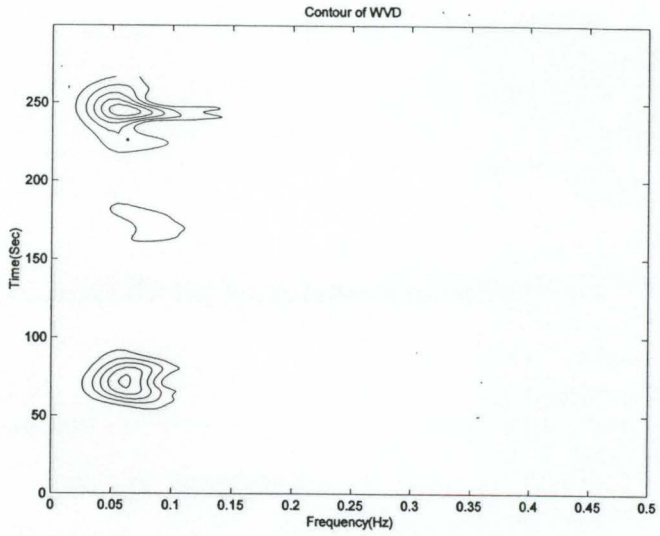

(c)

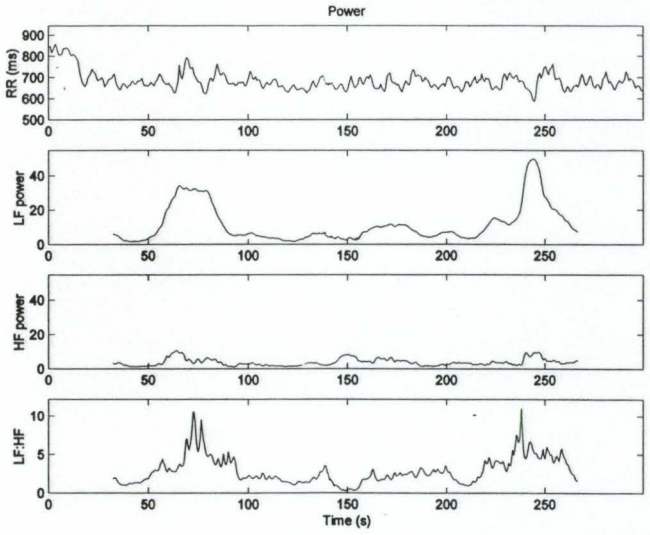

(d)

Figure 6.3 (*contd.*)

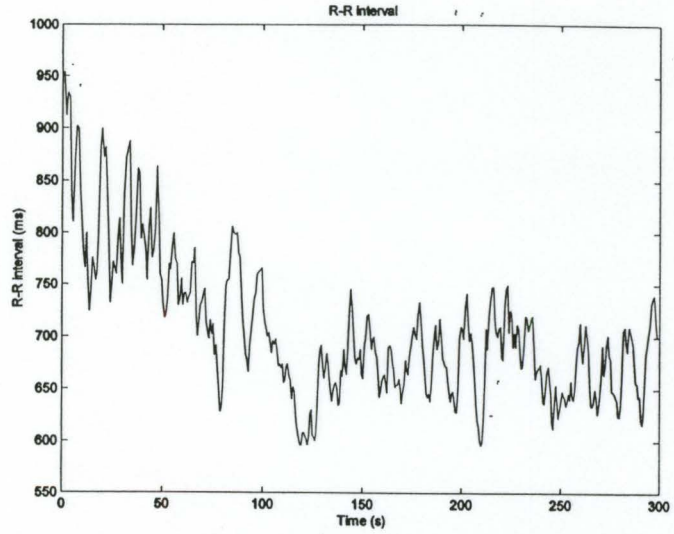

(a)

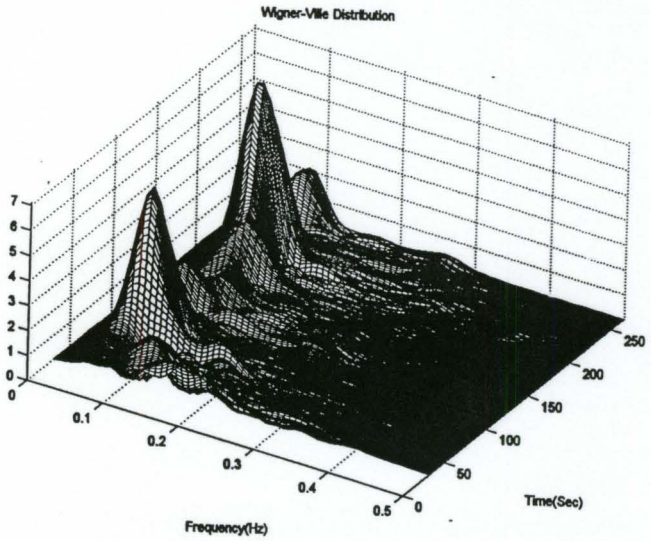

(b)

Figure 6.4 Example of Wigner-Ville distribution obtained during 90° tilt: (a) R-R interval vs. time. (b) Wigner-Ville distribution 3-D plot (power vs. time & frequency). (c) Wigner-Ville distribution 2-D contour plot. (d) Power (LF & HF) and LF:HF ratio vs. time plotted along with R-R interval vs. time for comparison.

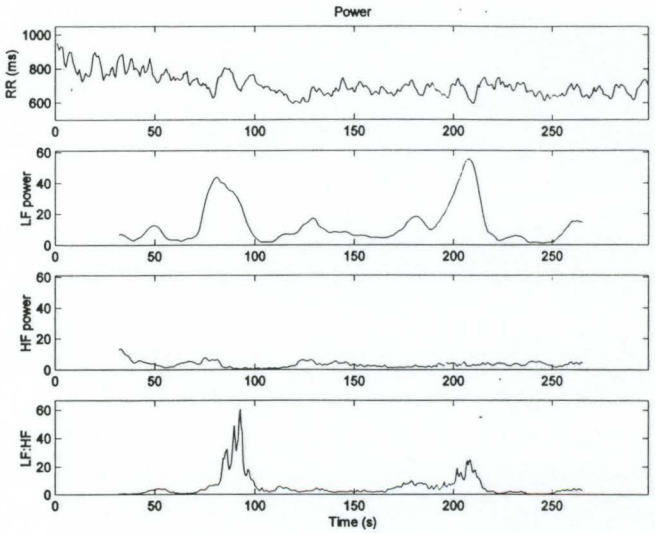

(c)

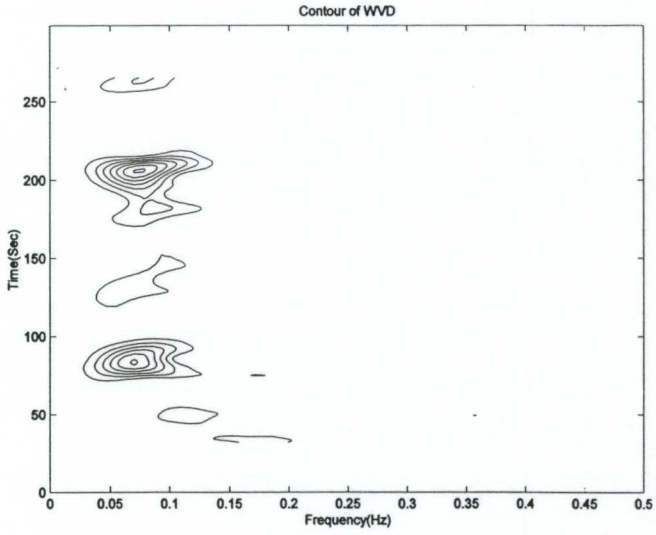

(d)

Figure 6.4 (*contd.*)

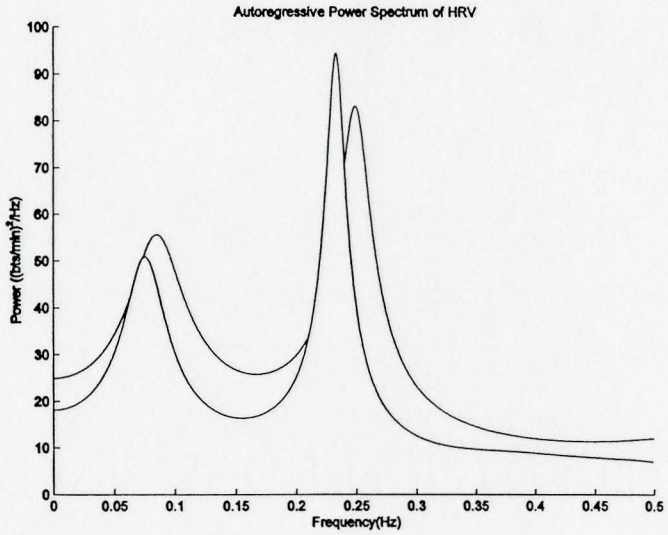

(a)

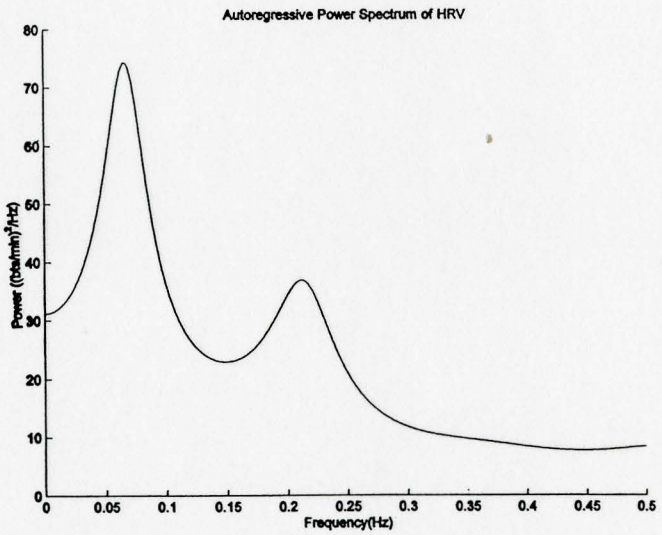

(b)

Figure 6.5 Autoregressive power spectrum of HRV signal during supine and tilt: (a) Supine. (b) 30 degree tilt. (c) 60 degree tilt. (d) 90 degree tilt.

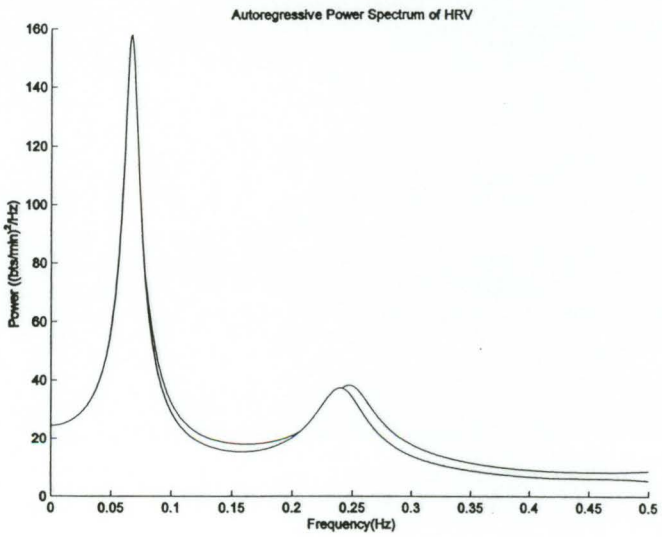

(c)

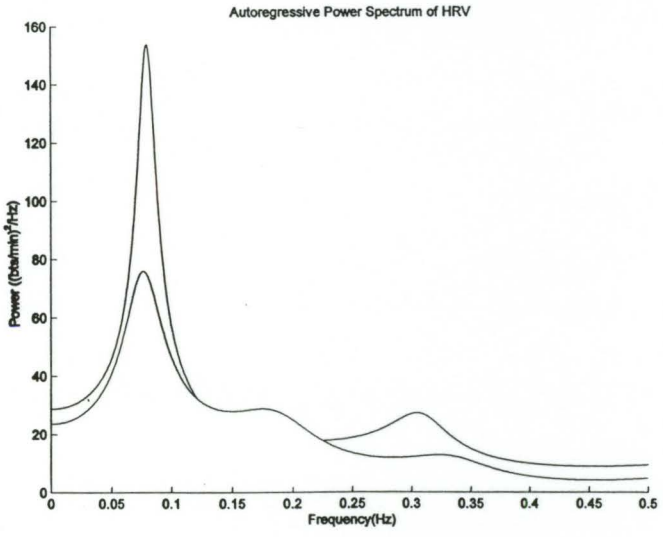

(d)

Figure 6.5 (*contd.*)

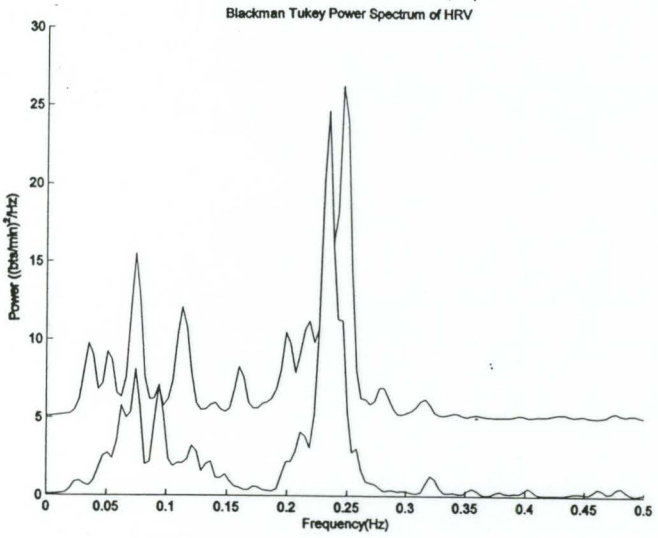

(a)

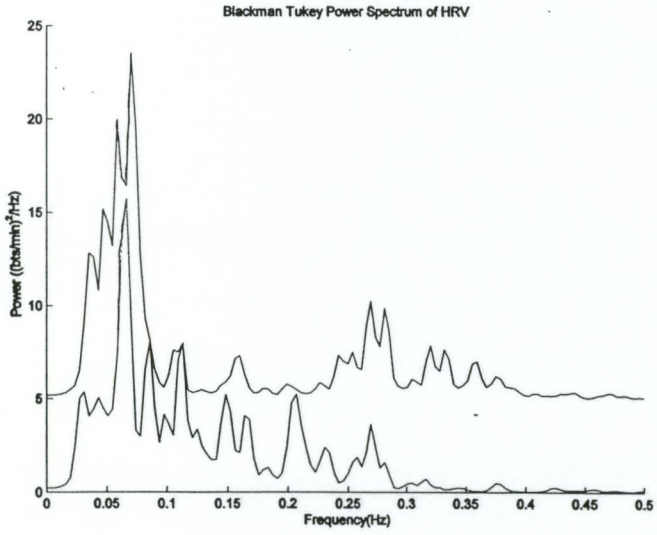

(b)

Figure 6.6 Blackman-Tukey power spectrum of HRV signal during supine and tilt: (a) Supine. (b) 30 degree tilt. (c) 60 degree tilt. (d) 90 degree tilt.

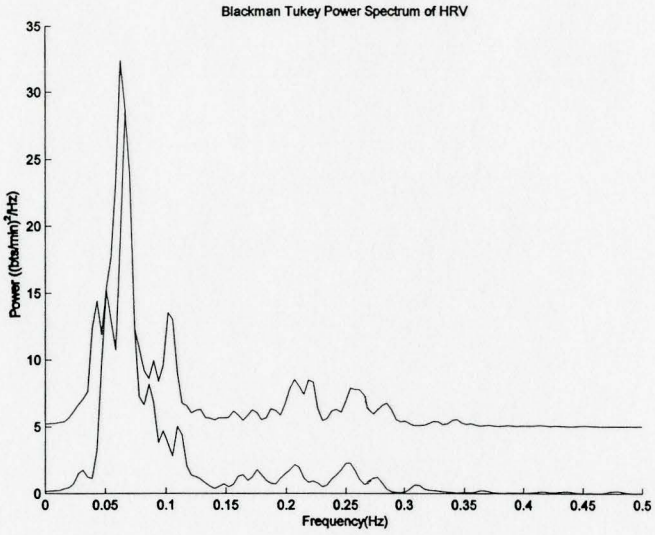

(c)

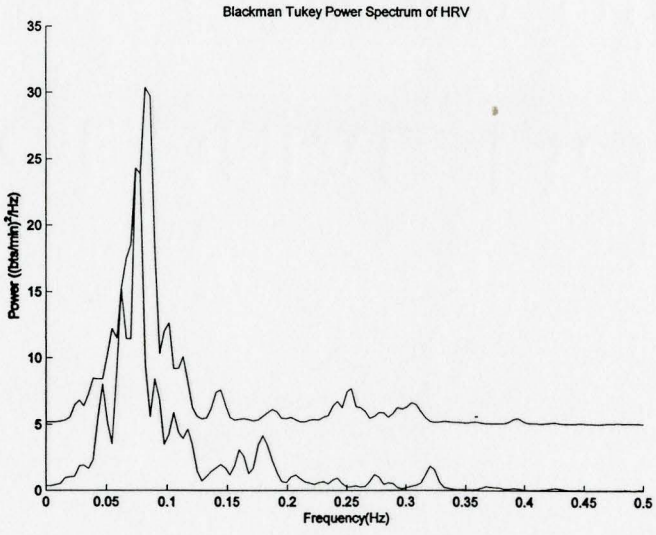

(d)

Figure 6.6 (*contd.*)

6.2.3 Comparison of WVD with AR & BT

In order to compare the WVD technique with AR & BT methods, we averaged the power spectral density of WVD over a five-minute time interval to get indices of LF power, HF power and LF:HF ratio. When we compared LF:HF ratios obtained from WVD technique (Table 6.3) and AR & BT methods (Table 6.1-6.2), the mean LF:HF ratio demonstrates an increasing trend as angle increases, irrespective of the method used. The averaged LF:HF ratio is then plotted separately for three different techniques (Figure 6.7 (a)-(c)), while the combined plot of all three methods is shown in Figure 6.7 (d). The WVD produces a variance which is less than that due to BT method but greater than that due to AR method. However, it seems that the WVD and BT methods both have a higher sensitivity of discriminating the change of LF:HF ratio from supine state to upright position.

6.2.4 Physiological Relevance

During supine state, there is no specific demand on the heart to supply blood against gravity Therefore, the LF/HF ratio is low During 90^{o} tilt, the blood pressure tends to fall due to gravity and is therefore supported by the sympathetic outflow in the form of increased venous return. Hence LF/HF ratio reaches a maximum. LF/HF ratio increases proportionately with increasing values of the tilt angle.

Table 6.1 Mean LF:HF ratio over ~5 min at four different angles using AR PS algorithm

	LF:HF at 0°	**LF:HF at 30°**	**LF:HF at 60°**	**LF:HF at 90°**
Subject1	0.79	1.17	1.94	N/A
Subject2	0.69	1.26	1.74	1.67
Subject3	0.66	0.9	1.23	1.61
Subject4	1.73	0.97	1.42	1.56

Table 6.2 Mean LF:HF ratio over ~5 min at four different angles using BT PS algorithm

	LF:HF at 0°	**LF:HF at 30°**	**LF:HF at 60°**	**LF:HF at 90°**
Subject1	1.18	2.23	7.98	N/A
Subject2	0.64	4.61	5.26	7.77
Subject3	0.61	2.3	3.74	4.82
Subject4	1.08	2.27	4.75	7.35

Table 6.3 Mean LF:HF ratio over ~5 min at four different angles using WVD algorithm

	LF:HF at 0°	**LF:HF at 30°**	**LF:HF at 60°**	**LF:HF at 90°**
Subject1	1.08	2.19	7.04	N/A
Subject2	0.62	4.56	4.94	6.77
Subject3	0.62	1.69	2.9	5.45
Subject4	0.94	2.3	4.28	6.33

Table 6.4 Comparison of the group average and standard deviation for three algorithms

	LF:HF at 0°	**LF:HF at 30°**	**LF:HF at 60°**	**LF:HF at 90°**
AR	0.97	1.08	1.58	1.61
BT	0.88	2.85	5.43	6.65
WVD	0.82	2.69	4.79	6.18
Stdev AR	0.51	0.17	0.32	0.06
Stdev BT	0.29	1.17	1.81	1.6
Stdev WVD	0.23	1.28	1.72	0.67

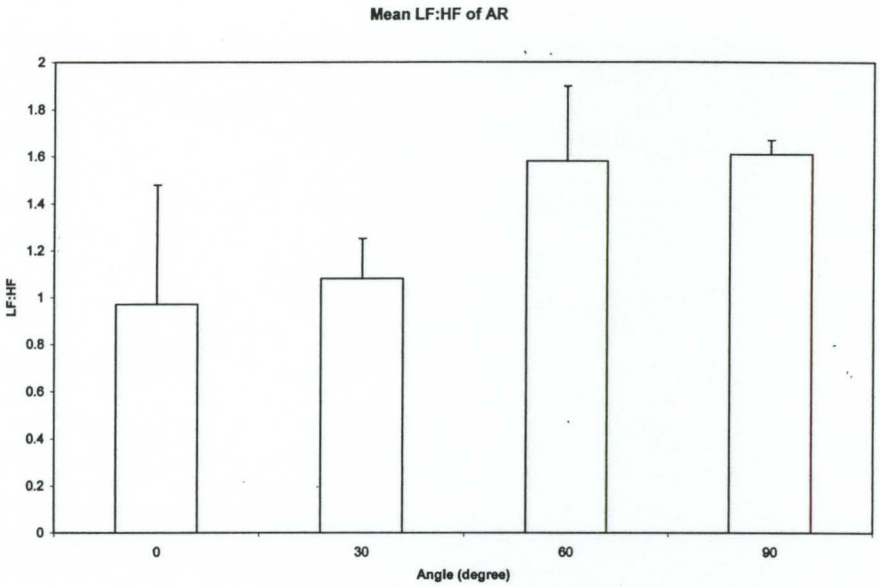

(a)

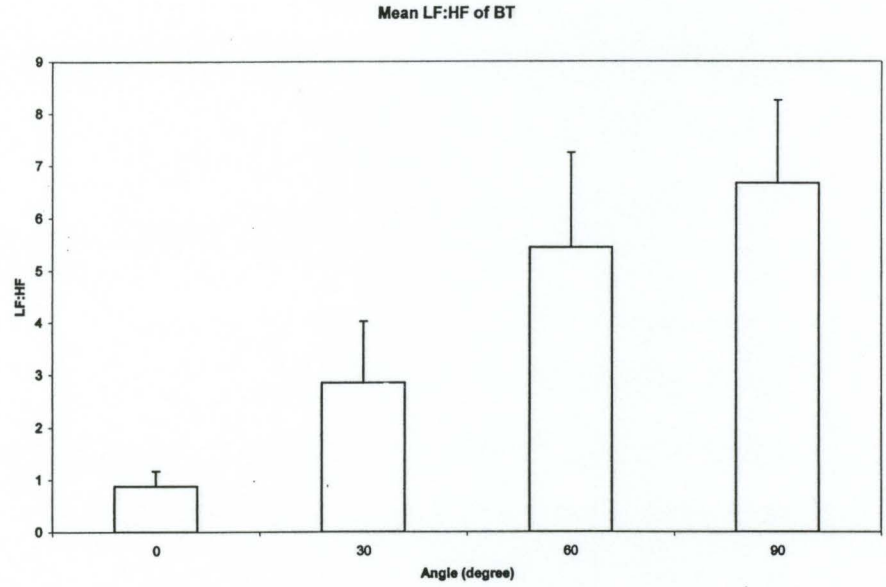

(b)

Figure 6.7 Comparison of mean LF:HF ratio obtained using AR, BT & WVD methods: (a) LF:HF versus angle using AR method. (b) LF:HF versus angle using BT method. (c) LF:HF versus angle using WVD method. (d) Combined plot of LF:HF versus angle using AR, BT & WVD techniques (bar with no pattern: AR; bar with diagonal line: BT; bar with dots: WVD).

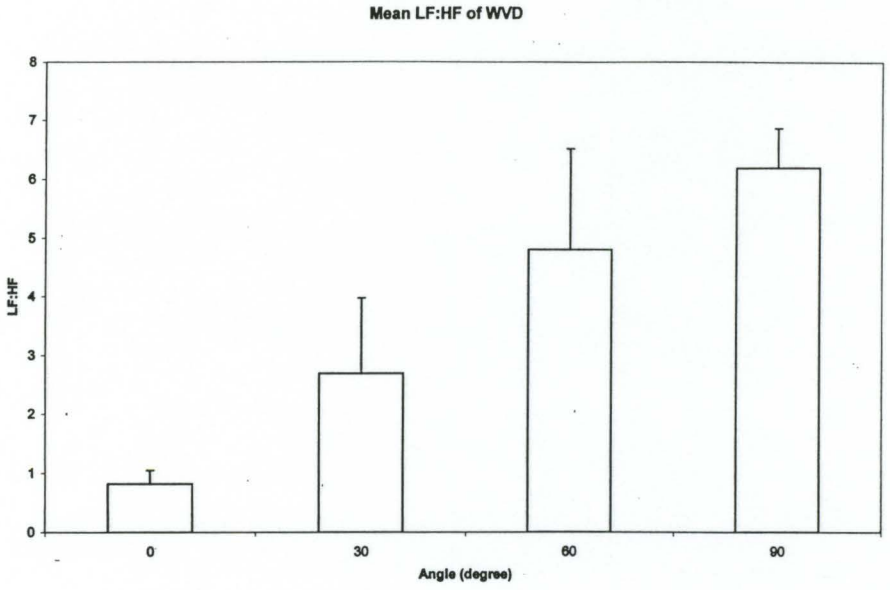

(c)

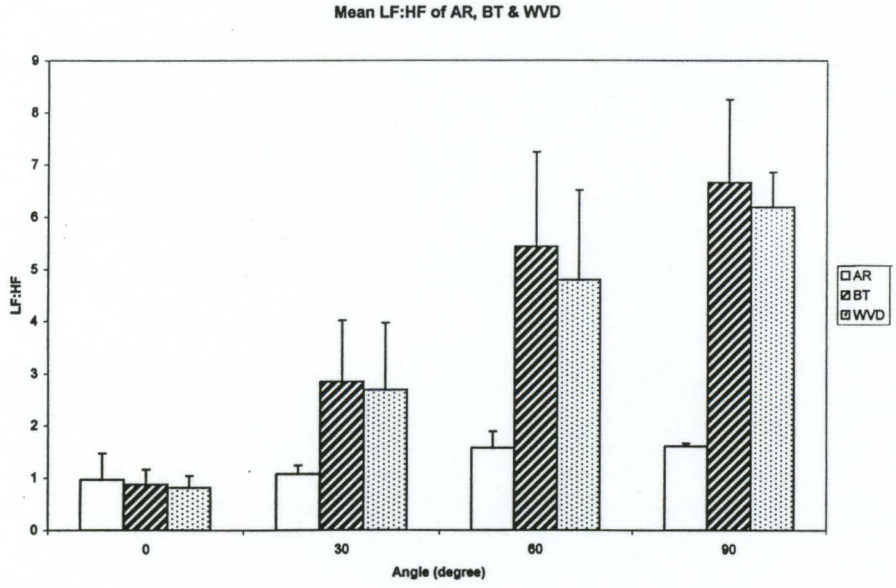

(d)

Figure 6.7 (*contd.*)

6.3 TIME-FREQUENCY ANALYSIS OF HRV DURING SLEEP

The objective of the second study was to examine the usefulness of analyzing PS/HRV using Wigner-Ville distribution and autoregressive model during different stages of sleep. Recent clinical studies suggest that an analysis of HRV during various sleep stages provides additional useful information in patients who had a myocardial infarction (Vanoli, 1994). Determination of a sleep stage is based on the combined information from electroencephalogram (EEG), electro-oculogram (EOG), and electromyogram (EMG) recordings. There are five sleep stages each with distinct EEG, EOG, and EMG activity characteristics (Figure 6.8). These five stages normally appear in a cyclic fashion (stage 1-2-3-4-3-2-REM) with cycle duration varying between 70 to 120 minutes. Sleep stages 3 and 4 last longer than other stages of sleep. Further, stages 3 and 4 are present early in the night and decrease during early morning, while REM sleep shows the opposite trend (Huggins, 1998).

6.3.1 Experiment Design

6.3.1.1 Subjects

Six subjects (two female, four male; mean age 22.7 ± 1.5 years) took part in this study. The sleep studies were conducted in the clinical neuroscience sleep investigation unit at McMaster University Health Science Center in collaboration with J. Huggins, from the department of Kinesiology (Huggins, 1998).

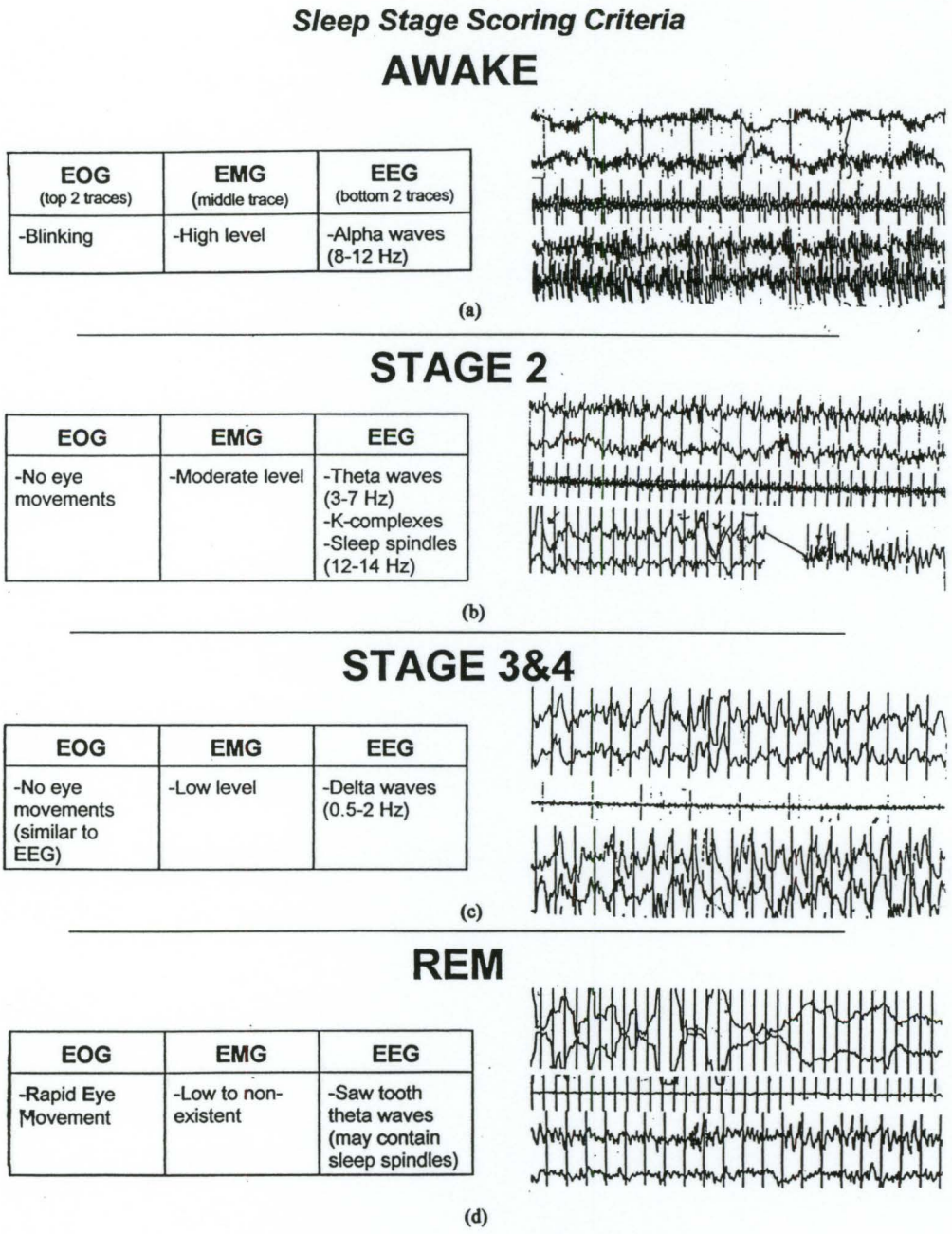

Figure 6.8 Sleep stage scoring criteria using EOG (top two traces), EMG (middle trace), and EEG (lower two traces). (a) Awake stage. (b) Sleep stage 2. (c) Sleep stage 3&4. (d) REM sleep. (From Huggins JD, 1998).

6.3.1.2 Measurements

Specific variables recorded include EEG, EOG, EMG, ECG and respiration. EEG data consisted of two channels each from occipital and central electrodes, positioned according to the international 10-20 electrode placement system for recording EEG (Daly and Pedley, 1990). EOG electrodes were placed above and below the right and left canthi of the eyes respectively, for two traces. Two EMG electrodes were attached beneath the chin. These six traces were amplified through a polysomnograph (Grass, model 8-20D). Two ECG lead and respiration traces were amplified through an ECG and an impedance plethysmograph (Hewlett-Packard). The polysomnograph and the amplifiers were interfaced with a personal computer (Gateway 2000/486) through CODAS resulting in eight channels of data. The sampled data was stored on a hard disk for off-line analysis.

6.3.2 Data Analysis

For each subject, three ten-minute long segments of the data during various sleep stages were subjected to analysis. Data was examined during following states: wakefulness, stage 2 (light sleep), stage 3 and 4 (slow wave sleep), REM. Each state of sleep was visually scored throughout the nightly recording and checked during off-line analysis according to standard criteria.

The ECG signal was processed as described in Chapters 2 and 3. We identified QRS complexes, constructed a time series of R-R intervals and computed the autoregressive power spectra. The 2-D autoregressive power spectra of HRV are shown in Figure 6.9 for a sample subject. The Wigner-Ville distribution of the R-R interval was computed using **Wigner95**, the software package developed for this thesis and described

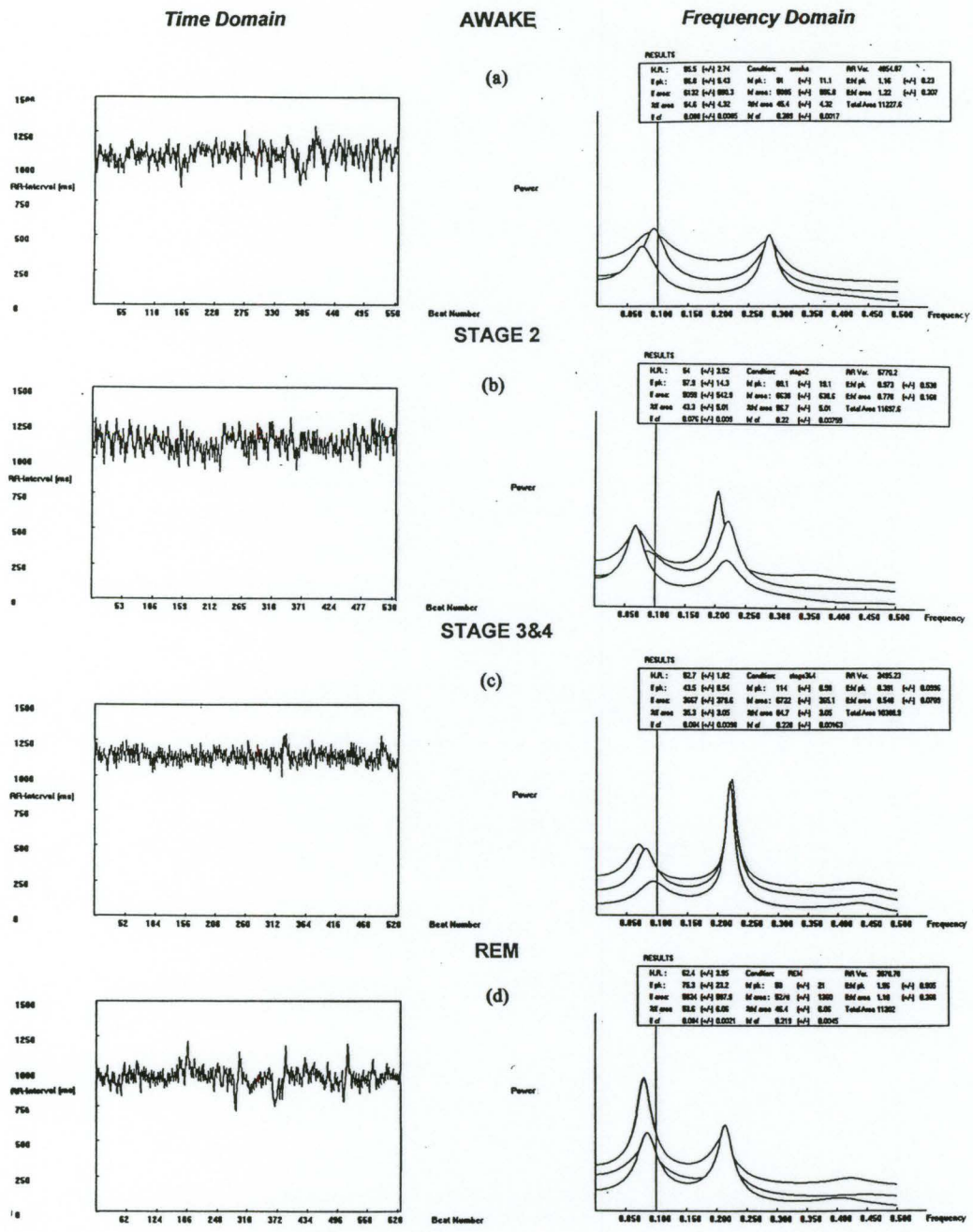

Figure 6.9 R-R interval and AR power spectra of different sleep stages: (a) Awake stage. (b) Sleep stage 2. (c) Sleep stage 3&4. (d) REM sleep. (From Huggins JD, 1998).

in Chapter 3. The results of Wigner-Ville distribution are shown in Figure 6.10-6.11 for stage 3&4 and REM sleep respectively. The ratio of low frequency power (LF: 0.04-0.15 Hz) to high frequency power (HF: 0.15-0.5 Hz) can be monitored during all sleep stages using AR method (Figure 6.9). Furthermore, as shown in Figure 6.11 the Wigner-Ville distribution provides more descriptive information in time-frequency plane. There is a consistent increase in the HF power of the power spectra using both AR method and Wigner-Ville distribution during sleep stage 3&4 (Figure 6.9 (c) and Figure 6.10 (b)). On the other hand, there is no dominant HF peak in time-frequency plane during REM sleep (Figure 6.11 (b)).

From a physiological point of view, this can perhaps be explained as follows. There is a functional resemblance between sleep and its apparent antithesis, exercise (Verrier, 1996). Both activities involve motor programs of the central nervous system, and appropriate central autonomic patterns are activated. The surges in sympathetic activity and reduction in baroreceptor sensitivity associated with REM sleep and severe exertion during wakefulness may precipitate myocardial ischemia, and trigger ventricular tachyarrhythmias. Therefore it is possible to explain the lack of dominant HF peak in REM sleep.

Further studies are needed to understand physiological mechanisms during different stages of sleep and may provide insights in the heart function of patients following a myocardial infarction.

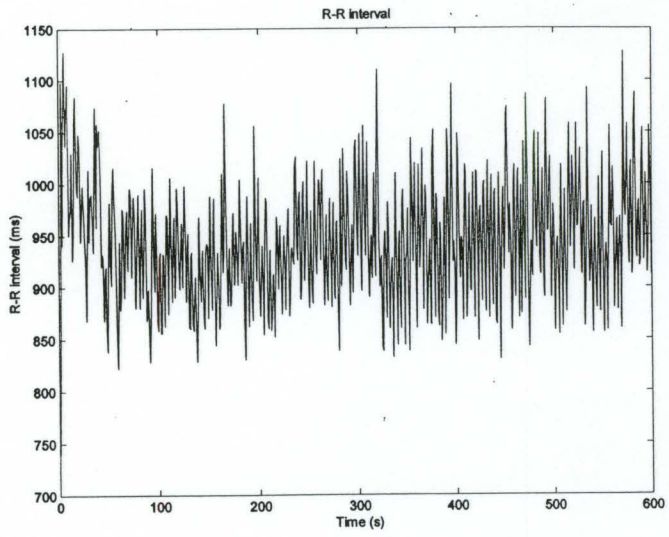

(a)

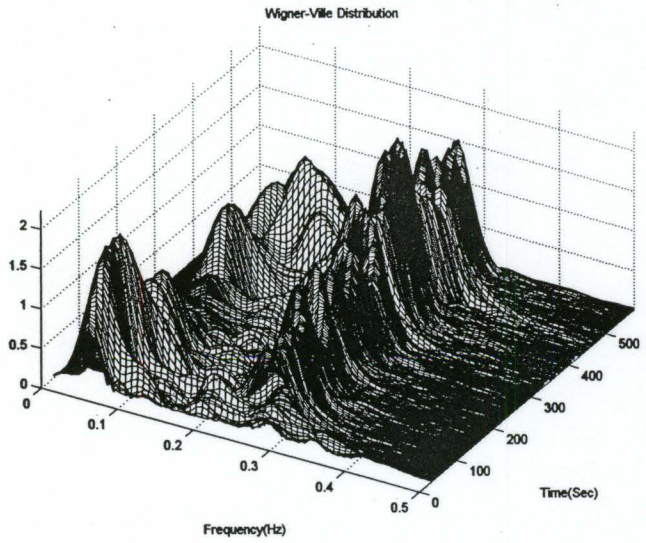

(b)

Figure 6.10 Results of Wigner-Ville distribution for sleep stage 3&4: (a) R-R interval. (b) 3-D plot of WVD. (c) 2-D contour plot of WVD. (d) R-R, LF power, HF power, and LF:HF ratio versus time.

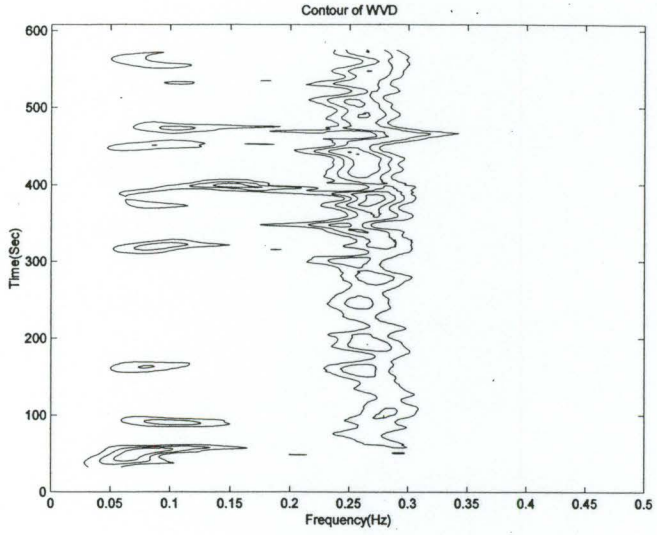

(c)

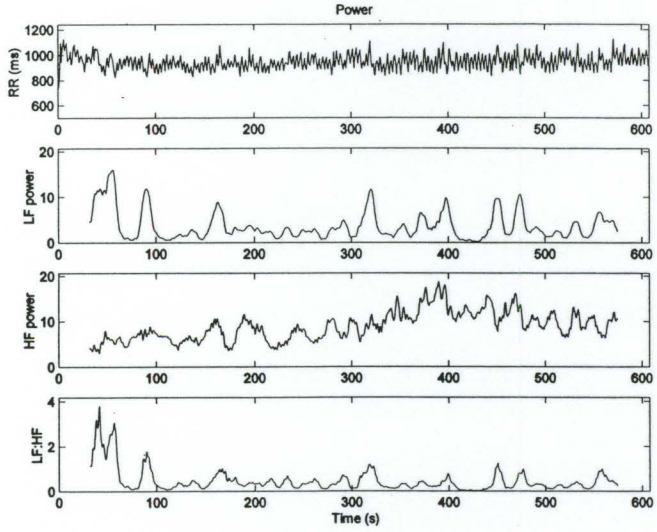

(d)

Figure 6.10 (*contd.*)

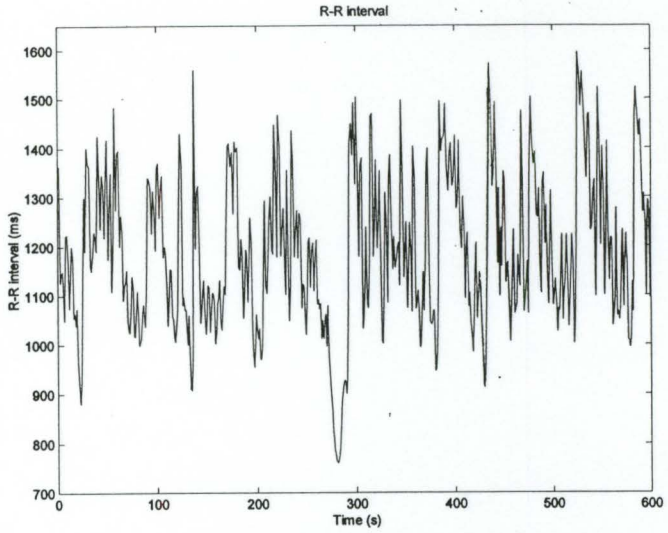

(a)

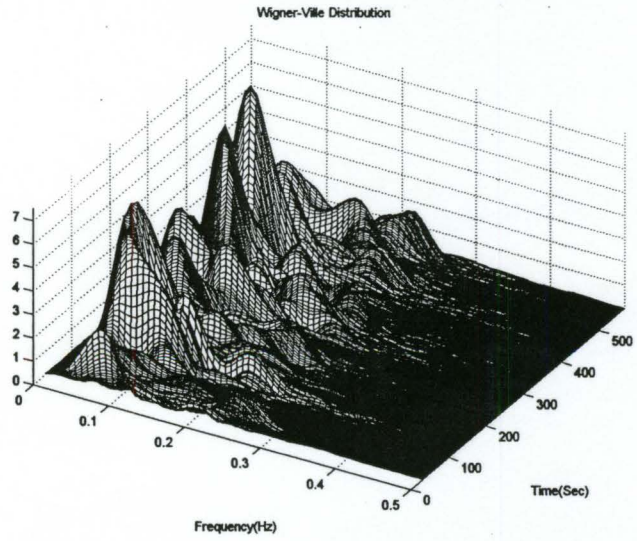

(b)

Figure 6.11 Results of Wigner-Ville distribution for REM sleep: (a) R-R interval. (b) 3-D plot of WVD. (c) 2-D contour plot of WVD. (d) R-R, LF power, HF power, and LF:HF ratio versus time.

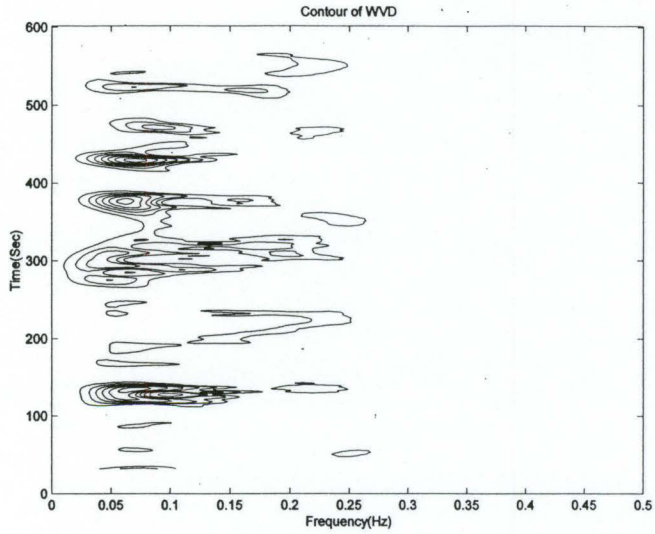

(c)

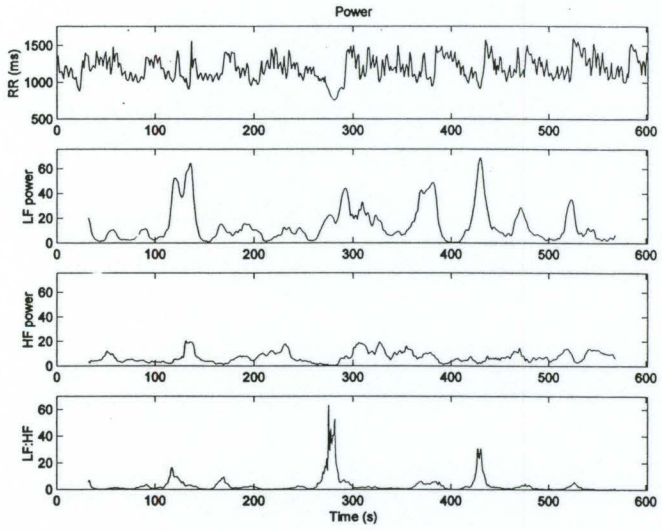

(d)

Figure 6.11 (*contd.*)

Chapter 7

Summary

7.1 SUMMARY

The work described in this thesis discusses the theoretical issues, algorithms and results of our studies involving digital signal processing of hemodynamic signals. In Chapter 1, we review the current literature on power spectral analysis of heart rate variability (HRV) and its use in studying autonomic nervous system (ANS). We also present the objectives of our work.

Off-line implementations of QRS detection, construction of HRV signal and computation of the power spectrum (PS) of HRV are described in Chapter 2. Specifically, autoregressive (AR) modelling method and Blackman-Tukey (BT) algorithm are discussed. Our results show that the QRS detection algorithm developed for this study was successful in detecting QRS complexes of the ECG signals recorded from healthy controls and patients in our laboratory with an error rate of less than ~0.2%. It was also shown that AR modelling method and BT algorithm revealed two distinctive frequency

bands (LF & HF) and thus provide a useful index (LF:HF ratio) for measuring sympathovagal balance.

While the concept of power spectral analysis has been employed in the study of ANS for more than a decade (Pomeranz et al., 1985), the analysis of HRV using time-frequency distribution (TFD) techniques has been investigated only for the last five years (Novak et al., 1993). Theoretical details and a C++ software package for computing time-frequency distribution of HRV, in particular, Wigner-Ville distribution (WVD) technique, are presented in Chapter 3. We found that an average of Wigner-Ville distribution computed from 128-second HRV signal yielded results comparable to those obtained from AR modelling method and BT algorithm. In addition, WVD technique provided more relevant information and detail in the time-frequency plane because of a large number of power spectra.

Success of our algorithms and software can only be measured by their application in evaluating human and animal autonomic nervous system. Towards this end, we describe in Chapter 4, the application of power spectral analysis for studying the ontogeny of ANS in premature infants. Our results suggest that a sympathetic predominance in early post-natal life (with a peak in sympathetic outflow at 30-32 weeks) is followed by an increase in the vagal outflow and an increase in the ANS responsiveness for increasing post-natal age. In Chapter 5, the applications of power spectra of HRV in studying the ANS of a rat model are presented. The study shows that power spectral analysis of HRV is sensitive enough to detect dose-dependent changes in nervous activity following atropine and methacholine challenge and provide additional evidence supporting the role of the autonomic nervous system in asthma.

In an attempt to test the usefulness of time-frequency distribution, a tilt paradigm is described in Chapter 6 to delineate a quantitative comparison of AR, BT and WVD techniques. The results show that WVD technique produces a continuous index (LF:HF ratio) of sympathovagal balance and with greater detail than that generated by AR and BT methods. Finally, an application of WVD technique to study the changes that take place in the ANS function during different stages of sleep is presented.

Bibliography

Akaike H (1974), "A new look at the statistical model identification," *IEEE Trans Autom Control*, vol. AC19, pp. 716-723.

Akselrod S, Gordon D, Ubel FA, Shannon DC, Barger AC, Cohen RJ (1981), "Power spectrum analysis of heart rate fluctuations: a quantitative probe of beat-to-beat cardiovascular control," *Science*, 213:220-222.

Alpert B (1995), "Neonatal blood pressure," in Clinical Information & Technology Series: Neonatal Intensive Care, pp. 29-30. SpaceLabs Medical, Inc., Washington, USA.

Assali NS, Brinkman CR III, Woods JR, Dandavino A (1978), "Ontogeny of the autonomic control of cardiovascular functions in the sleep," in Longo L, Ed., Fetal and Newborn Cardiovascular Physiology, pp. 49-91. Garland Press, NY, USA.

Barnes PJ (1995), "Is asthma a nervous disease?," *Chest,* 107: 119S-125S.

Bendat JS, Peirsol AG (1986), "Random Data: Analysis and Measurement Procedures," 2nd Ed., Wiley, New York.

Birnbaum SG, Richardson BC, Dellinger JA (1988), "Quantifying the altered cardiac response to atropine following pyridostigmine in rhesus macaques," *Pharmacol Biochem Behav,* 31: 381-386.

Boashash B, Black PJ (1987), "An efficient real-time implementation of the Wigner-Ville distribution," *IEEE Trans ASSP*, vol. 35, no. 11, pp. 1611-1618.

Boashash B (1991), "Time-frequency signal analysis," in Haykin S., Ed., Advances in Spectrum Analysis and Array Processing, volume 1, Chapter 9, pp. 418-517. Prentice-Hall: Englewood Cliffs, NJ.

Boashash B (1992), Time-Frequency Signal Analysis, pp.165, Longman Cheshire, Halsted Press, UK.

Brown TE, Beightol LA, Koh J, Eckberg DL (1993), "Important influence of respiration on human R-R interval power spectra is largely ignored," *J Appl Physiol*, 75:2310-2317.

Cabanas F, Pellicer A, Garcia-Alix A, Quero J, Stiris TA (1997), "Effect of dexamethasone therapy on cerebral and ocular blood flow velocity in premature infants studied by colour Doppler flow imaging," *Eur J Pediatr*, 156(1):41-46.

Cerutti C, Gustin MP, Paultre CZ, Lo M, Julien C, Vincent M, Sassard J (1991), "Autonomic nervous system and cardiovascular variability in rats: a spectral analysis approach," *Am J Physiol,* 261: H1292-H1299.

Chatow U, Davidson S, Reichman B, Akselrod S (1995), "Development and maturation of the autonomic nervous system in premature and full-term infants using spectral analysis of heart rate fluctuations," *Pediatr Res*, 37(3):294-302.

Clairambault F, Curzi-Dascalova L, Kauffmann F, Medigue D, and Leffler CH (1992), "Heart-rate variability in normal sleeping full-term and preterm neonates," *Early Hum Dev*, 28:169-183.

Cohen L (1966), "Generalized phase-space distribution functions," *J Math Phys*, vol. 7, pp. 781-786.

Cohen L (1989), "Time-frequency distributions – Review," *Proc IEEE*, 77, 941-981.

Cohen L(1992), "Time-frequency signal analysis," in Boashash B., Ed., Time-Frequency Signal Analysis, Chapter 1, pp. 3-42. Longman Cheshire, Halsted Press, UK.

Daly DD, Pedley TA, Ed. (1990), Current Practice of Clinical Electroencephalography, pp. 31-32. Raven Press, NY, USA.

DeBruijin NG (1967), "Uncertainty principles in Fourier analysis", in Shisha O, Ed., Inequalities, pp. 57-71, Academic Press, New York.

Djuric VJ, Overstreet DH, Bienenstock J, Perdue MH (1995), "Immediate hypersensitivity in the Flinders rat: Further evidence for a possible link between susceptibility to allergies and depression," *Brain Behav Immunity,* 9: 196-206.

Djuric VJ, Roberts S, Overstreet DH, Chen Y, Wang L, Tougas G (1997), "Autonomic modulation of intestinal anaphylaxis in a rat model of cholinergic sensitivity," *Gastroenterology,* 112: A722

Djuric VJ, Cox G, Overstreet DH, Smith L, Dragomir A, Steiner M (1998), "Genetically transmitted cholinergic hyperresponsiveness predisposes to experimental asthma," *Brain Behav Immunity* (In press).

Dougherty CM, Burr RL (1992), "Comparison of heart rate variability in survivors and nonsurvivors of sudden cardiac arrest," *Am J Cardiol*, 70:441.

Durbin J (1960), "The fitting of time-series models," *Rev Inst Int Statist*, 28: 233-243.

Eiselt M, Curzi-Dascalova L, Clairambault J, Kauffmann F, Medigue C, and Peirano P (1993), "Heart-rate variability in low-risk prematurely born infants reaching normal term: a comparison with full-term newborns," *Early Hum Dev*, 32:183-195.

Friesen GM, Jannett TC, Jadallah MA, Yates SL, Quint SR, Nagle HT (1990), "A comparison of the noise sensitivity of nine QRS detection algorithms," *IEEE Trans Biomed Eng*, 37(1): 85-98.

Garudadri H, Beddoes MP, Benguerel A-P, Gilbert JHV (1987), "On computing the smoothed Wigner distribution", *Proc ICASSP*-87, pp. 1521-1524.

Georgief MK, Mills MM, Gomez-Marin O, and Sinaiko AR (1996), "Rate of change of blood pressure in premature and full term infants from birth to 4 months," *Ped Nephrology*, 10:152-155.

Greenough A, Emerey EF (1993), "Blood pressure levels of preterm infants in the first year of life," *Acta Paediatr*, 82:528-529.

Hamelman E, Schwarze J, Takeda K, Oshiba A, Larsen GL, Irwin CG, Gelfand EW (1997), "Noninvasive measurement of airway responsiveness in allergic mice using barometric plethysmography," *Am J Respir Crit Care Med,* 156: 766-775.

Hamilton P, Tompkins W (1986), "Quantitative investigation of QRS detection rules using the MIT/BIH arrhythmia database," *IEEE Trans Biomed Eng*, 33(12): 1157-1165.

Harper RM, Schechtman VL, and Kluge KA (1987), "Machine classification of infant sleep state using cardiorespiratory measures," *Electroencephalogr Clin Neurophysiol*, 67:379-387.

Harvey A (1997), "Effect of age on autonomic neurocardiac function in healthy males and females," Master Thesis, Dept. of Kinesiology, McMaster University.

Hirsch JA, Bishop B (1981), "Respiratory sinus arrhythmia in humans: how breathing pattern modulates heart rate," *Am J Physiol*, 241:H620-H629.

Hlawatsch F, Boudreaux-Bartels GF (1992), "Linear and quadratic time-frequency signal representations," *IEEE Trans Sign Proc Mag*, pp. 21-67.

Hockman CH (1987), Essentials of Autonomic Function, pp. 42. Springfield IL, USA.

Hon E, Lee S (1965), "The fetal electrocardiogram – III. Display techniques," *Am J Obst & Gynec*, 91: 56-60.

Hsu WH (1985), "Effects of atropine and xylazine-pentobarbital anaesthesia in dogs: preliminary study," *Am J Vet Res,* 46: 856-858.

Huggins JD (1998), "Variations in cardiac autonomic balance during sleep stages displayed by power spectral analysis of heart rate variability," Undergraduate Thesis, Dept. of Kinesiology, McMaster University.

Japundzic N, Grichois ML, Zitoun P, Laude D, Elghozi JL (1990), "Spectral analysis of blood pressure and heart rate in conscious rats: effects of autonomic blockers," *J Autonom Nerv Syst,* 30: 91-100.

Jasson S, Medigue C, Maison-Blanche P, Montano N, Meyer L, Vermeiren C, Mansier P, Coumel P, Malliani A, Swyngnedauw B (1997), "Instant power spectrum analysis of heart rate variability during orthostatic tilt using a time-/frequency-domain method," *Circulation,* 96(10): 3521-3526.

Jenkins GM, Watts DG (1968), Spectral Analysis and Its Applications, Chapter 6, pp. 209-257. Holden-Day, San Francisco, USA.

Kamath MV, Fallen EL, McKelvie R (1991), "Effects of steady state exercise on the power spectrum of heart rate variability," *Med Sci Sports Excer,* 23:428.

Kamath MV, Fallen EL (1993), "Power spectral analysis of heart rate variability: a noninvasive signature of cardiac autonomic function," *Crit Rev Biomed Eng*, 21(3): 245-311.

Kamath MV, Fallen EL (1995), "Correction for ectopics and missing beats in the heart rate variability signal," in Malik M, Camm AJ, Ed., Heart Rate Variability, pp. 75-85, Futura Publishing Company, Inc., Armonk, NY, USA.

Katona PG, Jih F (1975), "Respiratory sinus arrhythmia: noninvasive measure of parasympathetic cardiac control," *J Appl Physiol*, 39:801-805.

Kay SM, Marple SL (1981), "Spectrum analysis – a modern perspective," *Proc IEEE* 69, 1380.

Kay SM (1988), Modern Spectral Estimation – Theory & Application, Chapter 6, pp. 153-216. Prentice-Hall: Englewood Cliffs, NJ, USA.

Kuwahara M, Yayou K, Ishii K, Hashimoto S, Tsubone H, Sugano S (1994), "Power spectral analysis of heart rate variability as a new method for assessing autonomous activity in the rat," *J Electrocardiol,* 27: 333-337.

Leff AR (1997), "Future directions in asthma therapy. Is a cure possible?," *Chest,* 111: 61S-68S.

Levinson N (1947), "The Wiener RMS (root mean square) error criterion in filter design and prediciton," *J Math Phys*, 25: 261-278.

Levy MN, DeGeest H, Zieske H (1966), "Effects of respiratory center activity on the heart," *Circulation Res*, 18:67-78.

Lin Z, Chen J, (1996), "Advances in time-frequency analysis of biomedical signals," *Crit Rev Biomed Eng*, 24(1): 1-72.

Lishner M, Akselrod S, Mor Avi V, Oz O, Divon M, aand Ravid M (1987), "Spectral analysis of heart rate fluctuations. A non-invasive, sensitive method for the early diagnosis of autonomic neuropathy in diabetes mellitus," *J Auton Nerv Syst*, 19:119.

Lombardi F, Sandrone G, Pernpruner L, Sala R, Garimoldi M, Cerutti S, Baselli G, Pagani M, and Malliani A (1987), "Heart rate variability as an index of sympathovagal interaction after acute myocardial infarction," *Am J Cardiol*, 60: 1239.

Low PA, (1997), Ed., 2nd edition, Clinical Autonomic Disorders: Evaluation and Management, Chapter 6 and 26. Lippincott-Raven publishers, Philadelphia and New York, USA.

Ludwig C (1847), "Beitrage zur Kenntniss des Einflusses der Respirations bewegungen auf den Blutlauf im Aortensysteme," *Arch Anat Physiol*, 13: 242-302.

Malliani A, Pagani M, Lombardi F, and Cerutti S (1991), "Cardiovascular neural regulation explored in the frequency domain," *Circulation*, 84(2): 482-492.

Malliani A, Pagani M, and Lombardi F (1994), "Physiology and clinical implications of variability of cardiovascular parameters with focus on heart rate and blood pressure (Review)," *Am J Physiol*, 73 (10): 3C-9C.

Martin TR, Ando A, Takeishi T, Katona IM, Drazen JM, Galli SJ (1993), "Mast cells contribute to the changes in heart rate, but not hypotension or death, associated with active anaphylaxis in mice," *J Immunol,* 151: 367-376.

Myers GA, Martin GJ, Magid NM, Barnett PS, Schaad JW, Weiss JS, Lesch M, and Singer DH (1986), " Power spectral analysis of heart rate variability in sudden cardiac death," *IEEE Trans Biomed Eng*, 33:1149.

Novak V, Novak P, De Champlain J, Le Blanc AR, Martin R., Nadeau R. (1993), "Influence of respiration on heart rate and blood pressure fluctuations", *J Appl Physiol*, 74: 617-626.

Novak V, Novak P, Low PA (1997), "Time-frequency analysis of cardiovascular function and its clinical applications," in Low PA, Ed., 2nd edition, Clinical Autonomic Disorders: Evaluation and Management, Chapter 26, pp. 345-347, Lippincott-Raven publishers, Philadelphia and New York, USA.

Oppenheim AV, Schafer RW (1975), Digital Signal Processing, pp. 211-218. Prentice-Hall: Englewood Cliffs, NJ, USA.

Osmond MH, Klassen TP (1995), "Efficacy of ipratropium bromide in acute childhood asthma: a meta-analysis," *Acad Emerg Med,* 2: 651-656.

Pagani M, Lombardi F, Guzzetti F, Rimoldi O, Furlan R, Pizzinelli P, Sandrone G, Malfatto G, Dell'orto S, Piccaluga E, Turiel M, Baselli G, Cerutti S, Malliani A (1986), "Power spectral analysis of heart rate and arterial pressure variabilities as a marker of sympathovagal interaction in man and conscious dog," *Circ Res*, 59(2):178-193.

Pagani M, Malfatto G, Peirini S et al. (1988), "Spectral analysis of heart rate variability in the assessment of autonomic diabetic neuropathy," *J ANS*, 23:143-153.

Pahlm O, Sornmo L (1984), "Software QRS detection in ambulatory monitoring – A review," *Med Biol Eng Comput*, 22: 289-297.

Pan J, Tompkins W (1985), "A real time QRS detection algorithm," *IEEE Trans Biomed Eng*, 32(3): 230-236.

Persson CGA (1997), "Centennial notions of asthma as an eosionophilic, desquamative, exudative, and steroid-sensitive disease," *Lancet,* 350: 1021-1024.

Pola S, Macerate A, Emdin M, Marchesi C (1996), "Estimation of the power spectral density in nonstationary cardiovascular time series: assessing the role of the time-frequency representations (TFR)," *IEEE Trans Biomed Eng,* 43(1): 46-59.

Pomeranz B, Macaulay RJB, Caudill MA, Kuntz I, Adam D, Gordon D, Kilborn KM, Barger AC, Shannon DC, Cohen RJ, Benson H (1985), "Assessment of autonomic function in humans by heart rate spectral analysis," *Am J Physiol*, 248:H151-H153.

Prechtl HFR (1974), "The behavioral states of the newborn infant (Review)," *Brain Res*, 76:185-212.

Reilly JP (1998), EE 731 Course Notes, "Matrix Computation and Signal Processing", Dept. of Electrical and Computer Engineering, McMater University.

Rubini R, Porta A, Baselli G, Cerutti S, Paro M (1993), "Power spectral analysis of cardiovascular variability monitored by telemetry in conscious unrestrained rats," *J Autonom Nerv Sys,* 45: 181-190.

Ruha A, Sallinen S, Nissila S (1997), "A real-time microprocessor QRS detector system with 1-ms timing accuracy for measurement of ambulatory HRV," *IEEE Trans Biomed Eng,* 44: 159-167.

Sabatino G, Quartulli L, DiFabio S, Ramenghi LA (1997), "Hemodynamic effects of intravenous morphine infusion in ventilated preterm babies," *Early Hum Dev*, 47(3):263-270.

Saul JP, Arai Y, Berger RD, Lilly LS, Colucci WS, and Cohen RJ (1988), "Assessment of autonomic regulation in chronic congestive heart failure by heart rate spectral analysis," *Am J Cardiol*, 61:1292.

Sayers BM (1973), "Analysis of heart rate variability," *Ergonomics*, 16:17-32.

Schwarz M (1970), "Information transmission, modulation, and noise," Chapter 8, pp. 577-584. New York: McGraw-Hill, USA.

Sgoifo A, Stilli D, Aimi B, Parmigiani S, Manghi M, Musso E (1994), "Behavioral and electrocardiographic responses to social stress in male rats," *Physiol Behav,* 55: 209-216.

Shannon DC, Carley DW, and Benson H (1987), "Aging of modulation of heart rate," *Am J Physiol*, 253(22):H874-H877.

Spaziani R, Djuric V, Kamath MV, Sridhar S, Armstrong D, Fallen EL, Upton ARM, Tougas G (1996), "Autonomic response to esophageal acid perfusion in patients with esophageal symptoms," Annual Meeting of American Gastroenterological Association and American Association for the study of Liver Diseases, San Francisco, USA. *Gastroenterology*, 110:A762.

Stankovic L (1994), "Time-frequency signal analysis," Research Monograph, pp. 1-18, Epsilon and Montenegropublic publishers, Montenegro.

Task force of the European Society of Cardiology and the North American Society of Pacing and Electrophysiology (1996), "Heart rate variability – standards of measurement, physiological interpretation and clinical use," *Circulation,* 93:1043-1065.

Van Ravenswaaij-Arts CMA, Hopman JCW, Kollee LAA, Van Amen JPL, Stoelinga GBA, and Van Geijn HP (1991), "Influences on heart rate variability in spontaneously breathing preterm infants," *Early Hum Dev*, 27:187-205.

Van Ravenswaaij-Arts C, Hopman J, Kollee L, Stoelinga G, and Van Geijn H (1994), "Spectral analysis of heart rate variability in spontaneously breathing very preterm infants," *Acta Paediatr*, 83:473-480.

Vanoli E, Adamson PB, Ba-Lin MPH, Pinna GD, Lazzara R, Orr WC (1994), "Heart rate variability during specific sleep stages: a comparison of healthy subjects with patients after myocardial infarction," *Circulation*, 91:1918-1992.

Verrier RL, Muller JE, Hobson JA (1996), "Sleep, dreams, and sudden death: the case for sleep as an autonomic stress test for the heart," *Cardiovascular Res*, 31:181-211.

Vybiral T, Bryg RJ, Maddens Me, Bhasin ME, Cronin S, Boden WE, Lehman MH (1990), "Effects of transdermal scopolamine on heart rate variability in normal subjects," *Am J Cardiol,* 65:604.

Webster JG (1978), "Medical Instrumentation – Application and Design," Boston: Houghton Mifflin, USA.

Wietse K, de Jong-de Vos van Stenwijk CCE, Sinnema G, Kavelaars A, Prakken B, Helders PJM, Heijnen CJ (1996), "The autonomic nervous system and the immune system in juvenile rheumatoid arthritis," *Brain Behav Immunity,* 10: 387-398.

Wieling W, Lieshout JJV (1997), "Maintenance of Postural Normotension in Humans," in Low PA, Ed., 2nd edition, Clinical Autonomic Disorders: Evaluation and Management, Chapter 6, pp. 73-82, Lippincott-Raven publishers, Philadelphia and New York, USA.

Xue Q, Hu YH, Tompkins WJ (1992), "Neural-network-based adaptive matched filtering for QRS detection," *IEEE Trans Biomed Eng*, 39: 317-329.

Ziegler D, Laux G, Dannehl K et al. (1992), "Assessment of cardiovascular autonomic function: age-related normal ranges and reproducibility of spectral analysis, vector analysis and standard tests of heart rate variation and blood pressure responses," *Diabetic Medicine*, 9:166-175.

Zubrow A, Hulman S, Kushner H, Falkner B (1995), "Determinants of blood pressure in infants admitted to neonatal intensive care units: a prospective multicenter study," *J Perinat*, 15(6):470-479.